UPPSALA
UNIVERSITET

Digital Comprehensive Summaries of Uppsala Dissertations from the Faculty of Science and Technology 1385

Effect of Substrate on Bottom-Up Fabrication and Electronic Properties of Graphene Nanoribbons

KONSTANTIN SIMONOV

ACTA
UNIVERSITATIS
UPSALIENSIS
UPPSALA
2016

ISSN 1651-6214
ISBN 978-91-554-9610-4
urn:nbn:se:uu:diva-295884

Dissertation presented at Uppsala University to be publicly examined in Häggsalen, Ångströmlaboratoriet, Lägerhyddsvägen 1, Uppsala, Friday, 23 September 2016 at 10:15 for the degree of Doctor of Philosophy. The examination will be conducted in English. Faculty examiner: Professor Alessandro Baraldi (Physics Department, University of Trieste, Italy).

Abstract

Simonov, K. 2016. Effect of Substrate on Bottom-Up Fabrication and Electronic Properties of Graphene Nanoribbons. *Digital Comprehensive Summaries of Uppsala Dissertations from the Faculty of Science and Technology* 1385. 101 pp. Uppsala: Acta Universitatis Upsaliensis. ISBN 978-91-554-9610-4.

Taking into account the technological demand for the controlled preparation of atomically precise graphene nanoribbons (GNRs) with well-defined properties, the present thesis is focused on the investigation of the role of the underlying metal substrate in the process of building GNRs using bottom-up strategy and on the changes in the electronic structure of GNRs induced by the GNR-metal interaction. The combination of surface sensitive synchrotron-radiation-based spectroscopic techniques and scanning tunneling microscopy with *in situ* sample preparation allowed to trace evolution of the structural and electronic properties of the investigated systems.

Significant impact of the substrate activity on the growth dynamics of armchair GNRs of width N = 7 (7-AGNRs) prepared on inert Au(111) and active Cu(111) was demonstrated. It was shown that unlike inert Au(111) substrate, the mechanism of GNRs formation on Ag(111) and Cu(111) includes the formation of organometallic intermediates based on the carbon-metal-carbon bonds. Experiments performed on Cu(111) and Cu(110), showed that a change of the balance between molecular diffusion and intermolecular interaction significantly affects the on-surface reaction mechanism making it impossible to grow GNRs on Cu(110).

It was demonstrated that deposition of metals on spatially aligned GNRs prepared on stepped Au(788) substrate allows to investigate GNR-metal interaction using angle-resolved photoelectron spectroscopy. In particular intercalation of one monolayer of copper beneath 7-AGNRs leads to significant electron injection into the nanoribbons, indicating that charge doping by metal contacts must be taken into account when designing GNR/electrode systems. Alloying of intercalated copper with gold substrate upon post-annealing at 200°C leads to a recovery of the initial position of GNR-related bands with respect to the Fermi level, thus proving tunability of the induced n-doping. Contrary, changes in the electronic structure of 7-AGNRs induced by the deposition of Li are not reversible. It is demonstrated that *via* lithium doping 7-AGNRs can be transformed from a semiconductor into a metal state due to the partial filling of the conduction band. The band gap of Li-doped GNRs is reduced and the effective mass of the conduction band carriers is increased.

Keywords: graphene nanoribbons, bottom-up, substrate, metal contact, electronic structure, electron doping, PES, ARPES, NEXAFS, STM

Konstantin Simonov, Department of Physics and Astronomy, Molecular and condensed matter physics, Box 516, Uppsala University, SE-751 20 Uppsala, Sweden.

ISSN 1651-6214
ISBN 978-91-554-9610-4
urn:nbn:se:uu:diva-295884 (http://urn.kb.se/resolve?urn=urn:nbn:se:uu:diva-295884)

List of papers

This thesis is based on the following papers, which are referred to in the text by their Roman numerals.

I **Effect of Substrate Chemistry on the Bottom-Up Fabrication of Graphene Nanoribbons: Combined Core-Level Spectroscopy and STM Study**
K. A. Simonov, N. A. Vinogradov, A. S. Vinogradov, A. V. Generalov, E. M. Zagrebina, N. Mårtensson, A. A. Cafolla, T. Carpy, J. P. Cunniffe, and A. B. Preobrajenski
J. Phys. Chem. C **118**, 12532-12540 (2014)

Addition/Correction published in *J. Phys. Chem. C* **119**, 880-881 (2015)

II **Comment on "Bottom-Up Graphene-Nanoribbon Fabrication Reveals Chiral Edges and Enantioselectivity"**
K. A. Simonov, N. A. Vinogradov, A. S. Vinogradov, A. V. Generalov, E. M. Zagrebina, N. Mårtensson, A. A. Cafolla, T. Carpy, J. P. Cunniffe, A. B. Preobrajenski
ACS Nano **9**, 3399-3403 (2015)

III **From Graphene Nanoribbons on Cu(111) to Nanographene on Cu(110): Critical Role of Substrate Structure in the Bottom-Up Fabrication Strategy**
K. A. Simonov, N. A. Vinogradov, A. S. Vinogradov, A. V. Generalov, E. M. Zagrebina, G. I. Svirskiy, A. A. Cafolla, T. Carpy, J. P. Cunniffe, T. Taketsugu, A. Lyalin, N. Mårtensson, and A. B. Preobrajenski
ACS Nano **9**, 8997-9011 (2015)

IV **On-Surface Growth of Graphene Nanoribbons *via* Organometallic Intermediates**
K. A. Simonov, A. V. Generalov, A. S. Vinogradov, G. I. Svirskiy, A. A. Cafolla, N. Mårtensson, and A. B. Preobrajenski
in manuscript (2016)

V **Effect of Electron Injection in Copper-Contacted Graphene Nanoribbons**
K. A. Simonov, N. A. Vinogradov, A. S. Vinogradov, A. V. Generalov, G. I. Svirskiy, A. A. Cafolla, N. Mårtensson, and A. B. Preobrajenski
Accepted to Nano Res. DOI:10.1007/s12274-016-1162-2 (2016)

VI **Giant Renormalization of the Quasiparticle Dispersion in Degenerately Doped Graphene Nanoribbons**
B. V. Senkovskiy, A. Fedorov, D. Haberer, M. Farjam, K. A. Simonov, A. B. Preobrajenski, N. Mårtensson, N. Atodiresei, V. Caciuc, S. Blügel, A. Rosch, N. I. Verbitskiy, M. Hell, D.V. Evtushinsky, R. German, S. Michel, R. German, T. Marangoni, P. H. M. van Loosdrecht, F. R. Fischer, and A. Grüneis
in manuscript (2016)

Reprints were made with permission from the publishers.

Comment on my own participation

All the papers included in the thesis are the result of team work and wide international collaboration. In general my position in the author lists reflects the amount of work on the respective paper and my responsibility. In papers **I - V**, I have had the main responsibility for carrying out the experiments and I have performed the data analysis. I was also responsible for writing the manuscript. For paper **VI** I took part in the angle-resolved photoemission spectroscopy measurements. I also participated in the discussion of the relevant results.

Parallel to my main work I have also been involved in other projects. However, since those are mostly outside of scope of my main research project, these are not included in the present thesis. In the following papers I was mostly involved in the experimental part, the data analysis and/or discussions of the results.

Papers not included in the thesis:

1. **Hole Doping of Graphene Supported on Ir(111) by $AlBr_3$**
   N. A. Vinogradov, K. A. Simonov, A. A. Zakharov, J. W. Wells, A. V. Generalov, A. S. Vinogradov, N. Mårtensson, and A. B. Preobrajenski
   Appl. Phys. Lett. **106**, 061601 (2013)

2. **NMR and NEXAFS Study of Various Graphite Fluorides**
   Y. Ahmad, M. Dubois, K. Guérin, A. Hamwi, Z. Fawal, A. P. Kharitonov, A. V. Generalov, A. Yu. Klyushin, K. A. Simonov, N. A. Vinogradov, I. A. Zhdanov, A. B. Preobrajenski, and A. S. Vinogradov

J. Phys. Chem. C **117**, 123564-13572 (2013)

3. **Comparative NEXAFS, NMR and FTIR Study of Various-Sized Nanodiamonds - As-Prepared and Fluorinated**
   E. M. Zagrebina, A. V. Generalov, A. Yu. Klyushin, K. A Simonov, N. A. Vinogradov, M. Dubois, L. Frezet, N. Mårtensson, A. B. Preobrajenski, and A. S. Vinogradov
   J. Phys. Chem. C **119**, 835-844 (2015)

4. **Evolution of CuI/graphene/Ni(111) System During Vacuum Annealing**
   A. V. Generalov, K. A. Simonov, N. A. Vinogradov, E. M. Zagrebina, N. Mårtensson, A. B. Preobrajenski, and A. S. Vinogradov
   J. Phys. Chem. C **119**, 12434-12444 (2015)

Abbreviations

1D, 2D, ...	one-dimensional, two-dimensional, *etc.*
***N*-AGNR**	Armchair Graphene Nanoribbon with a width *N*
ARPES	Angle-Resolved Photoemission Spectroscopy
ARUPS	Angle-Resolved Ultraviolet Photoemission
BZ	Brillouin zone
CLPES	Core-Level Photoemission Spectroscopy
DFT	Density Functional Theory
DOS	Density of States
fcc	face-centered cubic
GNR	Graphene Nanoribbon
IMFP	Inelastic Mean Free Path
IPES	Inverse Photoemission Spectroscopy
in situ	(prepared) inside ultra-high vacuum environment
ex situ	(prepared) outside ultra-high vacuum environment, respectively
MG	Monolayer of Graphite, Graphene
NEXAFS	Near-Edge X-ray Absorption Fine Structure
PES	Photoelectron Spectroscopy
PEY	Partial Electron Yield
RT	Room Temperature
SR	Synchrotron Radiation
STM	Scanning Tunneling Microscope (Microscopy)
STS	Scanning Tunneling Spectroscopy
TEY	Total Electron Yield
UHV	Ultra High Vacuum
XAS	X-Ray Absorption Spectroscopy
XPS	X-Ray Photoelectron Spectroscopy
***N*-ZGNR**	Zigzag Graphene Nanoribbon with a width *N*

Contents

1. Introduction

Nowadays, molecular electronics is regarded not only as a way of extending Moore's law beyond presently foreseen limits [1], but also as the source of exciting new opportunities for faster, smaller and cheaper electronic devices. Beyond the readily commercialized organic electronic devices, development of new *nanostructured materials* could pave the way toward industrial production of devices with dramatically reduced length scales. Ability to "*design*" functionalities and device structures with great degrees of sophistication opens a route for the development of quantum computing [2–5], molecular machines and switches [6–10], functional surfaces and nanoarchitectures [11–16] and other potentially revolutionary technologies.

Control over properties of novel nanoscale-structured systems often implies the control of their structure, composition, long-range order, *etc.* The bottom-up approach, in which *atomically precise* nanoscale structures are obtained from their molecular constituents by *self-assembled* growth or *via on-surface chemical reactions*, offers such opportunities for the design of nanostructures. Individual components play the role of the active building blocks bearing a specific property which make it possible to form the final nanomaterials.

Although the underlaying ideas of the methodology have been on the table for decades, the bottom-up construction of novel compounds was established as an independent field of research rather recently. The reasons for such significant delay are rather trivial. First of all the ability to control the sample preparation at the atomic level imposes certain restrictions on the experimental conditions. Indeed, investigation of the molecules forming certain superstructures naturally requires well-defined surfaces prepared under ultra-high vacuum (UHV) conditions to avoid perturbation of *on-surface chemical reaction* by solvents, gases, and other contaminants. Secondly, in order to study on-surface transformations, one has to have a local-probe technique allowing to obtain information on the submolecular level. Only the development of Scanning Tunneling Microscope (STM) in 1980s filled in this blank in the scientist's toolbox. In turn, the combination of the STM technique with modern X-ray spectroscopic tools addresses both geometric information and the chemical state of the species constituting the nanoarchitectures. Thus, nowadays possible changes induced by the various processes such as surface-molecule interaction or thermal annealing can be followed with remarkable level of detail. Thereby, taking into account the high potential of the bottom-up fabrication of custom materials for the future nanotechnology applications, the assembling of the molecules into various nanostructures is becoming a very active research area [16, 17].

Among all nanostructured materials, monolayers of graphite (MG, graphene) and other honeycomb carbon allotropes with reduced dimensionality, *e.g.* carbon nanotubes and *graphene nanoribbons* (GNRs), have been particularly prominent in recent years due to their remarkable structural and electronic properties [18]. The general theme of the present work revolves around GNRs - the narrow strips of graphene, several nanometers wide, which have been proposed to be used as the interconnects and components of graphene-based nanodevices, including functional elements down to single-molecule scale [19–28]. Unlike semimetallic graphene [18], where the conduction electrons are fully delocalized, the effect of quantum confinement results in the appearance of a band gap in narrow GNRs [19, 23, 29–38]. Moreover, the one-dimensional (1D) band structure of GNRs critically depends on its chirality (armchair, zigzag or intermediate edge shapes): zigzag GNRs (ZGNRs) possess a small gap between the spin-polarized edge states [30, 33, 34, 38, 39], while the narrow armchair GNRs (AGNRs) have a sizable band gap, which makes them a possible candidates for room-temperature transistor operations, enabling high on/off current ratios [22, 24, 28, 33]. The size of the band gap for both ZGNRs and AGNRs is shown to be inversely proportional to the GNRs width [23, 31, 33]. Moreover, the substitutional doping of GNRs with various heteroatoms, offers an effective way for the further modification of the GNRs electronic structure [40, 41].

It should be noted, that because of the critical dependence of the GNRs electronic properties on their geometrical shape, the ability to produce several nm wide GNRs with atomic precision is very important for potential applications. This represents a serious challenge for the top-down techniques since they provide only limited control over the width, symmetry and edge structure of the resulting GNRs [23, 38]. On the other hand, as was recently demonstrated by Cai *et al.* [42], the bottom-up route, including on-surface covalent coupling of molecular precursors is able to provide a high degree of control over the GNRs structure. Specifically, the precursors are halogen (in this case Br)-substituted and the halogen can be thermally dissociated leading to radical species which subsequently couple covalently and form GNRs upon further annealing [42]. To date, the bottom-up method is the only technique offering a full control of the GNRs atomic structure, which is, in general, determined by the molecular precursor used. For this reason, the "GNRs from bottom-up" has recently emerged as a hot research topic and during the last six years the bottom-up strategy have been employed to synthesize different types of atomically precise GNRs on noble metal surfaces [20, 21, 25–27, 42–47].

1.1 Motivation

It is clear, that when building on GNRs using bottom-up strategy one faces several problems, connected to the role of the underlying substrate.

First, the necessity to take into account the role of the metal substrate, specifically its orientation and chemical properties, in the GNRs growth process, which cannot be overemphasized. Indeed, from a variety of studies, devoted to the investigation of covalently bonded networks through surface-confined polymerization we know that, depending on the synthesis approach employed, the surface can be used as both a catalyst and/or a template to confine the polymerization reaction. Single-crystal noble metals, typically used as a substrate, are characterized by composition- and facet-dependent structural and electronic properties. For these face-centered cubic (fcc) crystals, (111) facets are closer packed than either the (100) or (110) facets. In particular, the Cu(110) surface is characterized by a two-fold symmetry and therefore atomically rough and anisotropic. In general, less dense facets are more active than close-packed ones [48] which consequently impact the intermolecular and molecule-substrate interactions leading to the formation of various molecular architectures [49–53].

In particular it was shown that for halogen-containing precursor molecules deiodination takes place spontaneously on Cu(111), Ag(111) and Au(111)[49, 54, 55]. On the other hand, at room temperature bromine is fully split off from such molecules on Cu(111) [51, 56–59], partially on Ag(111) [51, 55], and not at all on Au(111) [42, 52, 55, 60, 61]. Moreover, on copper and silver surfaces the molecular radicals often form metastable organomatallic structures [51, 55–58, 62, 63], while on gold, organometallic bonds are occasionally observed [64]. Furthermore, the catalytic properties of Cu(111) and Cu(110) surfaces can be used for the direct surface-assisted activation of C-H bonds in the organic building blocks [65–67], while no such effect was observed on Au(111) surfaces. Nevertheless, Zhong and co-workers [68] observed a linear alkane polymerization on Au(110) with alkane monomers forming linear molecular chains within the Au(110)-(1×3) channels, while no such polymers can be produced on the Au(111) surface. The guiding properties of the Cu(110) substrate for the polymerization process were also demonstrated by the formation of ordered para-polyphenylene molecular wires, oriented along the densely-packed $[1\bar{1}0]$ direction, from 1,4-diiodobenzene precursors [54], and by the creation of oriented metal-organic oligomers *via* surface-mediated reaction between various porphyrins [67]. Therefore, not only the catalytic properties of the substrate are important for the on-surface synthesis, but also the influence of adsorption energies, diffusion barriers, and lateral interactions of molecular precursors is important.

Recently, by comparing the formation of covalently bonded polymer networks on Cu(111), Au(111), and Ag(111) surfaces, Biery *et al.* [49] have demonstrated that the resulting structure is determined by the balance between diffusion and intermolecular coupling. On Cu(111) the energy barrier for diffusion appeared to be significantly higher than the one for covalent intermolecular bond formation, while Ag(111) provides the reverse relation. Generally, it was shown that relative to other surfaces Cu(111) presents more reactive

sites and a reduced mobility of the adsorbed molecules, while Ag(111) exhibits properties between those of Cu(111) and Au(111). Therefore, a detailed understanding of the substrate effect on the bottom-up synthesis of nanostructures, and GNRs are not an exception, appears to be an obligatory condition for the truly controllable on-surface growth.

The **second** problem concerns the influence of the substrate on the electronic structure of the produced GNRs. To date both experimental indications and theoretical calculations support a picture of weak hybridization and lack of charge transfer for AGNRs adsorbed on Au(111) [43, 69]. The low-energy states localized near zigzag edges, however, interact even with the noble Au(111) surface, as evidenced from the qualitative disagreement between experimental data and theoretical predictions for free-standing GNRs [25]. One can expect, that when adsorbed on more interacting metal surfaces, the effect of interaction of the graphene ribbon with the substrate cannot be neglected. Indeed, a detailed inspection of the electronic structure of 7-AGNRs on Ag(111) [45] (where $N = 7$ is the number of carbon atom pairs across the ribbon) reveals that the electronic structure of the nanoribbons is significantly influenced when 7-AGNRs are adsorbed on Ag(111) - the unoccupied bands of the nanoribbon become partially occupied, indicating a weak chemisorption nature of the ribbon-substrate interaction. An even more significant impact of the substrate was emphasized very recently for poly(para-phenylene) (PPP) nanowires, which can be considered as an extreme case of AGNRs (namely 3-AGNRs), grown on Cu(110) substrate [70]. In particular, it was shown that hybridization between π-states of the polymer and copper states results in metallic behaviour of the nanowires. Interestingly, this effect was not observed for the same polymer wires grown on a Cu(111) substrate [71], which was attributed by the authors of [70] to the fact that polymers are aligned in such a way as to be commensurate with the Cu(110) substrate, thus maximizing the interaction with the substrate in comparison to the PPP/Cu(111) interface.

The "metal contact" problem can also be viewed from the other side. Insufficient control over the doping level in freestanding graphene contacted to metal leads can significantly limit the performance and reproducibility of nanodevices [72–75]. Transport properties in the GNR-based devices will also be affected by metal contacts. For example, charge doping by metal-induced gap states has been predicted theoretically in different GNR/electrode systems [76]. Apparently, this affects the I-V characteristics of the GNR channel across two electrodes, and various interesting effects may appear depending on the contribution of the GNR sub-bands to the charge transport [77]. Therefore it is of crucial importance to explore the effects of metal-GNR interaction by investigation of the interfaces of GNRs with substrates more active than Au. Logically, our interests can be extended beyond interaction of GNRs with coinage metals, *e.g.* interfacing GNRs with alkali metals can be expected to

be a perspective way to modify electronic structure of GNRs as was confirmed for graphene [78, 79].

Surprisingly, up to present day there exists little experimental insight into the role of the substrate in on-surface chemical routes toward GNRs formation and effects of GNR-metal interaction on the electronic structure of the final product. In the vast majority of experimental studies, focussed on the bottom-up preparation of GNRs and investigation of their electronic structure, the ribbons were in contact with gold surfaces, including Au(111) [20, 21, 25–27, 42, 46, 47] and its vicinal Au(788) surface [43, 44], where aligned AGNRs on (111) facets can be grown. Moreover, so far the electronic structure of GNRs was mainly modified *via* the introduction of changes in the precursor molecule [27, 37, 41, 80, 81] and much less is known regarding the interaction of GNRs with active metals. Taking into account the technological demand for controlled preparation of atomically precise graphene nanoribbons with well-defined properties, the present thesis is focused on the investigation of the role of the underlying metal substrate in the process of building GNRs using a bottom-up strategy and on the changes in the electronic structure of GNRs induced by the GNR-metal interaction.

In **Paper I** the effect of the substrate reactivity on the growth dynamics and structure of AGNRs prepared on inert Au(111) and active Cu(111) is systematically studied by the combination of spectroscopic methods and STM. The significant impact of substrate activity on the GNR growth dynamics is demonstrated.

Paper II is, in turn, focused on deeper insight into the growth mechanism of GNRs on Cu(111). Unlike the standard mechanism of GNRs formation on Au(111), this process on Cu(111) is further complicated by the active role of the substrate in the on-surface reactions, which leads to the formation of the organometallic intermediates.

Paper III continues to consider the role of the molecule-substrate interaction in the bottom-up fabrication strategy of GNRs. By performing experiments on Cu(111) and Cu(110) surfaces, combined with Density Functional Theory (DFT) calculations, we show that a change of the balance between molecular diffusion and intermolecular interaction on Cu(110) significantly affects the on-surface reaction mechanism.

In **Paper IV** we demonstrate that, unlike for the inert Au(111) substrate, but similar to the more active Cu(111) substrate, GNR's growth on the Ag(111) surface involves the formation of the organometallic chains based on carbon-metal-carbon bonds. Our studies indicate that the structure of the organometallic chains is different on the Ag(111) and Cu(111) surfaces. The temperature regimes for the organometallic to covalent bond transformation on Ag(111) were found.

Paper V explores changes in the electronic properties of nanoribbons contacted with copper *via* its intercalation beneath 7-AGNRs grown on the Au(788) surface. We take advantage of combining spectroscopic experimental

techniques, including angle-resolved photoelectron spectroscopy, with STM to follow the intercalation process. We investigate structural and electronic properties of the 7-AGNRs/Cu/Au(788) system and its temperature evolution. We show that intercalation of copper leads to significant electron injection into the nanoribbons, thus contributing to the design of novel GNR-based devices.

A similar way to model the GNR-metal interface is implemented in **Paper VI** to investigate the effect of interaction with lithium on the electronic structure of 7-AGNR prepared on the Au(788) surface. It is demonstrated that *via* lithium doping, 7-AGNRs can be effectively transformed from a semiconductor into a metal due to the partial filling of the conduction band. The band gap of Li-doped GNRs is reduced and the effective mass of the conduction band carriers is increased.

2. Different strategies towards covalent molecular nanosystems

Several approaches have been investigated for the formation of molecular-based nanostructures, each suited for different applications. The on-surface molecular self-assembly is known to be a promising route towards formation of highly-ordered two-dimensional (2D) supramolecular structures with low defect density, composed of molecular blocks held together by *non-covalent bonds*. Such an approach is of particular importance in the fabrication of large-scale modular nanoarchitectures with nanoscale control due to the intrinsic defect correction, also known as self-healing, provided by the reversibility of the exploited interactions. Suitable bonding strategies include hydrogen bonds, van der Waals interaction and metal-organic coordination [11–13, 16]. Self-assembled nanostructures, therefore, have a great potential for the manufacturing of surfaces with tunable functionalities (*e.g.* electronic, magnetic, optic, catalytic *etc.*)[14, 15, 82–84]. However, self-assembly does have some limitations, most notably that the intermolecular interaction is relatively weak and therefore leads to fragile structures, not applicable for effective intermolecular charge transport. In turn, interconnection of the molecules in a controlled way directly on a surface through robust *covalent bonding* offers a way to overcome this limitation.

In contrast to supramolecular structures, the covalently bonded molecular building blocks can facilitate efficient charge transport as well as high thermal and mechanical stability which makes covalent coupling a promising approach for the design of components for nanotechnological applications [6, 9, 10, 19–21]. In principle, the last few years revealed that a variety of well-known reactions from "in-solution chemistry" can be applied for the synthesis of covalently linked structures on surfaces. Moreover, the co-existence of reagents and the substrate with certain directional and catalytic properties can favor some reactions observed only in a 2D confined geometry [17, 68, 85–88]. Carbon-carbon bond forming reactions are certainly the most important ones for the formation of covalent nanostructures. In this section, different examples of most wide-spread C-C coupling reactions will therefore be discussed with a focus on the covalent coupling of halogen-substituted building blocks, which are used for the bottom-up production of GNRs.

2.1 C-C coupling through C-X (X = Br,I) activation: Ullmann reaction

The Ullmann-type coupling reaction of dehalogenated monomers underlies the bottom-up mechanism of GNRs formation, thus a detailed discussion of this polymerization reaction is important within the framework of the present work.

More than 100 years ago, in 1901, Ullmann and Bielecki discovered the coupling reaction for aryl halides in the presence of a copper catalyst at high temperature (above 200°C) [89]. Since that time it has been long employed by chemists to generate a C-C bond between two aromatic units. Thus, the Ullman reaction was among the first coupling reactions from solution chemistry carried out on a single crystal copper substrate under UHV conditions [90]. The latest studies, focused on the identification of the exact on-surface reaction pathway for iodobenzene and bromobenzene on Cu(111) [54, 58, 59], have revealed that the C-C coupling occurs in two steps (Figure 2.1). For X = Br,I at the first step the dehalogenation of the precursor molecules takes place subsequent to deposition at room temperature, resulting in dehalogenated monomers and halides chemisorbed on the surface. The molecular intermediates are stabilized by the formation of bonds to the surface at their dehalogenated sites. It should be noted, that on Cu(111) the formation of organometallic heterostructures stabilized by Cu atoms and based on carbon-metal-carbon bonds is often obtained at the first reaction step [51, 56–58]. Further, upon temperature activation, organometallic bonds can usually be converted into covalent ones.

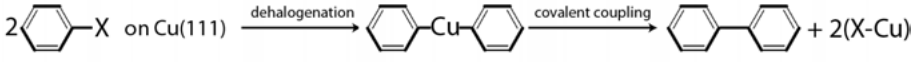

Figure 2.1. Reaction scheme of on-surface Ullmann coupling between two aryl halides resulting in the formation of biaryl and copper halide. "X" typically stands for I or Br.

Recent studies have shown that, with certain differences from the prototypical copper surface, analogous (Ullmann-type) coupling reactions can be performed also on (111) facets of less reactive transition metals (TMs) belonging to the 11th group, namely silver [49, 51, 91] and gold [42, 49, 52, 55, 60, 61]. Figure 2.2 (a) illustrates the general concept of covalent assembly on surfaces using halogen-substituted molecular precursors. Depending on the number of active sites in the precursor molecule it can be used for the tailored bottom-up synthesis of 1D and 2D nanostructures. In general, the reaction path is analogous to the Ullmann reaction and exploits the fact that the halogen atoms are more easily abstracted than their hydrogen counterparts. This results in species, featuring unsaturated carbon atoms that establish the covalent bond after an intermediate diffusion process.

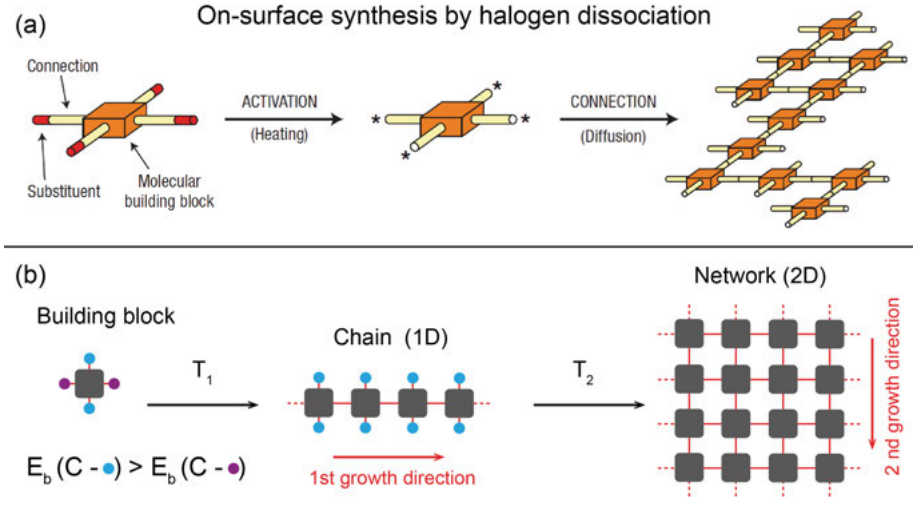

Figure 2.2. (a) Concept of the formation of covalently bound networks by connecting activated molecular building blocks. *Copied from* [92]; (b) Scheme of sequential activation mechanism using monomers with unequal functional groups having different dissociation energy barriers (E_b).

Since 2007, when formation of 0D, 1D and 2D tetraphenylporphyrin assemblies on Au(111) was for the first time demonstrated by L. Grill *et al.* [92], this strategy was a vast source of inspiration for novel developments [17, 82, 93]. To date, the molecular building blocks are often functionalized with bromine [42, 51, 56–58, 60, 91], iodine [49, 54], or a combination of both [55, 94]. Chlorine and fluorine, in turn, are rarely used as a halogen substituents in the context of on-surface polymerization [95, 96].

The bond dissociation energy is specific for each type of halogen, resulting in different activation temperatures for the dehalogenation. In this respect, DFT simulations suggest that the energy barriers are around 0.3 eV smaller for deiodination than for debromination on Au(111), Ag(111) and Cu(111) [97]. Accordingly, in 2012 Lefferentz and co-workers [94] have shown that additional flexibility can be added to the method by proper design of the precursor molecule, which can contain unequal active "legs" (Figure 2.2 (b)). The difference between the dissociation energy barriers (E_b) for the halogen atoms allows to perform sequential dissociation of the C-X bonds and thus create sophisticated multi-component molecular nanostructures by using various substrates, precursor molecules and varying the kinetic parameters of the on-surface reaction [55].

As was mentioned above, the proper selection of the substrate also plays an important role for the on-surface Ullmann-type reaction. DFT calculations of the Ullmann coupling on (111) facets of different TMs indicate that both the

Table 2.1. *The summary of experimental data, showing the dissociation progress and resulting intermediate structures after room temperature (RT) deposition of various precursor molecules having halogen side groups on Au(111), Ag(111) and Cu(111).*

Single crystal substrate	Debromination progress	Deiodination progress
Au(111)	No⇒Self-assembly	Complete⇒ Covalent network
Ag(111)	Partial⇒Protopolymer[a]	Complete⇒Protopolymer
Cu(111)	Complete⇒Protopolymer	Complete⇒Protopolymer

[a] Protopolymer is the name for the organometallic structure or surface-stabilized structure. The table is based on the following papers: [42, 51, 52, 55–63]

reaction energy and the halogen dissociation energy barrier increase for debromination and deiodation in order of Cu(111), Ag(111), and Au(111)[97]. Table 2.1 summarizes the existing experimental data on the deiodiation and debromination of various halogen-substituted molecules after RT deposition on Au(111), Ag(111) and Cu(111). The resulting molecular structure is additionally specified for each case. After dehalogenation on copper and silver the formation of metastable organometallic structures, where molecular radicals are bound through C-metal-C bonds, is commonly observed. It was shown, that on Cu(111), the controlled formation of the covalent structure is not always possible, since C-Cu bonds in the protopolymer appear to be stronger than the covalent bonds of the covalent backbone [51]. Therefore the nature of metal surfaces has a clear impact on the bottom-up process. To summarize, the two main factors are the mobility of the precursor molecules and the surface reactivity [49]: a copper surface is more reactive, but does not allow enough diffusion, while on gold the molecule can freely diffuse, but additional temperature activation of the dehalogenation process may be required.

Figure 2.3 (a) represents the fist reaction step of the AGNR formation from 10,10'-dibromo-9,9'-bianthracene (DBBA) molecular precursors on Au(111), realized in the pioneering work by Cai *et al.* [42]. The illustrated reaction is identical to other Ullmann-like processes for Br-substituted units on Au(111) which were discussed above: temperature activated dehalogenation and further polymerization results in formation of polymer chains, constituted from anthracene subunits. Steric hindrance between hydrogen atoms of adjacent anthracenes rotates the latter around the chain axis which manifests itself as an alternated protrusion pattern in the STM image (Figure 2.3 (b)). Such long oligomers play a role of new precursors for further formation of AGNRs on Au(111). Remarkably the oligomerization of 9,10-dibromoanthracene (one anthracene with two bromine atoms - one in the middle of each zigzag side) does not occur either on Au(111) or on Cu(111), probably due to intermolec-

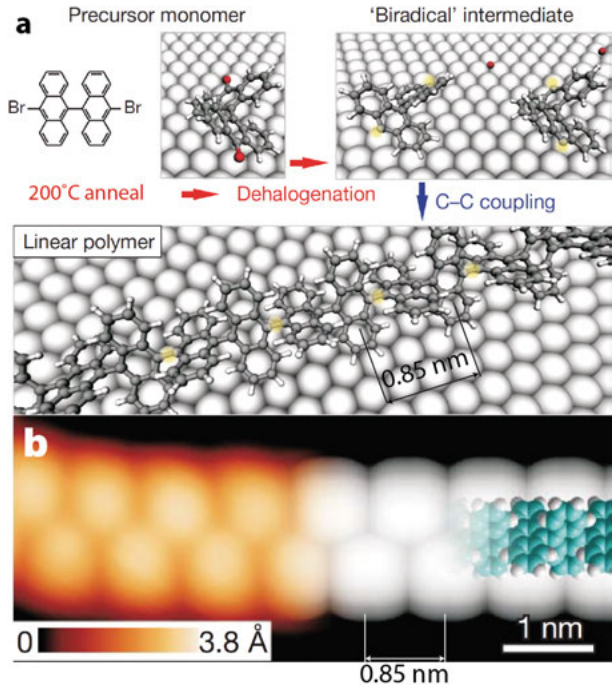

Figure 2.3. (a) The schematics illustrate the first stage of AGNRs formation on Au(111) - Ullmann-type covalent coupling reaction of DBBA precursors upon 200°C anneal; Grey - carbon, white - hydrogen, red - Br atoms; (b) The high-resolution STM image showing polymer chain as alternated protrusions from anthracene lobes pointing upwards and the superimposed ball and stick model. The 0.85 nm periodicity of the structure is in agreement with the structural model. *Image is based on the data presented in* [42].

ular repulsions of aromatic hydrogens belonging to neighboring molecular units, lying flat on the metallic surface (own data, unpublished).

2.2 C-C coupling through cyclodehydrogenation

The next important reaction, enabling the on-surface growth of GNRs, is cyclodehydrogenation. In solution it is widely used to obtain large fused polyaromatic hydrocarbons from various oligoaryles [98] and involves the oxidative C-C coupling of two neighboring C-H groups (formally by the loss of H_2) with subsequent cyclization in the presence of Lewis acids. Luckily, this C-C bond formation mechanism can also be implemented on metal surfaces for synthesis of polyaromatic hydrocarbons from polymer precursors, which was firstly realized in 1999 by Weiss *et. al.* [99] on a Cu(111) substrate (Figure 2.4).

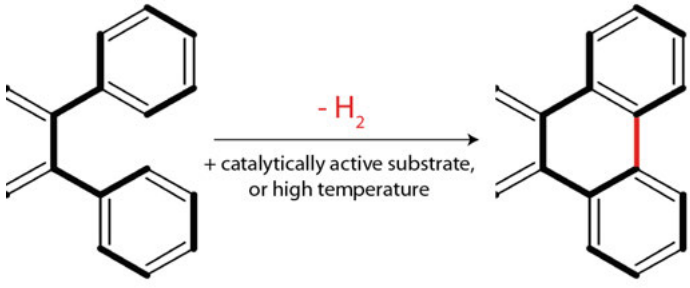

Figure 2.4. Conceptual representation of an on-surface cyclodehydrogenation reaction, leading to fused polyaromatic fragments.

Nevertheless, the first detailed investigations of surface-assisted cyclodehydrogenation were performed significantly later, when the possibility to grow aromatic hemispheres on Ru(0001) [100] and fullerenes on Pt(111) [101] from their planar precursors have been demonstrated. In the next several years cyclodehydrogenation was used to grow GNRs on Au(111) [20, 21, 25–27, 42, 46, 47] and Ag(111) [43], nanographenes on Cu(111) [65] and other fascinating nanoarchitectures on TM surfaces [66].

Treier and colleagues [65] have investigated the reaction path for surface-assisted cyclodehydrogenation of polyphenylene on Cu(111). The process takes place at 180°C and results in the formation of flat tribenzocoronene units. By a combination of STM measurements with detailed DFT calculations, the authors were able to follow the cyclodehydrogenation process and show that on active Cu(111) cyclodehydrogenation occurs through several surface-stabilized intermediates, which underlines the catalytic role of Cu(111) in the reaction. On the other hand, their theoretical simulations show, that the cyclodehydrogenation reaction can also proceed (but, probably, in a different way) on an inert substrate, although higher activation temperatures may be required.

It should be mentioned, that apart from cyclodehydrogenation (intramolecular oxidative C-C coupling), another related reaction, called dehydrogenative polymerization (intermolecular oxidative C-C coupling) exists. The dehydrogenative polymerization process formally involves the same catalytic or thermal activation of neighboring C-H groups, but located on different precursor molecules [66, 102]. The impact of the balance between surface reactivity and mobility of precursor molecules on the bottom-up formation of polymer structures through dehydrogenative reactions was recently demonstrated by Pinardi *et al.* [66]. In general, it was shown, that strong coupling of precursor molecules to an active substrate blocks the diffusion and, accordingly, the cyclodehydrogenation reaction within individual building blocks dominates. On the other hand, a weak coupling of precursors to the inert substrate allows

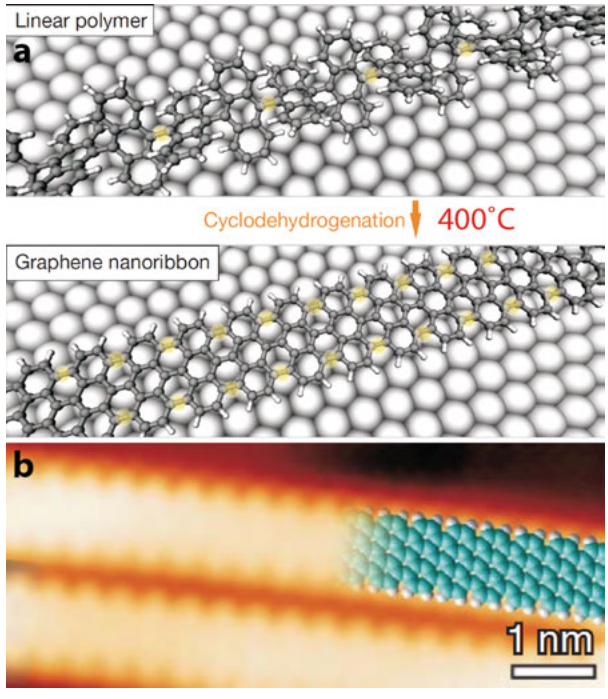

Figure 2.5. The schematics illustrate the formation of AGNRs on Au(111) from polyphenulene precursors through thermal-activated (400°C) cyclodehydrogenation; Grey - carbon, white - hydrogen atoms; (b) A high-resolution STM image showing two AGNRs and the superimposed structural model. *The image is based on the data presented in* [42].

diffusion and therefore individual molecules can fuse together, thus forming big covalent structures *via* dehydrogenative polymerization (along with simultaneous cyclodehydrogenation).

As mentioned above, cyclodehydrogenation is the next step, necessary for the production of GNRs on Au(111). According to [42], annealing at 400°C of the polyanthracene, previously described in Section 2.1 (Figure 2.3), causes cyclodehydrogenation to occur within the polymer chain thus leading to the formation of expected AGNRs (Figure 2.5).

2.3 Other types of on-surface covalent coupling reactions

It is worth to note, that the investigation of various on-surface reactions, leading to the formation of covalent structures (also including heterostructures), is a rapidly developing and very broad area of surface science. The most interesting strategies for the chemical reactions on noble metal surfaces, allowing

formation of extended polymeric networks with C-C bonding distinct from graphene, include: (i) homo-coupling of terminal alkynes (*Glaser-Hay reaction*) [85–88, 103]; (ii) C-C *Sonogashira coupling* of haloaromatic compounds with terminal alkynes [104]; (iii) alkane dehydrogenative polymerization [68] and others. Moreover, structures containing heteroelement bonds can also be produced *via*, for example, imine formation (C-N double bond) [105–107], boronic acid condensation (C-B-O bonds)[85, 108], metal-organic bonding [56, 67, 109] *etc*. Alltogether this present an extremely rich toolbox for the exciting "molecular origami" game. On the other hand, this thesis does not aim to cover all the diversity of on-surface reactions, since they are lying out of scope of GNRs formation. The interested reader can refer to several recent reviews on the topic [17, 82, 93] and to the references above.

2.4 Kinetics of on-surface transformations

In the previous sections we have already briefly touched upon the importance of kinetic parameters for the on-surface reaction pathway and the resulting structure (see Section 2.1). Indeed, the formation of covalent bonds is usually an irreversible process and thus poorly chosen reaction conditions can lead to the formation, either of structures with high defect densities, or even some system completely different from the target one. Therefore, the conception of polymer structures growth and, in particular, the influence of kinetic factors on it, is worth being considered in more detail.

In principle, independently of the chosen mechanism, two different routes for the polymerization reactions can be distinguished: upon activation of polymerization process, the building units either directly couple with each other under the release of byproduct [42, 54] or they form surface-stabilized radicals [51, 56, 87, 110]. In the latter case subsequent coupling steps exist: typically upon longer annealing times the surface-stabilized species can bind to surface adatoms, forming metastable organometallic structures [56], or directly interlink by covalent bonds [87]. In turn, organomellic structures can be converted to the covalent ones, but additional temperature activation is always required [51, 57]. As we can see, in both cases the reaction occurs over several steps and, therefore, the reaction rate is limited by the rate of the slowest reaction step [111]. In general, the reaction rate constant ν of some thermally activated process can be obtained by the Arrhenius equation, where T is the temperature, E_b is the reaction barrier for the corresponding process, k_B - Boltzmanns constant, and A is an empirical factor:

$$\nu = Ae^{-E_b/k_BT}. \tag{2.1}$$

For example, for the on-surface Ullmann-type coupling, the reaction rate for polymer formation depends mainly on the dehalogenation and coupling

steps, but also the diffusion on the surface (which can also be considered as a temperature activated process with corresponding diffusion barrier) have to be taken into account [55]. In turn, the rate of cyclodehydrogenation is governed by the reaction of C-H bond cleavage having smaller E_b on catalytically active surfaces [66].

To sum up, all these factors must be taken into account when one is selecting conditions for the on-surface synthesis of nanostructures, including GNRs.

3. Graphene nanoribbons: electronic structure and experimental progress

The graphene nanoribbon is the central object of the research work, included in the present thesis. Therefore this chapter summarizes the most important electronic properties, predicted for GNRs as well as the recent experimental progress in their atomically controlled preparation.

3.1 Electronic structure of graphene nanoribbons

As was mentioned above, the intensive investigation of GNRs is inspired by their remarkable electronic properties, making narrow GNRs a promising material for potential applications in nanodevices (see Chapter 1). Below, the most important electronic properties predicted for GNRs (some of which have already been proven experimentally) will be discussed in more detail.

The terminology is the best starting point to facilitate the further understanding of this section. In general, a GNR can be thought of as a long strip cut out of a graphene sheet (Figure 3.1). Considering various crystallographic directions, along which the GNR can be cut out, there are different types of GNRs which are most intuitively classified by their edge structure, width and length. To some extent, most of the electronic properties of the real finite GNRs can be quite accurately described by fictitious infinitely long GNRs [26, 34]. Therefore, for simplicity the GNRs will be further considered as infinitely long graphene strips. Returning back to the nomenclature, it is analogous to the one for carbon nanotubes: the orientation of the GNR axis within the "parent" graphene sheet is referred to as "chirality" and is defined by the vector $\mathbf{T} = m \times \mathbf{p} + n \times \mathbf{q}$, connecting crystallographically equivalent sites along the GNR edge, and defined in the graphene lattice coordinate system ($\mathbf{p}$,$\mathbf{q}$), $|\mathbf{p}| = |\mathbf{q}| = a_{gr} = 2.46$ Å(a_{gr} - the lattice constant of graphene). Alternatively, the chiral angle (θ) can be used to characterize the GNR axis direction and, therefore, its chirality. Thus, for the case of chiral (4,1) GNR, outlined by the red border in the top picture of Figure 3.1, $\theta = 10.9^{\circ}$. Two extreme cases, characteristic for the most prominent types of GNRs, are defined by $\theta = 0^{\circ}$ or $\theta = 30^{\circ}$ (green and cyan arrows at Figure 3.1) resulting in GNRs with zigzag or armchair edges, respectively.

The width of the ribbon (ω) is often specified by a characteristic number N, which denotes the number of carbon atom pairs across the ribbon for AGNRs or the number of zigzag lines parallel to the edge direction for ZGNRs,

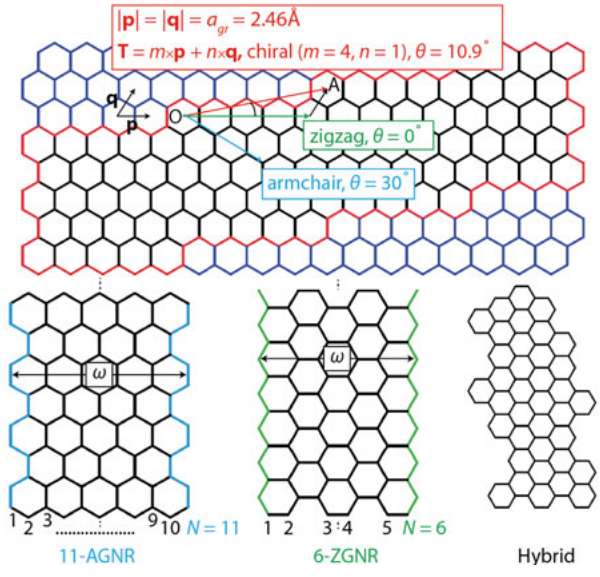

Figure 3.1. Constructing an atomic model of GNRs with different edge configurations. The chiral (4,1) GNR is outlined by red. The chirality (*m*,*n*) is defined by the components of vector **T** = OA in the coordinate system of the graphene sheet (**p**,**q**) or by the chiral angle θ. For armchair and zigzag edges θ is 30° or 0°, respectively. The bottom part illustrates the width (ω) determination for GNRs with armchair and zigzag edge shapes: 11-AGNR, which has 11 carbon atom pairs making up its width, and 6-ZGNR, having 6 zigzag lines parallel to the edge direction. Also, the example of GNR with arbitrary edge structure is presented (hybrid GNR).

as illustrated at Figure 3.1 for the examples of 11-AGNR and 6-ZGNR. In principle, the diverse family of GNRs is not limited to graphene strips, having regular edge shape. GNRs with irregular edge structure are referred to hybrid GNRs, possessing a mixed, partially armchair, partially zigzag character[1], which is also reflected in their electronic structure. Nevertheless, for potential applications, AGNRs and ZGNRs, each having a well-defined edge shape and, therefore, unique electronic properties, are the most interesting ones.

Since GNRs are just geometrically terminated MG layers, some features of their electronic structure can be predicted from that of the 2D graphene sheet. The tight-binding approximation (TBA), using the C 2s and C 2p atomic orbitals as a basis set [113], offers a very simple way to calculate the π-band dispersion of MG [114]. Each of the carbon atoms within the graphene layer is sp^2-hybridized and linked with its three neighbors *via* strong covalent bonds. The corresponding σ-bands (bonding and anti-bonding) are split to high en-

[1]It should be noted, that the edge of chiral GNRs can also be considered as a superposition of armchair and zigzag regions, but unlike hybrid GNRs, they are regularly intermixed in a certain fixed proportion.

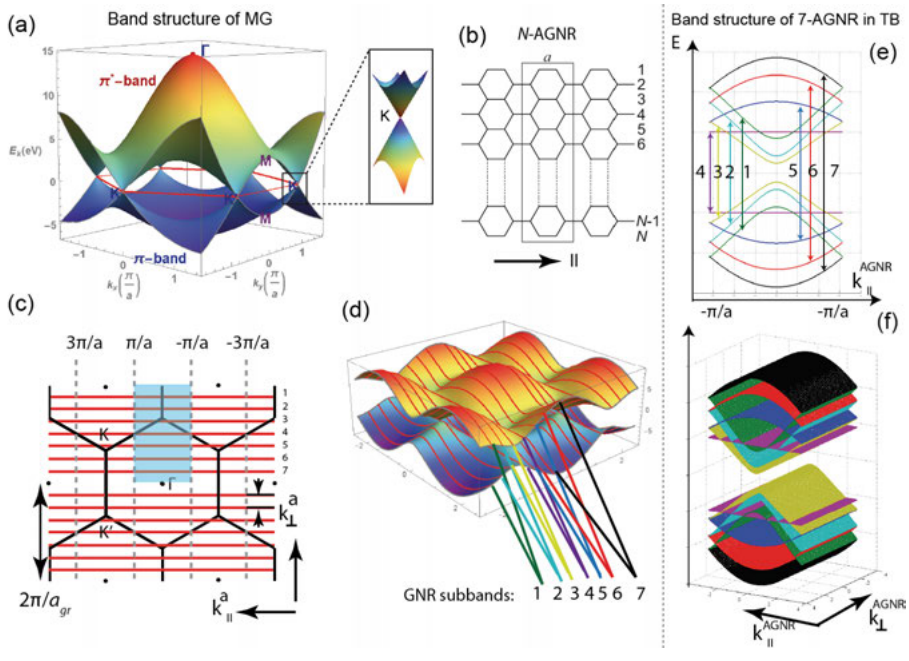

Figure 3.2. Derivation of the band structure of AGNRs from the band structure of MG in the tight binding approximation. (a) The calculated dispersion of the valence (π) and conduction (π^*) bands of free-standing graphene. *Copied from* [112]. Both bands overlap only at the **K** and **K'** points of the hexagonal BZ, forming Dirac cones with linear dispersion. (b) The structure of graphene nanoribbons with armchair edges. The black rectangle defines the unit cell with translational periodicity $\boldsymbol{a}$, corresponding to the armchair edge structure. (c) Brillouin zones of graphene (black hexagons) with discretized spectrum of the 7-AGNR (red lines) along $k_{\perp}^{AGNR}$ direction. Dashed lines indicate borders of the one-dimensional BZs of AGNR along $k_{\parallel}^{AGNR}$. The semitransparent rectangle highlights the BZ of the nanoribbon, which includes all inequivalent subbands. (d) 3D plot of the bulk graphene band structure calculated within the TBA. Red lines correspond to the descrete values of the transverse wavevector $k_{\perp}^{AGNR}$ for $N = 7$ AGNR. Colour-coded lines and indexes show 7 pairs of subbands. (e) Band structure of 7-AGNR within TBA, which is equivalent to the projection of the slices of the 3D plot onto the $k_{\parallel}^{AGNR}$ direction. Subband indexes are also shown. (f) Plot, illustrating the one-dimensional character of the GNR's band structure.

ergy values and can therefore be neglected, when investigating the low energy band structure. The remaining valence electron in the p_z orbital leads to the formation of another pair of bands, the so-called π-bands. Therefore, within the TBA it is possible to derive the band structure of graphene as [114]:

$$E(\mathbf{k}) = \pm\gamma_0\sqrt{1+4\cos\left(\frac{k_y a_{gr}}{2}\right)\cos\left(\frac{\sqrt{3}k_x a_{gr}}{2}\right)+4\cos^2\left(\frac{k_y a_{gr}}{2}\right)}, \quad (3.1)$$

where k_x, k_y are the momentum components, a_{gr} - the lattice constant of graphene and γ_0 is a value of the overlap integral for the corresponding atomic orbitals.

The result is presented in Figure 3.2 (a). As can be seen, the upper (conduction) and lower (valence) bands are degenerate at the 6 points **K** (**K'**), located in the corners of the hexagonal graphene Brillouin zone (BZ)[2]. Moreover, at each corner the electronic bands $E(\mathbf{k})$ show a linear **k** dispersion relation and form so-called Dirac cones (see the inset in Figure 3.2 (a)). In this regime the π-band electrons and holes behave like massless Dirac particles, hence the name [18]. As it will be demonstrated below, the electronic band structure of graphene nanoribbons can to a large extent be understood in terms of one-dimensional cuts in the two-dimensional band structure of graphene. While this strategy is outdated, it is still widely used as a qualitative illustration of the origin of the GNRs band structure.

Since AGNRs, and specifically 7-AGNRs are the main objects of the present work, the discussion will be focused on them. The atomic structure of N-AGNR is schematically shown in Figure 3.2 (b). The AGNR is characterized by the periodicity $\boldsymbol{a}$ in the direction parallel to the armchair edge and has a finite width in the perpendicular direction. Since it is possible to obtain a graphene layer by placing AGNRs side-by-side (if we do not take into account hydrogen atoms terminating the ribbon's edges), the boundary conditions at the armchair edge are compatible with the unperturbed electronic structure of graphene [116]. As a consequence, the band structure of N-AGNRs can be qualitatively obtained by slicing the band structure of graphene at N equidistant wave numbers. It can be shown [116], that in the general case of N-AGNR the confinement of electrons in the direction perpendicular to the GNR axis restricts the corresponding wavevector component to discrete values $k_{\perp}^{AGNR} = \pm 2\pi r/(N+1)a_{gr}$, $r \in 1\ldots N$. As a result, in **k**-space the BZ of graphene folds into the BZ of N-AGNR having the size equal to $2\pi/a = 1.46$ Å^{-1} in the $k_{\parallel}^{AGNR}$ direction and $2\pi/a_{gr}$ in the $k_{\perp}^{AGNR}$ direction, which includes all inequivalent subbands. As an example, Figure 3.2 (c) shows how the 1D Brillouin zone of 7-AGNR, which includes $N = 7$ inequivalent subbands, can be obtained

[2]For information about the theoretical background and terminology related to the band structure of solids, the interested reader is referred to the literature on the topic, *e.g.* [115].

from the 2D graphene Brillouin zone. For a better visualization, Figure 3.2 (d) illustrates the π-band electronic structure of MG calculated within the TBA, sliced by the parallel lines at the indicated values of $k_{\perp}^{AGNR}$. The resulting 1D band structure of 7-AGNRs (Figure 3.2 (e)) can be considered as a projection of the cuts of the graphene band structure onto the $k_{\parallel}^{AGNR}$ direction (ΓM for graphene). The highest occupied band is always given by the cut that comes closest to the Dirac point of the graphene BZ. The whole derivation of this can be found in Ref. [116]. In the armchair case, Equation 3.1 reduces to the system of one-dimensional equations with discrete $k_{\perp}^{AGNR}$, describing each pair of subbands:

$$E(\mathbf{k}_{\parallel}^{AGNR}) = \pm\gamma_0\sqrt{1+4\cos(p)\cos\left(\frac{\sqrt{3}k_{\parallel}^{AGNR}a_{gr}}{2}\right)+4\cos^2(p)}, \quad (3.2)$$

where $p = k_{\perp}^{AGNR} \times a_{gr}/2$.

It should be noted that the value of $k_{\perp}^{AGNR}$ is not defined for AGNRs since electrons are confined in that direction. As a result, the band structure of AGNRs (actually this applies to all types of GNRs) is purely one-dimensional (if we do not take into account the effects of interaction between the GNRs on the substrate [70]). In principle that means that each of the subbands disperses only in the $k_{\parallel}^{GNR}$ direction, as it shown in Figure 3.2 (f).

By analogy with AGNR, in ZGNR the confinement of electrons takes place in the direction perpendicular to the zigzag axis and the corresponding wavevector component $k_{\perp}^{ZGNR}$ (which is collinear with $k_{\parallel}^{AGNR}$) has descrete values. At the same time the boundary condition for the zigzag edge is incompatible with the graphene lattice (Figure 3.3 (a)). Despite this it was shown that for ZGNRs the spectrum of all bands except one can be still obtained by slicing the band structure of graphene. However, these slices do not follow exactly straight lines anymore [116]. The BZ of ZGNR is shown in Figure 3.3 (b) and includes all inequivalent states in **k**-space[3]. Therefore the band structure of GNRs having zigzag edges is predicted by projecting the cuts of graphene's band structure onto the $k_{\parallel}^{ZGNR}$ direction. From Figure 3.3 (c), showing the 3D band structure of graphene with the arbitrary slices on it, the clear difference between band structures of zigzag and armchair ribbons is becoming obvious. Indeed, unlike the case of AGNRs, the dispersion relations, originating from the graphene's **K** points, are expected to appear around $|k_{\parallel}^{ZGNR}| = 2\pi/3z$, *i.e.* not in the centre of the 1D BZ. Figure 3.3 (d) depicts the band structure of 6-ZGNR, calculated in the TBA [117]. As can be seen, the projected graphene-derived subbands almost reproduce the band structure of zigzag ribbon. Nevertheless at the edges of BZ a pair of flat metallic states is found instead of a

[3]It is easy to show that the sizes of BZ for AGNR and ZGNR are the same, being half as large as the hexagonal BZ of graphene.

Dirac cone. As will be explained in more detail below, these states are exclusively found in ZGNRs and localized at the zigzag edges which is why they are referred to as *edge states* [30, 33, 117, 118]. This pair of localized subbands therefore cannot be obtained from the band structure of graphene by analogy with other N - 1 extended states.

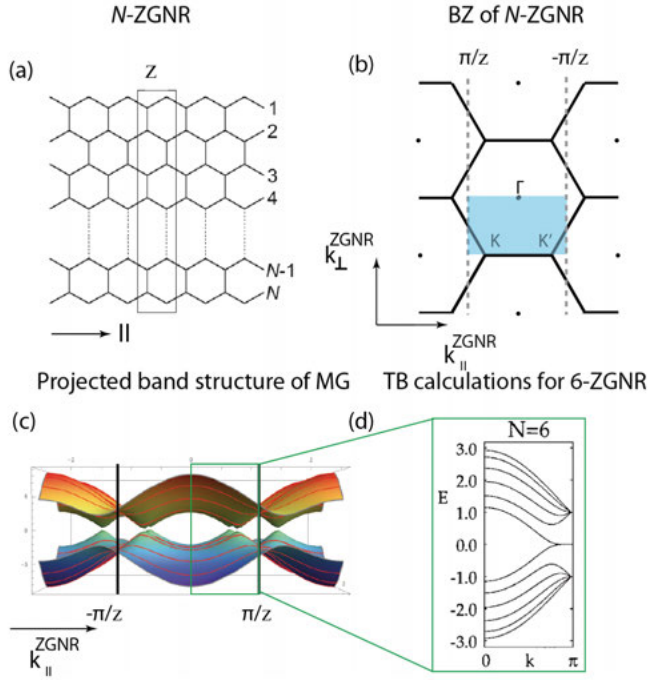

Figure 3.3. (a) Structure of graphene nanoribbons with zigzag edges. The black rectangle defines the unit cell with translational periodicity $z = a_{gr}$, corresponding to the zigzag edge structure. (b) Brillouin zones of graphene (black hexagons) and ZGNR (semitransparent rectangle). Dashed lines indicate borders of the one-dimensional BZs of ZGNR along $k_{\parallel}^{ZGNR}$. (c) View of the bulk graphene band structure calculated within the TBA along $k_{\parallel}^{ZGNR}$ direction. The red lines indicate arbitrary cuts, which should result from discretization of the transverse wavevector $k_{\perp}^{ZGNR}$ (one have to remember that in reality they are not exactly straight). (e) Band structure of 6-ZGNR calculated within TBA, *copied from* [117]. It is similar to the projection of the slices of the 3D plot onto the $k_{\parallel}^{ZGNR}$ direction, except for the appearance of the pair of flat metallic bands associated with the zigzag edge states.

While TBA calculations predict a metallic behavior for all ZGNRs, they also show that N-AGNR is metallic if $N = 3p+2$ (where p is positive integer) or otherwise, semiconducting (Figure 3.4 (a, b)). The gap for an N-AGNR (Δ_a) is shown to be inversely proportional to its width, ω_a (Figure 3.4 (a)). In turn, more recent calculations [30, 33, 36, 118], which employ DFT and

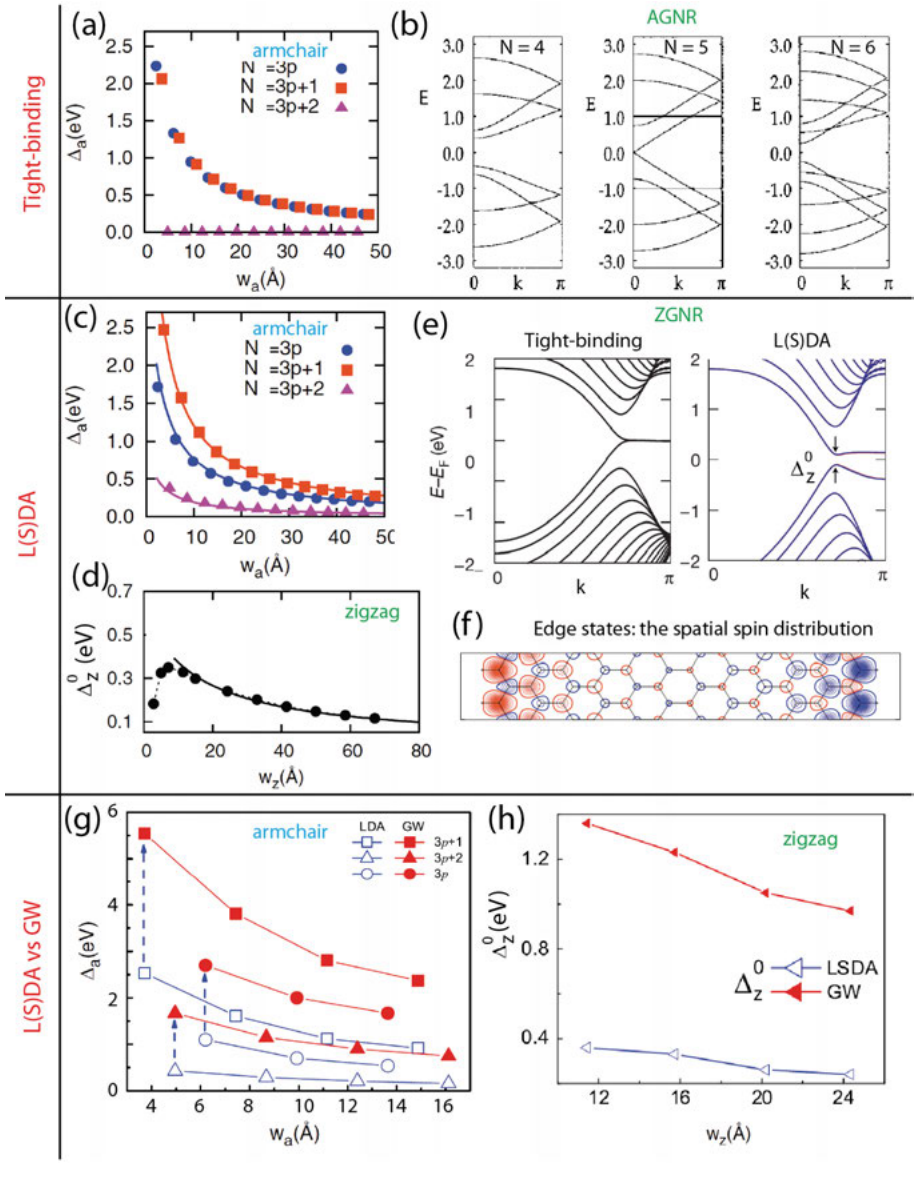

Figure 3.4. (a) The calculated band gap in AGNR (Δ_a) as function of its width (ω_a), (b) the calculated band structure of AGNR with N = 4, 5 and 6. Panels (c)-(f) show results obtained within the local spin density approximation: (c) shows the variation of Δ_a as a function of ω_a, demonstrating the existence of three GNR "families", (d) the variation of Δ_z as a function of ω_z, (e) the band structure of 12-ZGNR within the tight-binding (left) and local spin density (right) approximations, (f) The spatial spin distributions of the ground state for 12-ZGNR. The comparison between energy gaps calculated within L(S)DA and GWA for armchair (g) and zigzag (h) ribbons. (a), (c), (d), (f) - *copied from* [118], (b) - [117], (e) - [30] and (g), (h) *adapted from* [33].

the Local (Spin) Density Approximation (L(S)DA), showed that all zigzag and armchair edged GNRs should have a finite band gap when relaxation of the structure and spin polarization is considered (Figure 3.4 (c-e)). Moreover, independent of the chirality, the band gap Δ is reduced as the width of the system increases (Figure 3.4 (c,d)). In addition, the N-AGNRs can be divided into three "families", which are classified according to whether $N = 3p+1$, $N = 3p+2$, or $3p$ and show a hierarchy of gap size given by $\Delta_a^{3p+1} > \Delta_a^{3p} > \Delta_a^{3p+2}$ [33, 118]. As for ZGNRs, upon inclusion of the spin degrees of freedom within L(S)DA, theory predicts a ferromagnetic ordering at each zigzag edge and antiparallel spin orientation between the electrons in two opposite edge states [30, 118]. The spatial spin distributions of the ground state in the case of 12-ZGNR is displayed in Figure 3.4 (f) [118].

However, it is well established, that LDA (and L(S)DA as its variation) is not the best method to calculate the band gaps of semiconductors and, especially not for nanostructures [119]. To improve the results one needs to include self-energy effects. One successful approach for this is through the GW Approximation (GWA) [119]. In case of GNRs, the use of GWA instead of L(S)DA does not change the overall character of the $\Delta(\omega)$ dependence, but results in significantly larger magnitudes of the band gaps for both armchair (Figure 3.4 (g)) and zigzag (Figure 3.4 (h)) ribbons.

The experimental progress, and, in particular, the use of the bottom-up strategy for GNRs preparation, allowed to prove some of the theoretically predicted properties of these intriguing systems. Thus, by using Scanning Tunneling Spectroscopy method (STS) (see Section 4.4.3), Chen *et al.* [26] have measured the band gap for atomically precise 13-AGNR/Au(111) (Δ_a^{13} = 1.4 eV), which appears to be 1.2 eV smaller than the band gap determined for 7-AGNR/Au(111) (Δ_a^{7} = 2.6 eV). Since both 7- and 13-AGNRs belong to the same "family" ($N = 3p+1$), this result is in line with the theoretically predicted relation between Δ and ω. Moreover, within a range of widths for GNRs of 15 to 90 nm, fabricated using a litography technique, a $\Delta \propto 1/\omega$ relation was also observed [23]. This behavior seems to be independent of the chirality which the authors ascribe to the imperfect edges which are due to the fabrication process employed [23].

The 7-AGNR ($\omega \approx 0.8$ nm), grown on gold surfaces with (111) facets using the bottom-up procedure described in the previous chapter (sections 2.1 and 2.2), is the most well-studied type of GNRs. The band gap value of 7-AGNR has been measured using different techniques, including STS [20, 26, 43], Angle-Resolved Ultraviolet Photoemission Spectroscopy (ARUPS) in combination with Inverse Photoemission Spectroscopy (IPES) [44], Angle-Resolved Two Photon Photoemission (AR-2PPE) [47] and conduction ($\frac{dI}{dV}$) measurements [24]. The accumulated experimental statistics thus allows to perform a reliable comparison with the results from theoretical simulations (Table 3.1). As can be seen, for such narrow ribbons the calculated gap is in the order

of electronvolts: the DFT calculations predict a band gap from 1.5 to 2 eV [30, 32, 118] while the value obtained in GWA as expected yields a larger band gap of 3.8 eV [33, 43]. The experimentally observed Δ_a^7 for 7-AGNRs/Au is 2.5 - 2.8 eV, and thus significantly smaller than 3.8 eV expected for isolated 7-AGNR within GWA. The reduction of the band gap can be associated with the effect of the polarization of the gold substrate which is estimated by including image charge (IC) corrections in the GW approximation [43]. The resulting Δ_a^7 value of 2.3-2.7 eV is in relatively good agreement with experimental studies.

It should be noted, that the effect of ribbon-substrate interaction cannot always be limited to polarization effects. Indeed, for inert Au(111) this simplification is justified by the small hybridization of the electronic bands of ribbons and Au(111) and the absence of significant ribbon-substrate charge transfer [43]. Nevertheless, as was demonstrated by Huang *et al.* [45], STS indicates that the electronic structure of 7-AGNR is influenced when it is grown on Ag(111), indicating a weak chemisorption nature of the ribbon-substrate interaction. Recent DFT calculations carried out for ZGNRs on Au(111), Ag(111) and Cu(111) [39] also pointed out the presence of significant interaction and charge transfer between the GNRs and the substrate for Ag(111) and to an even larger extent for Cu(111). Such a significant substrate effect can be perceived in two ways: on the one hand, this is certainly a disadvantage if one is interested in the preparation of GNRs with unperturbed electronic structure, while on the other hand the ribbon-substrate interaction can be considered as another way to manipulate the electronic and magnetic properties

Table 3.1. *Comparison of the band gap values for 7-AGNR, determined by various theoretical and experimental methods. (PBE: Perdew-Burke-Enzerhof realization of the general gradient approximation. HSE: Hybrid density functional. GW + IC: GWA with image charge correction to take into account interaction with the Au(111) surface.)*

Method	Environment	Δ_a^7 (eV)	Ref.
DFT (PBE)	in vacuum	1.5	[32]
DFT (HSE)	in vacuum	2.1	[32]
DFT (LDA)	in vacuum	1.6	[30, 118]
GWA	in vacuum	3.8	[33]
GWA + IC	Au(111)	2.3-2.7	[43]
ARUPS/IPES	Au(788)	2.8	[44]
ARUPS/STS	Au(788)/Au(111)	2.3	[43]
STS	Au(111)	2.5	[26]
AR-2PPE	Au(111)	2.6	[47]
Conductance	Au(111)	2.7	[24]

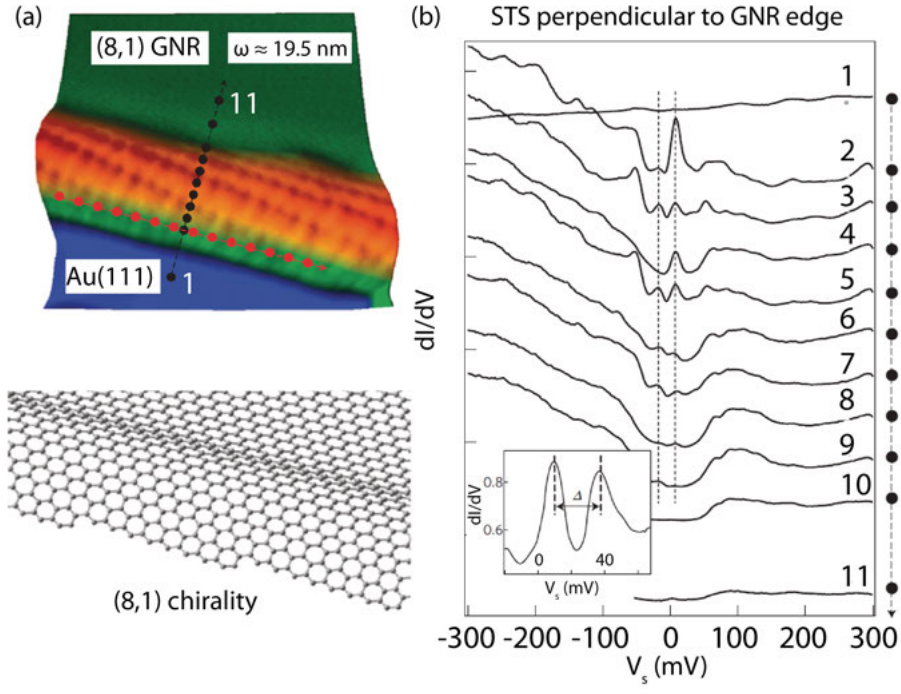

Figure 3.5. Experimental observation of the edge states associated with zigzag edges. (a) Top - atomically resolved STM image of the terminal edge of an (8,1) GNR with measured width of 19.5 nm. Bottom - structural model of the (8,1) GNR edge. (b) Normalized dI/dV STS curves measured at locations represented by black dots at the STM image in (a). Inset shows a higher resolution dI/dV spectrum for the edge of a (5,2) GNR with 15.6 nm width. *Copied from* [120]

.

of GNRs [39, 121]. Very recently, the authors of Ref.[70] have shown that for poly(para-phenylene) (PPP) chains (which can be considered as narrow 3-AGNRs) grown on Cu(110) substrate, interaction with the substrate significantly affects the electronic structure of the ribbons by reducing their bandgap and by filling the lowest unoccupied states. Interestingly, the electronic structure of 3-AGNR differs considerably on Cu(110) [70] and Cu(111) [71] substrates.

The edge states described above, which are characteristic for zigzag edges have also been observed experimentally. As an example Figure 3.5 illustrates the observation of such states, located at the zigzag edges of chiral (8,1) GNR, prepared *via* chemical unzipping of carbon nanotubes and further deposited on a Au(111) substrate [120]. Figure 3.5 (a) shows the topographic STM image and the corresponding model of the (8,1) GNR edge. As can be seen, the zigzag character is rather pronounced for this type of ribbons and there-

fore their electronic structure is quite close to the ZGNRs having the same width (19.5 nm). Spatially resolved STS clearly reveals the existence of two electronic states close to the Fermi level, which are observed only close to the chiral GNR edge (Figure 3.5 (b)). The edge states are separated by a small gap of 24 mV for (8,1) GNRs and 28 mV for the narrower (5,2) GNRs in agreement with the calculated results (Figure 3.4 (d,e)). It should be noted, that similar states have also been observed on the zigzag edges of finite AGNRs and are always referred to as the *end states* [26].

3.2 On-surface synthesis of graphene nanoribbons

As was mentioned above, the bottom-up strategy, originally implemented by Cai *et al.* [42] to produce 7-AGNRs on Au(111) surface, has been proven to be a powerful tool for the preparation of GNRs with atomic precision. Each stage of the process, leading to the formation of GNRs from molecular precursor molecules, has been described in detail in Chapter 2 (Sections 2.1 and 2.2) and can vary depending on the substrate used. Not counting the only work where 7-AGNRs have been grown on Ag(111) [45], all other experiments have been carried out on Au(111) [20, 21, 25–27, 42, 46, 47] or on its vicinal Au(788) surface [43, 44]. Let us quickly repeat the main stages of the process. If the molecule containing Br side groups is deposited on Au(111) at RT annealing to 200°C is required to activate the dehalogenation process which, in turn, is accompanied by the directional covalent coupling of debrominated units. The polymer chains formed play a role of large precursors for the formation of GNRs *via* the internal cyclodehydrogenation process, which on Au(111) takes place at 400°C.

Without significant changes, the described two-step reaction scheme can be applied to all kinds of GNRs, which have been synthesized on gold (111) facets from various brominated molecular precursors. Figure 3.6 summarizes the achievements to date in the bottom-up synthesis of various GNRs on gold surfaces. Apart from DBBA molecules (Type I precursor) , resulting in 7-AGNRs, using a slightly modified building block (Type II) Chen *et al.* [26] were able to obtain straight 13-AGNRs and to perform STS studies on them. Furthermore, by combining Type I and Type II precursors the same authors have grown 7-13 graphene nanoribbon heterojunctions [21].

Besides the AGNR system, the chevron-type GNRs (CGNRs) can be produced from the appropriate precursor molecule (Type III) [20, 42]. In principle CNGR can be seen as composed of two alternating armchair-edge sub-ribbons, characterized by $N = 9$ and $N = 6$. Such a special shape has an effect on the electronic band structure of CGNRs in general [44] and, in particular, on its thermoelectric properties [122]. Very recently even ZGNRs were realized by a proper selection of the initial molecular entity [123].

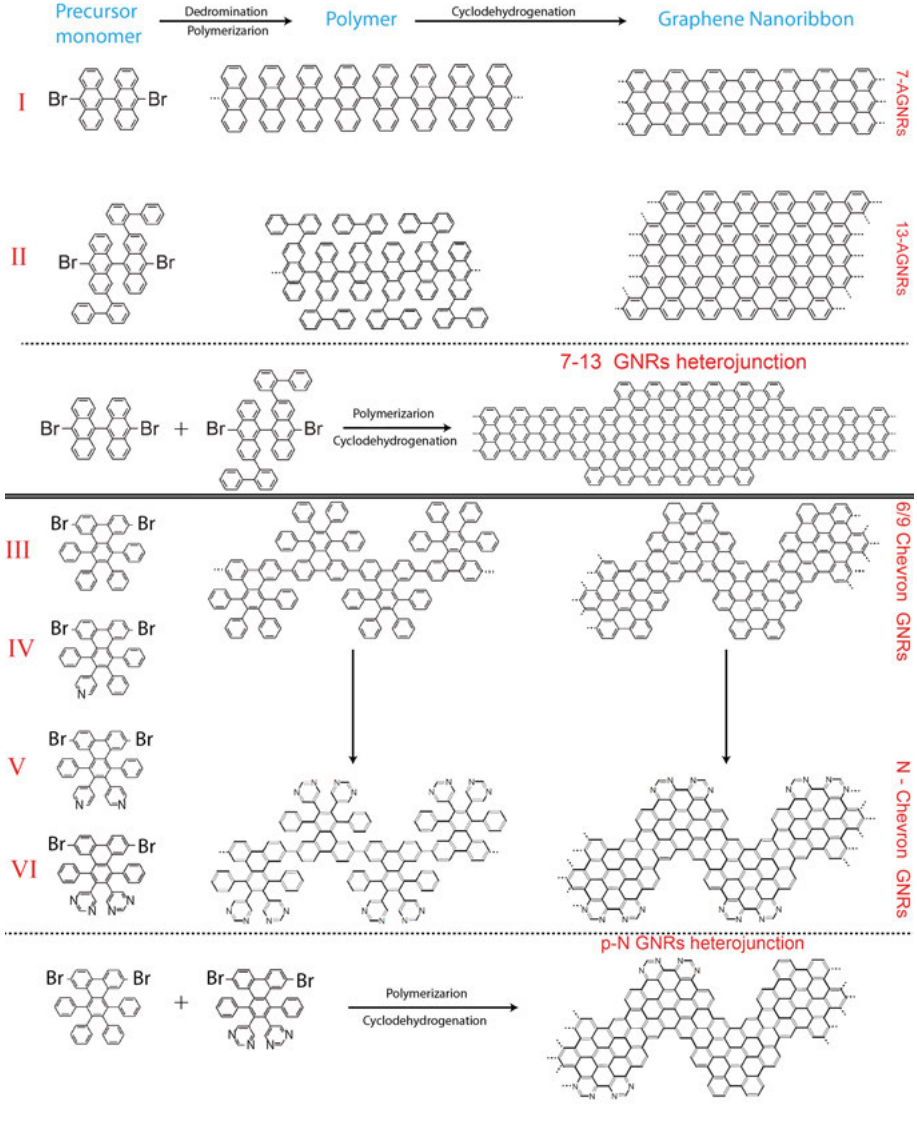

Figure 3.6. Different types of GNRs grown *via* a bottom-up procedure from corresponding molecular precursors. See text for the explanation.

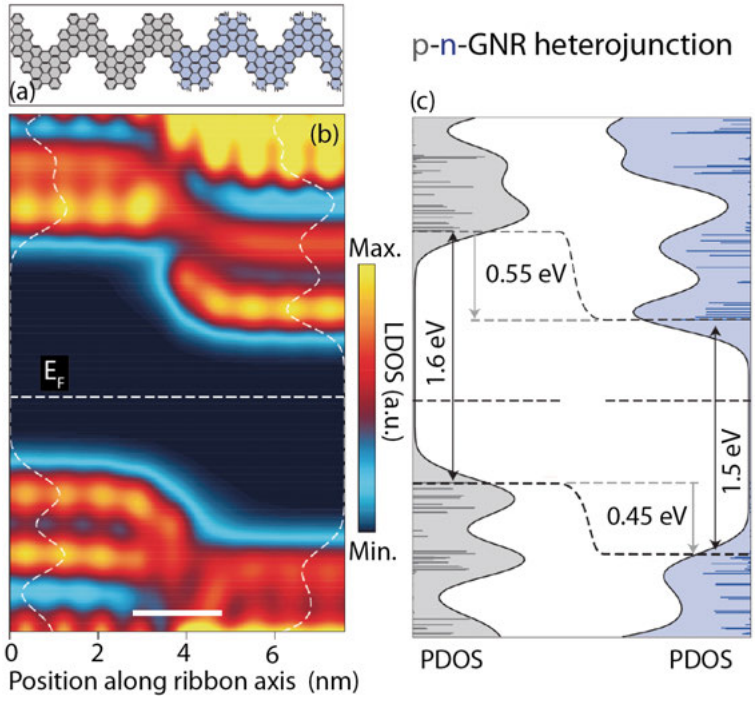

Figure 3.7. The p-n heterojunction *via* bottom-up. (a) The schematic model of p(gray)-n(blue) heterojunction and the averaged local DOS measured across it (b). The scale bar (2 nm) for (a) and (b) is the same. (c) The results of DFT simulation for p-n-GNR junction. PDOS - computed density of states, projected on the undoped and electron-doped GNR segments. *Copied from* [20].

Apart from changing the geometry of the produced GNRs, one can think about functionalization of precursor molecules and hence the resulting GNRs as another possibility to tune the electronic properties of ribbon-based devices [20, 27, 37, 41, 80, 81]. For example, by analogy with graphene [124, 125], doping of GNRs can be achieved by inclusion of substitutional heteroatoms in the carbon lattice. Thus, precursor molecules with one (Type IV), two (Type V) and four (Type VI) nitrogen-substituted sites have recently been used for the synthesis of n-doped CGNRs on Au(111) [20, 27]. A definite plus of the implemented bottom-up method lies in the precise control over the doping level which is fully determined by the number of nitrogen-substituted carbon atoms in the precursor building block. Bronner *et al.* [27] have shown that increasing the number of N atoms in the precursor molecule for N-CGNRs (here N stands for the nitrogen) yields a band shift of 0.13 eV per nitrogen atom. Interestingly, in their recent work Cai *et al.* [20] have synthesized graphene nanoribbon heterojunctions by combining Type III and Type VI precursors.

The resulting N-CGNRs are thus composed of undoped and electron-doped segments.

The electronic structure of the obtained atomically precise p-n-GNR junction has been further studied using STM (STS) local probe methods in combination with DFT calculations. By applying STS to measure the local DOS across the p-n junction (Figure 3.7 (a)), the authors were able to visualize the band shift in this region (Figure 3.7 (b)). The experimental data are in full agreement with the theoretical predictions (Figure 3.7 (c)) and show that the band bending across the p-n-GNR heterojunction occurs within only 2 nm and can be characterized by the band offset of about 0.5 eV. Therefore, taking into account the wide tunability of the band gap *via* the ribbon width and *via* the doping level achieved by changing the number/type of substituting atoms in precursor molecules, the unique potential of bottom-up on-surface synthesis for the engineering of atomically precise GNR heterostructures was clearly demonstrated.

4. Experimental section

This chapter deals with a description of various methods used in the present work to enable detailed investigations of on-surface molecular transformations and the resulting nanostructures.

The investigation of surfaces and, in particular, chemical processes which take place there is a challenging task, requiring special experimental conditions and techniques. Nevertheless, the undoubted value of the ability for nano-scale control and functionalization on surfaces for both theoretical and practical applications makes this topic the subject of enduring interest for the surface science community. Typically, in order to study the characteristics of the on-surface reactions one must have an opportunity to control the surface characteristics on the atomic scale. Thus, in order to prevent residual gas adsorption, which can have large effect on the surface properties, such experiments require Ultra High Vacuum (UHV) conditions. In the present work, all the results were obtained in an UHV of better than 5×10^{-10} mbar.

A lot of surface science techniques rely on the detection of electrons emitted from the sample. The reasons for electrons being such a prominent probe are many: they are easy to generate, handle and detect. But even more important is the fact that low energy electrons with a kinetic energy of 20 - 200 eV are extremely surface sensitive since they can travel only very short distances through the sample without undergoing inelastic scattering events - typically less than 10Å.

In this work mainly three techniques, all of which, to some extent, are based on the detection of electrons, were used: Photoelectron Spectroscopy (PES), Near-Edge X-ray Absorption Fine Structure (NEXAFS) spectroscopy in the partial electron yield (PEY) mode and Scanning Tunneling Microscopy (STM). In the following chapter the physical basis and practical realization of each method will be discussed in more detail.

The properties of single crystal metal surfaces as well as some aspects of the sample preparation procedures which have been employed are also discussed.

4.1 Photoelectron spectroscopy (PES)

Photoelectron spectroscopy (PES) is a widely used surface science technique for the investigation of the electronic structure of matter. It relies on the photoelectric effect occurring as the result of light-matter interaction. In the most simple picture, the photons that hit the sample kick out electrons that are then

detected. First observed in 1887 by Hertz [126], the photoelectric effect was theoretically explained in 1905 by Einstein [127], who invoked the quantum nature of light to show that a photon can liberate an electron from a system only if its energy is larger than the work function of the material. Most often, different achronyms are used for the technique, depending on the employed photon energy regime. In general, PES can be divided into two types:

- Ultraviolet Photoelectron Spectroscopy (UPS) utilizing photons with an energy from 10 eV to 100 eV. UPS is typically implemented to investigate the occupied states in the valence and conduction bands of solids.
- X-ray Photoelectron Spectroscopy (XPS) which, as follows from its name, employs photon energies of about 100 - 10000 eV. XPS is widely used to obtain information about the core levels of elements and is often referred to as Core-Level Photoelectron Spectroscopy or CLPES.

In this work we have utilized XPS in the *soft* X-ray regime ($\hbar\omega \approx 150$ - 2000 eV) allowing us to follow the transformations of core levels line shapes and binding energies of such elements like carbon, nitrogen, oxygen, bromine *etc.*, which are often present in various organic molecules used in molecular architecture.

It should be noted that such division into groups is rather arbitrary both in terms of the object of investigation and the physical processes behind. Thus in the following section the common theoretical aspects of PES will be considered.

4.1.1 Theoretical aspects of PES

The photoemission process is generally described by the Einstein equation, which can be written as:

$$E_K = \hbar\omega - E_B - \phi, \tag{4.1}$$

where E_K is the Kinetic Energy (KE) of the photoelectron, ϕ stands for the material's work function and E_B - is the Binding Energy (BE) of the electron. The BE of an energy level measured by PES in solids is generally referred to the Fermi level (E_F), and to the vacuum level in free molecules or atoms.[1] Equation 4.1 can be interpreted as follows: a photon with energy $\hbar\omega$ can liberate an electron from the solid only if $\hbar\omega \geq E_B + \phi$. The photon energy thus determines the kinetic energy of the outgoing electron. The BE is defined as the difference in total energies of the N - and (N - 1) - electron systems:

$$E_B = E_{tot}(N-1) - E_{tot}(N), \tag{4.2}$$

[1] One has to keep in mind that most researches give E_B with a positive sign. Therefore E_B should not be confused with the initial-state energy, E_i, which has the same reference point but the opposite sign and corresponds to the negative energy of the certain energy level (orbital) occupied by an electron in the matter.

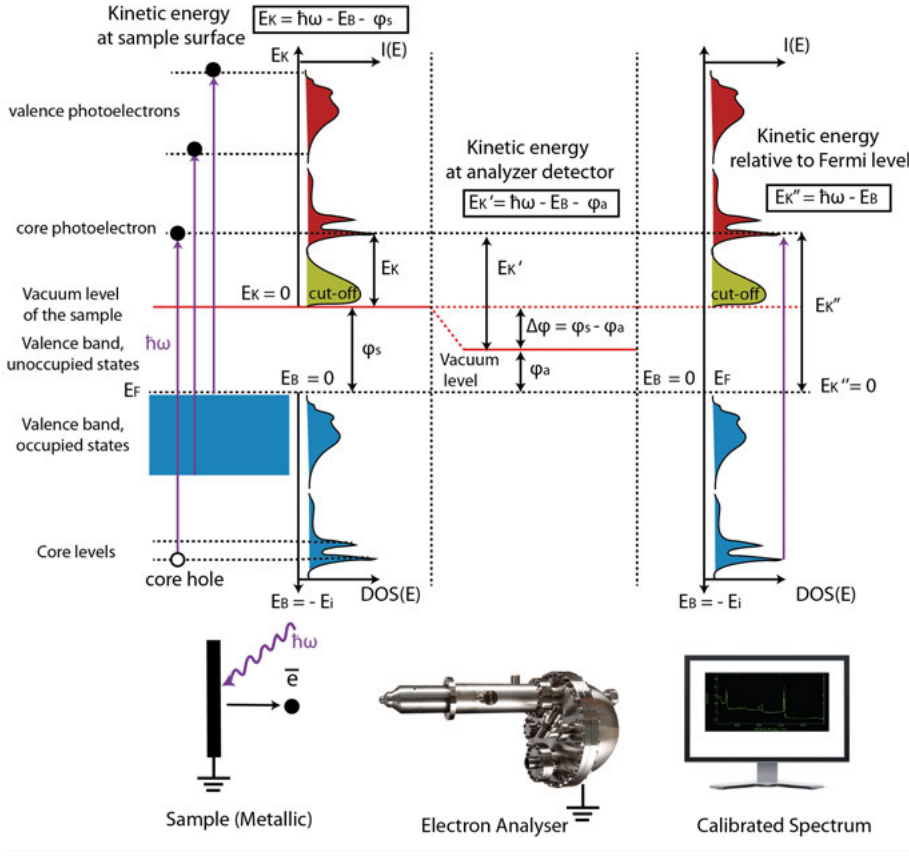

Figure 4.1. Schematic of the photoemission process. From left to right: directly at the sample surface; at the analyzer detector; after calibration to the Fermi level position. The sample is in electrical contact with the spectrometer, which results in the alignment of the Fermi levels, while the vacuum levels of the electron analyzer and the sample do not coincide. The relation between the photoemission intensity from the solid (I(E)) and the density of the occupied states (DOS) is shown.

where $E_{tot}(N-1)$ includes also the Coloumb interaction between the core hole and the outgoing electron.

A schematic view of the origin of the photoemission spectrum is shown in Figure 4.1. For simplicity the case of a metallic sample is shown. Equation 4.1 is directly illustrated by this scheme. As can be seen, in the simplest approach the kinetic energy distribution of the photoelectrons (I(E)) generally represents the occupied density of states (DOS) distribution in the sample plus the signal from slow (secondary) electrons, which starts as a sharp cut-off at the vacuum level and rapidly drops down with increasing kinetic energy. Of course in reality the photoemission is a complicated many-body physical phenomenon, which triggers a long sequence of accompanying processes affecting the final intensity, spectral shape and energy positions of the individual features in the spectrum. In particular, when analyzing an XPS spectrum one should take into account the photoionization cross-section, the presence of satellite lines, Auger peaks, plasmon losses *etc.* Some of these factors will be shortly outlined in the following sections. For a detailed description of the photoemission theory and applications the classical book of Hüfner [128] may be recommended.

Moreover, a purely experimental aspect of binding energy evaluation has to be taken into account. As can be seen from the left panel of Figure 4.1, E_K of the emitted electron, which is determined by Equation 4.1, should be measured with respect to the vacuum level of the sample. Nevertheless, the experimentally measured kinetic energy (E'_K) is determined relative to the vacuum level of the electron analyzer. The Fermi levels of the sample and the spectrometer are aligned since these are connected electrically, but the vacuum levels are not. The reason is that spectrometer has its own specific (generally unknown) work function (ϕ_a), which does not coincide with the sample work function (ϕ_s). Therefore, a contact potential exists between the sample and the analyzer thus leading to acceleration or deceleration of the photoelectrons by $\Delta\phi = \phi_s - \phi_a$. Nevertheless, simple calibration procedures allow to overcome this problem. Indeed, during measurements the sample-analyzer system has a common Fermi level, which can serve an ideal reference point in the case of metallic and low band gap semiconductor samples. By measuring the position of the Fermi level with the same photon energy as for the core-level and moving the BE axis origin in such a way, that $E_B(E_F) \equiv 0$, one can determine the $E''_K = \hbar\omega - E_B$ independent from the spectrometer work function.

Photoemission cross section

From a quantum mechanical point of view in photoemission we are concerned with transitions from (occupied) initial states to free states of the system with Hamiltonian H_0. The transitions are induced by the incoming radiation, *i.e.* by the time-dependent electromagnetic field. The situation can be treated by standard means of time-dependent perturbation theory with the perturbation operator H^{int}. Since the perturbation is periodic in time, Fermi's Golden Rule

can be employed to calculate the transition rate between the initial multielectron state, described by the wavefunction Ψ_i and the final state Ψ_f. Thus the expression for the integral cross section for photoemission can be written as follows:

$$\sigma_{fi} \propto \left|\langle \Psi_f | H^{int} | \Psi_i \rangle\right|^2 \delta(E_f - E_i - h\nu) \tag{4.3}$$

E_i - energy of the system in the initial state
E_f - final state energy

For the system irradiated by light, H^{int} can be written down by replacing the momentum operator p by $\mathbf{p} - e\mathbf{A}$, where $\mathbf{A}$ is the vector potential of the external field. In the simplest case of a spinless particle H^{int} can be represented as:

$$H^{int} = \frac{e}{mc}\mathbf{A} \cdot \mathbf{p} \tag{4.4}$$

If $\mathbf{A}$ is then decomposed using the plane monochromatic waves as a basis, it can be shown that:

$$\langle \Psi_f | H^{int} | \Psi_i \rangle \sim \langle \Psi_f, |\mathbf{up} e^{i\mathbf{k}'\mathbf{r}} | \Psi_i \rangle \tag{4.5}$$

$\mathbf{u}$ - polarization vector of incident radiation
$\mathbf{k}'$ - wave vector of incident radiation

By applying the electric dipole approximation in which the wavelength of the electromagnetic radiation is assumed to be much larger than the typical size of the exited atom we get $e^{i\mathbf{k}'\mathbf{r}} \to 1$. Therefore the matrix element in 4.5 can be rewritten and the cross section appears to be proportional to $\langle \Psi_f | \mathbf{up} | \Psi_i \rangle$ or $\langle \Psi_f | \mathbf{ur} | \Psi_i \rangle$ in coordinate representation [128]. If we assume that the potential is spherically symmetric for both the initial and final states of the system then this matrix element can be decomposed into radial and angular parts. Taking into account the properties of the spherical functions, it can be shown that the transition, described by Equation 4.3, is governed by the *selection rules* for the quantum numbers: $\Delta S = 0$, $\Delta l = \pm 1$.

Equation 4.3 can be further adjusted for practical applications by introducing one more approximation. Indeed, if the factorization of the multielectron wave functions for both initial and final states is allowed, they may be represented as $\Psi(N) = C\varphi_v \psi_R^v(N-1)$. Here the index v indicates that the electron with quantum number v has been left out (because it was photoexcited), R stands for the remaining system, N denotes the number of electrons in the illuminated volume, φ_v is a one-electron wave function while $\psi_R^v(N-1)$ is a wave function of the rest of the system and C is an antisymmetrizing operator. By applying this approach together with the dipole approximation, Equation 4.3 can be rewritten as:

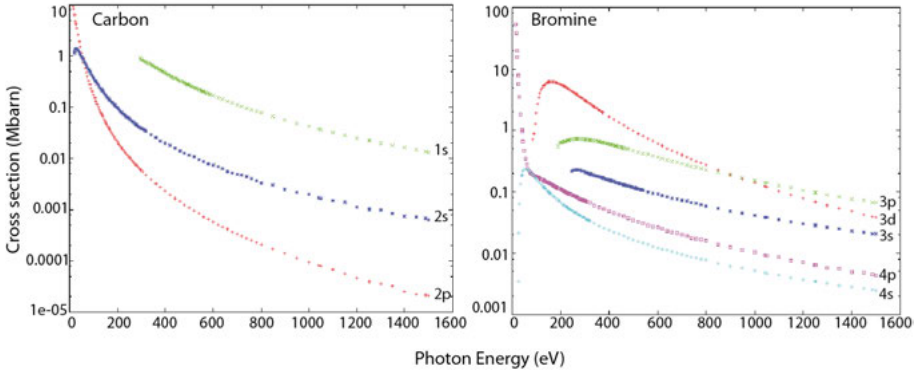

Figure 4.2. Calculated photoemission cross sections as a function of the photon energy for carbon and bromine. *Adapted from* [129].

$$\sigma_{fi} \propto |\langle \varphi_{f,v} | \mathbf{ur} | \varphi_{i,v} \rangle|^2 \cdot |\langle \psi^v_{R,f}(N-1) | \psi^v_{R,i}(N-1) \rangle|^2 \cdot \delta(E_f - E_i - h\nu) \quad (4.6)$$

Therefore, it can be seen that the matrix element of the photoionization process consists of a one-electron term and an overlap integral of the rest electron system. Assuming that the rest of the system is not affected by the excitation of the photoelectron (*frozen-orbital approximation*), so that $\psi^v_{R,f}(N-1) = \psi^v_{R,i}(N-1)$, the photoemission cross section can be represented by one-electron matrix elements and Equation 4.6 can be rewritten in the following one-electron form with explicit treatment of the **k** dependence of the electron:

$$\sigma_{fi} \propto |\langle \varphi_f, \mathbf{K} | \mathbf{ur} | \varphi_i, \mathbf{k} \rangle|^2 \delta(E_f - E_i - h\nu) \delta(\mathbf{K} - \mathbf{k} - \mathbf{G}) \quad (4.7)$$

where **k** and **K** are the wave vectors of the electron before and after interaction, respectively. The vector **G** is the smallest reciprocal lattice vector. The additional delta function in 4.7 represents nothing more than a momentum conservation law.[2] When choosing the photon energy for the experiment one should take into account that the chosen photon energy will generate a high cross section in order to produce high intensity of the recorded spectrum. Indeed, Equation 4.7 includes the matrix element, the value of which directly depends on the overlap between the localized atomic wave function of the initial state and delocalized wave function of the outgoing wave. Taking this into account it is possible to give a qualitative description of the energy dependence for the core-level cross section [130]. At the photoemission threshold the energy of the outgoing electron is low and the corresponding de Brogile wavelength is long. Therefore we can assume that in this case the amplitude of φ_f is roughly constant in the vicinity of the atom and the overlap integral will give some finite value. On the other hand, if the photon energy is high, the final

[2]Momentum of the photon is not included, which corresponds to vertical (optical) transitions.

state wavelength is very short and oscillates rapidly (changes sign) in the region of initial state, which gives an overlap integral approaching zero. Figure 4.2 illustrates the calculated atomic cross sections for Carbon and Bromine. Tabulated values of the photoionization cross sections for different elements can, for example, be found in Ref.[129].

Inelastic mean free path: Surface sensitivity

In the framework of the so-called three step model[3] [131], the photoelectron produced as a result of the photoionization process, travels through the volume of the sample to the surface where (if it has enough momentum $\mathbf{K}\perp$ perpendicular to the surface of the solid for overcoming the surface potential barrier) it can escape to the vacuum.

As was mentioned above, one of the main motivations to use electrons in surface science is their short inelastic mean free path (IMFP) in the matter. In general, the IMFP (λ) is the average distance which electron travels in the solid before it experiences the first event of inelastic scattering. The primary electrons lose their energy in the solid *via* a number of processes (like plasmon excitation, electron-hole pair formation, phonon excitation, *etc.*) which, in turn, changes the energy (and momentum) distribution of the photoelectrons on their way to the surface. Thus, the intensity of electrons maintaining the original kinetic energy, E_i, decays according to:

$$I(d) = I_0 e^{\frac{-d}{cos(\theta)\lambda}}, \tag{4.8}$$

where $I(d)$ is the intensity of primary electrons with unchanged energy originating from the depth d, I_0 is the initial beam intensity and θ is the angle between the surface normal and the wavevector of the ejected electrons. Obviously, IMFP is a function of the electron energy ($\lambda = \lambda(E_i)$). Figure 4.3 shows the so-called *universal mean free path curve* which demonstrates that IMFP is, to a large extent, a material-independent function of kinetic energy. The reasoning behind this is that in the energy range of interest the electrons in the solid can be considered as a free electron gas and thus the IMFP can be described by the mean electron density, with is approximately the same for all materials [128]. The mean free path curve has a broad minimum around a kinetic energy of about 70 eV. There it is less than 10Å. This means that if we observe an electron with this kinetic energy and this electron has left the solid without suffering an inelastic scattering event, it originates from the first few atomic layers. Moreover, we can decrease the surface sensitivity either by going to very low energies of a few eV or to much higher energies of several

[3]The three step model divides the photoemission process into three steps: (i) excitation of photoelectron, (ii) travel to the surface and (iii) escape of photoelectron into vacuum.

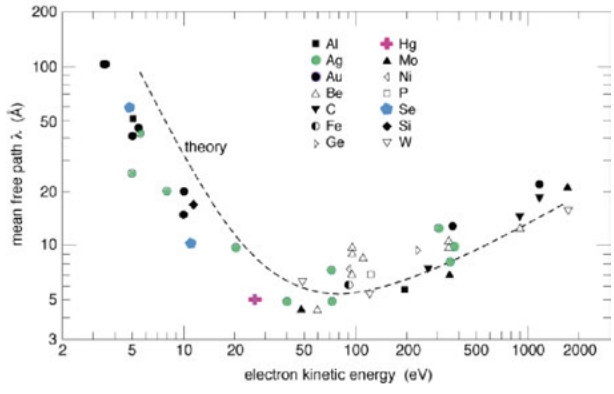

Figure 4.3. Electron mean free path curve. Theoretical curve is shown with the dashed line, while experimentally obtained values for different elements are shown with symbols. *Copied from* [132].

keV[4]. For the photon energy range used in soft XPS (150 - 2000 eV) the IMFP is only a few Å, which makes XPS a very surface sensitive technique.

The IMFP conception does not have consequences only for XPS. In principle, as was mentioned before, it works for all electron-based techniques in which low-energy electrons are detected. For example, as will be demonstrated in sec. 4.2 it can be applied for the estimation of the probing depth of Near-Edge X-ray Absorption Spectroscopy technique, measured in the Partial Electron Yield mode. Moreover, the IMFP does not have only consequences for the surface sensitivity of electron based techniques, but also poses a problem as electrons are required to travel relatively long distances (several dm) from the sample to the detector and would strongly interact with any gas present. Therefore, this is one more reason to perform electron-based experiments under UHV conditions, thus preventing inelastic scattering of the electrons against the residual gas molecules.

4.1.2 Core-level PES

XPS is often also referred to as Core-Level Photoemission Spectroscopy (CLPES). This title emphasizes the main purpose of this technique which is to obtain information about non-dispersive core levels of the elements: their energy positions and line shapes, shape and chemical shifts. In particular, the concept of core-level *chemical shifts* is the basis of a technique called ESCA, namely Electron Spectroscopy for Chemical Analysis, which was significantly developed in the late 1950s and early 1960s by the group of Kai Siegbahn

[4]Of course, when choosing the corresponding photon energy, the energy dependence of the photoionization cross section have to be taken into account.

from Uppsala University, Sweden [133]. Owing to the rapid improvement of vacuum technology and the wide availability of extremely bright synchrotron radiation sources, CLPES and ESCA as its most common variation are currently among of the most demanded techniques, which are extensively used in surface science.

In this work CLPES was employed as an analytical tool allowing to follow the changes in concentration and chemical state of elements contained in the sample. Thus, some useful aspects of CLPES and ESCA, required for the understanding of the experimental results presented in the thesis, are described below.

Binding Energy definition

Before we start to discuss the core-level binding energy shifts, we need to define the BE conception in more details. In chapter 4.1.1 of this work the *frozen orbital approximation* to the photoexcitation was introduced. In the framework of this approximation it is assumed that the removal of a photoelectron from a certain orbital v does not affect the remaining electrons and thus in Equation 4.6 the following equality holds: $\psi^{v}_{R,f}(N-1) = \psi^{v}_{R,i}(N-1)$. In this case the BE of the orbital by definition equals the energy of Hartree-Fock orbital (ε_v), taken with the opposite sign (so-called Koopman's theorem [134]):

$$E_B(v) = -\varepsilon_v \tag{4.9}$$

However, in reality, as soon as the core hole is created, the remaining electron system readjust itself in order to minimize the system's total energy. Therefore, the so-called *final state effects* have to be taken into account for a more accurate estimation of the binding energy. Usually, binding energy can be represented as:

$$E_B(v) = -\varepsilon_v + \varepsilon_{relax} + \varepsilon_{corr}, \tag{4.10}$$

where ε_{relax} is a term describing the *relaxation* correction due to the screening of the core hole by the rest of the electrons, and ε_{corr} is a *correlation* term which includes collective effects of electron-electron interaction which can be neglected in many cases. Inclusion of the relaxation and correction terms lowers the core-level BE and provides a better agreement with experimental data.

As can be seen, the photoexcitation process seriously affects the whole electronic system of the sample. Therefore, the photoemission spectrum can consist of several lines: the main line accompanied by energy-loss structures at higher BE, which originate either from the effect of the static core hole created during the photoexcitation of the core electron, or by the excitations that take place during transport of the photoelectron out of the solid. The corresponding energy-loss processes are usually called "extrinsic" or "intrinsic" excita-

tions. For example, plasmon peaks characteristic for some metals and which are due to the excitation of the conduction electron density oscillations, can be both "extrinsic" and "intrinsic". The example of pure "intrinsic" energy-loss features are the shake-up/shake-off satellites, which involve excitations of valence band electrons by the core-hole potential to the unoccupied state above the Fermi level or to the continuum, respectively. For the interpretation of "intrinsic" features a simple one-electron approach, allowing multiple excited states having the same core hole, can be used (calculated wihin the *sudden approximation*[128, 135]). The further description of satellite structures is omitted here since such structures are poorly expressed in the spectra of the molecules presented in this thesis. For further reading the interested reader is referred to *e.g.* references [128, 135, 136].

Core-level chemical shift

As was mentioned before, the so-called chemical shifts of the core-level binding energy play a central role in the ESCA technique. Indeed, usually one is primarily interested in understanding and using chemical shifts of binding energies rather than their absolute values. The *Chemical Shift* (CS) can be defined as a change of the binding energy of a particular energy level of the same atom in different chemical surroundings, usually denoted as ΔE_B. Therefore CS can be employed to distinguish and identify the chemical and/or geometrical environment of the emitting atom.

Using a very simplified model we can discuss how the chemical shift arises. The contributions to ΔE_B may be divided into *initial-state* and *final-state ones*. The initial state effect on the BE can be roughly split into the contribution from the atom's nearest neighbors and from the rest of the crystal:

$$\Delta E_B^{ini} = \frac{\Delta q}{\overline{r_v}} + \frac{\Delta q \alpha_M}{d} \tag{4.11}$$

The first term correspond to the Coulomb interaction between the core electron and the difference in valence electron charge Δq due to the charge transfer from/to the nearest neighbors. Here $\overline{r_v}$ is the average radius of the valence orbitals. The second term represents the variation of the electrostatic interaction between the core shell and the rest of the crystal, *i.e.*, a variation of Madelung energy (α_M stands for the Madelung constant and d is the lattice constant).

The final-state effects represent the changes in the second term of Equation 4.10, and thus deal with the difference in relaxation (screening) of the core hole upon charge transfer Δq. Without going into details, the relaxation contribution to the CS can be explained as follows: an increase in the number of valence electrons, which can screen the photohole from the outgoing electron, leads to a reduction of the corresponding Coulomb attraction. This, in turn, leads to an enhanced kinetic energy of the photoelectron and hence to a decrease in BE. For a detailed analysis of chemical shifts it is important to explicitly include the final state effects. However, for many types of systems,

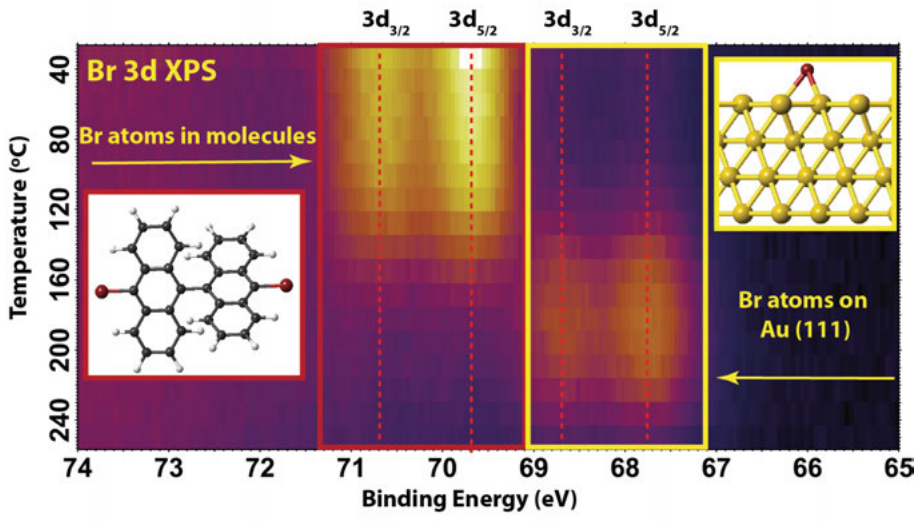

Figure 4.4. Photoelectron intensity map, showing evolution of Br 3d XPS spectrum of DBBA/Au(111) as a function of increasing temperature (from Paper I). The photoemission line demonstrates a prominent (almost 2 eV) chemical shift towards lower binding energies when Br atoms split off from molecules. Inset to the left shows a ball-and-stick model of DBBA molecule. Inset to the right shows the schematics of bromine adatom on Au(111) surface. Carbon atoms are gray, hydrogen atoms are white, gold atoms are yellow and bromine atoms are dark red.

like the molecular nanoarchitectures described in the present thesis one still finds a good correlation between shifts and charge transfer, even when final state effects are included.

It should be noted that in metallic systems, *e.g.* in alloys, the screening of the core-ionized state is very efficient. As a result the final state effects can play a dominant role in the determination of the sign for the CS. In general, for such systems there is no direct correlation between the charge transfer Δq and the CS [137, 138].

Because of the extremely high surface sensitivity of XPS, one can even investigate the energy levels of submonolayers of molecules or atoms adsorbed on a surface. The chemical bonding to the surface will, of course, be reflected mainly in the valence orbitals, but the CLPES can also give some useful information. This property of photoemission spectroscopy is extensively used in the present thesis. Thus, Figure 4.4 is an example from **Paper I**, demonstrating the usage of chemical shift for tracking the sample evolution upon heating. It this case the sample was a submonolayer of DBBA molecules on a Au(111) surface. Figure 4.4 shows the Br 3d photoelectron intensity map (a set of color-scaled XPS spectra combined together), recorded during the sample annealing. Below 100°C the Br 3d signal is a single spin-orbit doublet (J

= 3/2, J = 5/2). Further heating leads to the appearance of a new spin-orbit doublet at lower binding energies. The high BE component is attributed to Br atoms linked to the DBBA molecule, while the low BE one can be assigned to Br atoms adsorbed on Au(111) after debromination of the molecules. The CS is almost 2 eV in this case and thus allows one to clearly distinguish the two different components. This is not always the case, since the CS can in principle be infinitely small, while the resolution of the experimental equipment is always limited. Thus in many cases the CS are unresolvable and the individual components, corresponding to chemically nonequivalent chemical states of the atom, merge into one broad line having a complicated spectral profile. Since most CLPES experiments are aimed at the precise determination of the binding energies and the relative intensities of the peaks, originated from the same atom in different chemical states, a *decomposition* (or *line fitting*) of the photoemission spectrum is often needed. But before describing the fitting procedure, the factors which affect the core-level line shape should be discussed.

Line shape decomposition

There are various factors that contribute to the shape of the core-level peak, including lifetime, different types of inelastic losses, instrumental resolution, *etc.* Let us consider the most important ones.

The excited final state of the photoemission process can de-excite through several possible channels, including radiative (fluorescence) and/or non-radiative (Auger) decay. The finite lifetime, in turn, results in a spectral broadening having a Lorentzian shape [139].

Moreover, the primary core-level XPS line will be additionally modified by different excitation processes which, as was mentioned above, lead to energy losses and which always accompany the photoemission. Altogether this results in broad features and higher background on the high BE side of the main peak. In particular, on metals a significant line asymmetry towards higher binding energies can usually be observed due to the fast response of the Fermi sea of conduction electrons to the photohole. Such assymetric spectral profile has been first described by Doniach and Ŝunjić [140] in the form:

$$f(E) = \frac{\Gamma(1-\alpha)}{(\gamma^2 + (E-E_0)^2)^{(1-\alpha)/2}} \cos(\frac{\pi\alpha}{2} + \theta(E)), \tag{4.12}$$

where

$$\theta(E) = (1-\alpha)\arctan((E-E_0)/\gamma) \tag{4.13}$$

Here α is called the asymmetry parameter, $2\gamma^2$ is the full width at half maximum (FWHM) of the Lorentzian lifetime broadening, Γ is the Gamma function and E_0 is related to but not equal to the position of the maximum intensity for the core line due to assymetry of its shape. The α - parameter is

usually treated as an empirical fitting parameter and has a value between 0 and 1 characterizing the density of conduction electrons. Thus, for semiconductors and insulators $\alpha = 0$ and (4.12) yields a pure Lorentzian shape. In the particular case of the C 1s core-levels of molecular submonolayers adsorbed on the metallic surface, analyzed in the present work, the asymmetry parameter was often small (about 0.1) but not zero, as one could expect for molecules. Nevertheless, for the submonolayers the adsorbed molecules and the metal surface form an interface having a common electron system. Thus, the photoemission process from the atom within the molecule can be affected by the conduction electrons at the metal surface.

Further the Doniach - Ŝunjić line shape is additionally broadened with a Gaussian function, which originates from both fundamental and instrumental factors. The former include excitations of quantized vibrations during the photoexcitation process. Concerning the instrumental factor, it involves the non-zero width of the energy distribution of the incident photon beam as well as the instrumental function of the electron analyzer. Altogether these broadenings may be described by a convolution of the Doniach - Ŝunjić and Gaussian functions. For the XPS data included in this thesis, the total instrumental resolution was about 100 meV.

Along with the primary contribution to the XPS spectrum there is another one, often called *background spectrum*, which reflects the inelastic losses of the outgoing electron always accompanying the photoemission process. A lot of approaches have been developed for the modeling of the background behavior. The two most important ones are the so-called Shirley background[141] and more sophisticated Tougaard background[142]. Nevertheless, since all spectra analyzed in the present work have a smooth and low-intense background, it was always fitted with linear or parabolic functions, which still provide satisfactory accuracy of the fitting procedure.

The decomposition of the spectra was performed using the FitXPS program by David Adams [143]. The experimental spectrum was numerically fitted with some number of peaks having a Doniach - Ŝunjić line shape convoluted with a Gaussian plus a background curve as discussed above. Such procedure allows rather precise estimations of the fraction of atoms of the same kind in different chemical states by comparing the relative peak areas.

An example of such a fitting analysis is illustrated in Figure 4.5. It shows the C 1s XPS spectrum taken from the submonolayer of intact DBBA molecules on Au(111) at RT. The fitting procedure allows to distinguish three components constituting the photoemission line. Each of them corresponds to a group of carbon atoms having similar chemical states. Within each group the chemical state of the atoms may vary slightly, but the difference in BE of the corresponding C 1s PE lines is too small to be resolved. The results of the C 1s PE peak fitting are in excellent agreement with the model values for the relative peak area, given in parentheses. This example demonstrates the heuristic

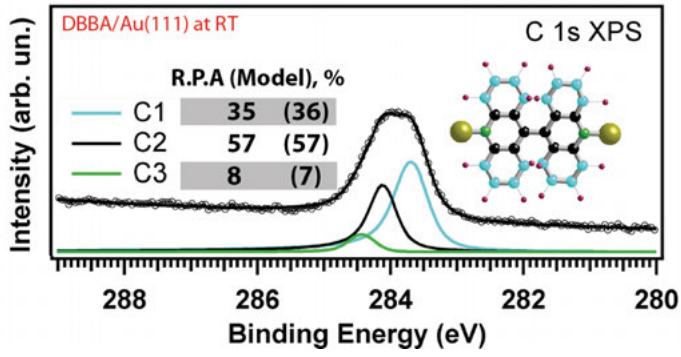

Figure 4.5. An example of a line fitting, taken from Paper I. C 1s XPS spectrum from a submonolayer of DBBA/Au(111) at RT, deconvoluted into components, corresponding to the three groups of chemically non-equivalent carbon atoms (C1, C2 and C3). Each component is color-coded on the basis of the schematic ball-and-stick model illustrated to the right (two Br atoms are yellow). In the Table the contributions of the individual components to the total C 1s signal, determined from the peak fitting analysis, are presented and compared with the corresponding values predicted by the structural model (values in parentheses).

potential of the core-level peak fit analysis which is widely employed for the analysis of the experimental data presented in the thesis.

4.1.3 Angle-resolved PES

Angle-resolved photoemission spectroscopy (ARPES) is the most important experimental technique to determine the occupied band structure of solids

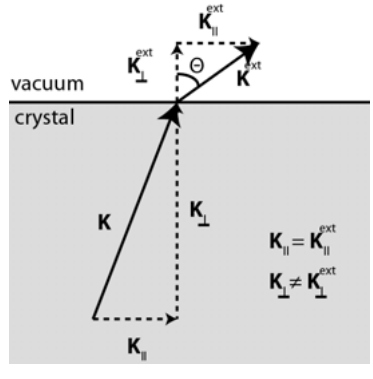

Figure 4.6. Schematic drawing which illustrates the refraction of the outgoing electron wave and the relation between the wavevector components of photoelectrons inside and outside the crystal. For more detailed information see the text.

and their surfaces. Unlike XPS, ARPES, also called angle-resolved ultraviolet photoemission (ARUPS), utilizes low photon energies. Nevertheless, the basic theory for calculating the photoemission cross section described in section 4.1.1 can be applied for ARPES as well. The need for lower photon energies is two-fold. On the one hand, for the high photon energies used in XPS, the cross section for valence band photoemission is very small. On the other hand - lower photon energies prevent significant averaging of the photoemission signal over the surface BZ, which makes ARPES a perfect tool for mapping the sample's band structure, *i.e.* $E_B(\mathbf{k})$.

Being interested in the surface electronic structure of solids and materials with reduced dimensionality, we can limit ourselves to studies of the two-dimensinal band structure $E_B(\mathbf{k}_\parallel)$. Fortunately, this is much simpler than studying the dispersion of bulk states $E_B(\mathbf{k})$ with a three-dimensional $\mathbf{k}$ vector. Indeed, upon the transition through the sample surface the electrons are refracted (see Figure 4.6), *i.e.* the perpendicular component of the photoelectron wavevector ($\mathbf{K}_\perp$) is not conserved in the photoemission process due to the effect of the potential step on the crystal surface. As a result, the determination of $E_B(\mathbf{k})$ requires knowledge of the crystal potential and exact refraction of $\mathbf{K}_\perp$. On the other hand, in the two-dimensional case $\mathbf{K}_\perp$ can be excluded from the consideration. In contrast to $\mathbf{K}_\perp$, $\mathbf{K}_\parallel^{ext} = \mathbf{K}_\parallel$ since translation symmetry of the crystal is not broken in the parallel direction. Therefore for the parrallel component of the electron wavevector the momentum conservation law can be represented as $\mathbf{K}_\parallel^{ext} = \mathbf{K}_\parallel = \mathbf{k}_\parallel + \mathbf{G}_\parallel$ (see equation 4.7), thus making it possible to obtain value of $\mathbf{k}_\parallel$ directry from the measured distribution of photoelectrons.

Utilizing the model of free-electron final states and the reduced zone scheme which includes all inequivalent values of $\mathbf{K}_\parallel$, we can calculate $\mathbf{k}_\parallel$ from the kinetic energy E_K and the emission angle Θ (see Figure 4.6):

$$\mathbf{k}_\parallel = \mathbf{K}_\parallel^{ext} = sin\Theta \left| K^{ext} \right| = sin\Theta \frac{\sqrt{2m_e}}{\hbar} \sqrt{E_K} \tag{4.14}$$

In the present thesis ARPES was implemented to investigate the 1D electronic structure of 7-AGNRs grown on a vicinal Au(788) surface before and after intercalation of copper (**Paper V**). As an example, Figure 4.7 illustrates the ARPES intensity plot recorded for the clean Au(788) surface in the vicinity of the Γ point of the surface BZ. The Au(788) surface consists of (111)-oriented terraces of width $\omega = 3.8$ nm. Such regular steps form a 1D superlattice giving rize to the replicas of the free-electron-like gold surface state due to the scattering of the outgoing electron wave on the regular step edges [144].

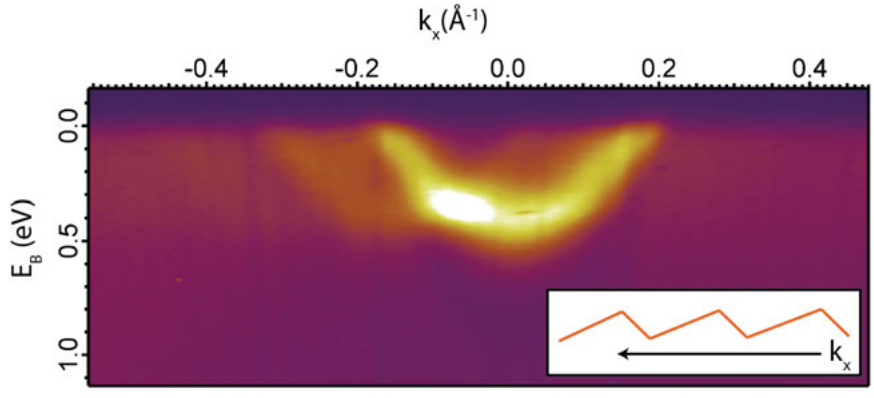

Figure 4.7. ARPES data recorded for the Au(788) surface in the vicinity of the Γ point of the surface BZ. Photoelectron angular resolution is measured in the direction perpendicular to the step edges of this vicinal surface, as shown at the inset. The free-electron-like gold surface state and its replicas appearing due to the superlattice folding effects are clearly visible.

4.1.4 Instrumentation

In order to measure the kinetic energy distribution of the photoelectrons, an *electron analyzer* has to be used. In this section a short overview of the hemispherical electron analyzer (HSA) working principle, which is required for the general understanding of the XPS and ARPES experiments, will be given.

A cut through the mirror plane of the HSA is shown in Figure 4.8 (a). A focused monochromatic photon beam illuminates the surface at a certain angle[5]. The emitted electrons pass through a first electrostatic lens system (L1) which focuses them on the decelerator[6]. At this point electrons are decelerated down to the pass energy (E_{pass}) - the mean kinetic energy of the electrons which are able to pass through the analyzer. The second electrostatic lens system (L2) begins just after the aperture and focuses the electrons on the entrance slit of the spectrometer (S1). The electrons enter between two concentric conductive hemispherical plates, which have an applied potential difference. Inner hemisphere has a positive potential, thus attracting electrons, and the outer one is on the negative repulsive potential. The value of the voltage on the hemispheres is chosen in a such a way that only electrons with $E_{pass} \pm \Delta E$ are able to path through the exit slit (S2) to the detector. Electrons with too low kinetic

[5]Typically the UHV chamber is designed in a such a way that the angle between the polarization vector of the the incoming photon beam and the axis of the analyzer (the wavevector of the photoelectron) is close to 54.7°. This angle is known as the "magic angle" since at this angle the differential photoemission cross section does not depend on the symmetry of the electron orbital. The UHV chambers at D1011 and I4 at MAX IV are not at exception.

[6]The voltage on the decelerator is changing while the analyzer measures the scan in the user-defined kinetic energies range.

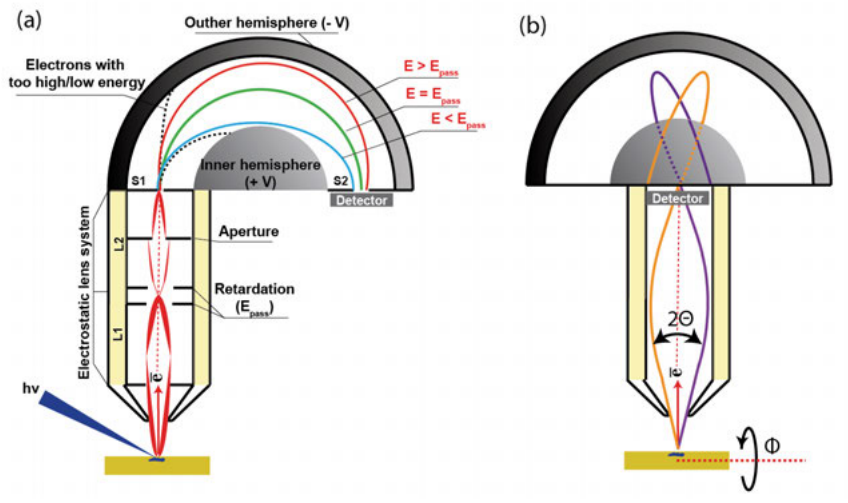

Figure 4.8. Schematic drawing of a HSA with a 2D detector showing two planes used for energy (a) and angular (b) resolution. For more detailed information see the text.

energies will hit the inner hemisphere and electrons with too high energies - the outer one, and thus will be lost. Electrons with E_{pass} will be centered at the detector, while the ones having lower or higher energy will reach the detector closer to the inner or outer hemisphere, respectively. The detector is a two-dimensional position sensitive detector containing channel plates, which permits an energy resolution along its length.

In order to measure ARPES the photoemitted electrons also need to be detected as a function of their emission direction. In that mode electrons having the certain kinetic energies $E_{pass} \pm \Delta E$ and emission angles $\pm\Theta$ are detected. Indeed, as can be seen from Figure 4.8 (b), electrons entering the HSA in an angular range of $\pm\Theta$ from the centre axis of the lens (orange and violet trajectories) are projected on the direction of the detector, which is perpendicular to the direction of energy dispersion. If the electron analyzer probes a large angular range in one direction (Θ in Figure 4.8 (b)), the other angular component can be probed by rotating the sample (Φ in Figure 4.8 (b)).

The energy resolution of the electron analyzer depends on the pass energy, the size of entrance slit S1, s, and the mean radius of curvature of two hemispheres, R_{mean}. Without taking into account the angular width of the electron distribution, ΔE can be given by:

$$\Delta E = \frac{E_{pass} s}{2R_{mean}} \tag{4.15}$$

E_{pass} and s can be changed during the experiment. However, both parameters influence the transmission of the spectrometer and a balance between resolution and electron count rate needs to be found.

4.2 X-ray absorption spectroscopy

X-ray Absorption Spectroscopy (XAS) is a powerful and well-established tool which yields element-specific information about the energy distribution and symmetry of the unoccupied states, the chemical state of the absorbing atom and also about interatomic distances. A lot of literature is devoted to XAS, and the description of the technique presented below is based on several sources [145–147].

In the original form the X-ray absorption experiment corresponds to measuring the X-ray intensity (I) transmitted through the sample. The attenuation of the X-ray beam while passing through the sample is described by the Beer-Lambert-Bouguer law in a simple form:

$$I = I_0 e^{-\tau x} \tag{4.16}$$

Where I_0 corresponds to the initial intensity, x - is the path length in the material and τ is the linear attenuation coefficient which contains all the physics needed to understand XAS. Furthermore τ can be represented as a sum: $\tau = \mu + \sigma_s$. The last term σ_s is the linear scattering coefficient, taking into account effects of coherent and non-coherent X-ray scattering. The former one, μ, also called the linear absorption coefficient, describes the changes in the transmitted intensity occurring due to the "pure" photoelectric absorption. In the interval of photon energies of 150 - 2000 eV, used in the present work, the photoexcitation processes (μ) dominates and the influence of X-ray scattering can be neglected.

Absorption of a photon either leads to an ionized atom, if the photoelectron is lifted to the continuum, or to an excited atom, if the photoelectron fills an unoccupied atomic or molecular orbital state below the ionization threshold. The continuum absorption normally starts stepwise at the "edge", corresponding to $\hbar\omega = E_{ion}$ (E_{ion} - ionization energy of a certain atomic shell). Thus, the position of the adsorption edge naturally contains information about the chemical species present in the sample and their oxidation states. Going above the absorption edge leads to a monotonous decrease of the cross section until the photon energy reaches the value of the ionization energy for a deeper atomic shell. A closer look at the behavior of the absorption coefficient in the vicinity and far away from the absorption edge allows to distinguish two characteristic regions:

- The one which starts approximately 40 eV above the absorption edge, where the X-ray absorption spectrum reveals broad low-intensity oscillations. These oscillations are usually defined as Extended X-ray Absorption Fine Structure (EXAFS).
- The second region, on the contrary, called Near-Edge X-ray Absorption Fine Structure (NEXAFS). It starts 5-10 eV below the absorption edge and continues up to 30 - 50 eV above the edge. In most cases this part

of the spectrum is dominated by intense and well-developed absorption structures.

In general, the difference between NEXAFS and EXAFS relates to the physical processes occurring after the photoelectron have been created, which allows to derive different information from the two regions. The border between the regions is not fixed, but can be approximated by comparing the interatomic distances, d_i, and the photoelectron wavelength λ_e:

- For small $\lambda_e < d_i$ (big **k** value) single scattering dominates, leading to smaller changes in the absorption spectrum. This defines the EXAFS regime, which contains information about bond lengths and coordination numbers.
- For big $\lambda_e > d_i$ (small **k** value), multiple scattering occurs and backscattering restricts photoelectron mostly within first coordination sphere, which can be described as the transitions of the core-electron to the unoccupied states localized in the vicinity of absorbing atom. Thus the NEXAFS profile contains rich information about the chemical bonding of the absorbing atom with its nearest surrounding.

Together with PES, NEXAFS spectroscopy is one of major experimental techniques used in the present work, so below the brief description of the NEXAFS concepts is given.

4.2.1 Near-edge X-ray absorption fine structure spectroscopy

Despite the fact that the quantitative analysis of NEXAFS spectra is not straightforward and complicated since it requires the description of multiple electron wave scattering, the qualitative interpretation can provide a lot of information about the system under study.

As was mentioned above, the low-kinetic-energy electrons undergo multiple scattering on the scattering centers closest to the absorbing atom. At certain energies this process results in the temporal "capture" of the photoelectron within the area including the absorbing atom and the atoms of it's nearest surrounding (*quasimolecule*). It turns out that such resonances can be quite accurately described as one-electron photoexcitations of the inner-shell electrons to the unoccupied orbitals of the polyatomic system. In a first approximation the resonance effects do not depend on the arrangement of atoms in the second and succeeding coordination spheres, and thus persist in more complex polyatomic systems. Such an approximation is called the quasi-molecular approach and allows to describe the NEXAFS structures in terms of transitions of core-level electrons into unoccupied molecular orbitals (MO's) of the quasimolecule [148].

In the case of molecules, such interpretation of NEXAFS appears even more natural, since the resonances in NEXAFS can be directly associated with dipole-allowed excitations of the inner-shell electron to unoccupied MO's hav-

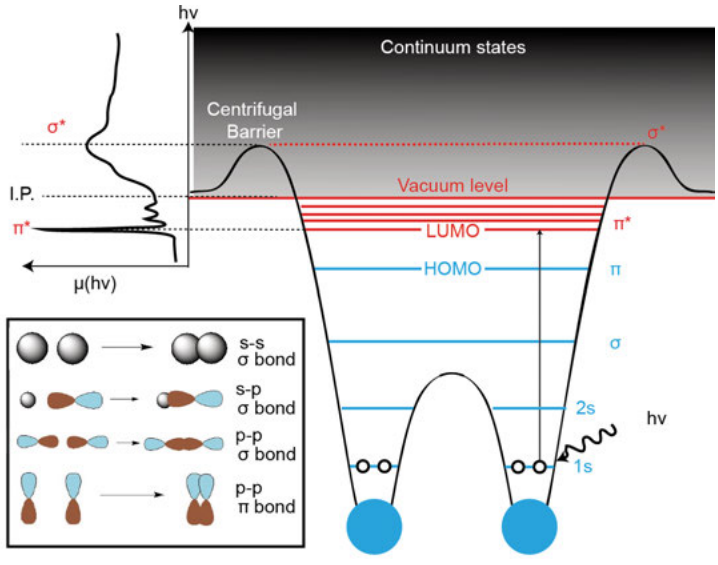

Figure 4.9. Diagram showing the formation of the K-shell spectrum for a diatomic molecule. The inset shows the schematic of the σ and π bond formation. LUMO - Lowest Unoccupied Molecular Orbital, HOMO - Highest Occupied Molecular Orbital.

ing the appropriate symmetry. In general, the simplest MO symmetry classification, which is valid also for polyatomic molecules, is in terms of σ and π orbitals. For σ orbitals or bonds there is no nodal surface that contains the bond axis, while a π orbital has one nodal surface or plane containing the bond axis. The σ bond is always present, while the existence of π bonds depends on the atomic constituents of the molecule and the number of valence electrons available for bonding.

For the K-shell spectra, investigated in this work, the observed NEXAFS resonances correspond to the *dipole allowed* transitions of a 1s core-electron to π^* and σ^* antibonding orbitals of at least partial p-character. The schematic potential and 1s spectra of a diatomic molecule is shown in Figure 4.9 together with the inset illustrating the formation of σ and π orbitals. The initial 1s state is always of σ symmetry, while the final state arises from mixing s and p or p and p orbitals and may be of both π^* or σ^* character (see inset in Figure 4.9). If π bonds are present, the lowest unoccupied molecular orbital is usually a π^* orbital, and therefore the lowest energy resonance is the π^* resonance. In most cases, the π^* - resonances are found below the ionization threshold as they are shifted below the ionization potential (I.P.) level by the additional Coulomb electron-hole interaction. The π^* resonances always appear in the absorption spectrum of molecule as sharp, well-defined resonances, since the excited electron is confined to the vicinity of the excited atom by the effective

potential landscape containing a potential barrier. On the other hand, the σ^* resonances are found above the I.P. and appear to be much wider due to significantly shorter lifetime of the excited state (so-called "*shape resonances*").

Anisotropy of absorption cross section

In the framework of this one-electron approximation the physical principle which is exploited in NEXAFS is not different from the one in XPS: the absorption of photons causes transitions of the bound electrons to unoccupied states in the vicinity of the ionization threshold. Therefore an Equation similar to (4.7) can be applied for the absorption cross-section [7] [145]:

$$\sigma \propto |\langle \varphi_f, \mathbf{k}_f | \mathbf{ur} | \varphi_i, \mathbf{k}_i \rangle|^2, \tag{4.17}$$

where **u** is the polarization vector of incident radiation and **r** - coordination vector of photoelectron. Thus, assuming 100% polarization of the incoming radiation, we obtain:

$$\sigma \propto |\langle \varphi_f, \mathbf{k}_f | r | \varphi_i, \mathbf{k}_i \rangle|^2 \cdot \sin\theta^2 \tag{4.18}$$

Here θ corresponds to the angle between the direction of the dipole momentum of the electron transition and the wave vector of an incident photon. From (4.18) it is clear that the probability of electron excitation, and hence X-ray absorption, is maximum for the transition momentum parallel to the incident radiation polarization vector and minimal in the direction normal to it.

The anisotropy of X-ray absorption can be effectively used for investigating the spatial localization of the unoccupied states of certain symmetry and the orientation of the adsorbed molecules with respect to the substrate.

In Figure 4.10 a set of angular dependent absorption spectra for DBBA on Au(111) at different substrate temperatures is shown (data taken from **Paper I**). The schematics, depicting the relative orientation of the π^* and σ^* states with respect to the incidence radiation polarization vector for the sample annealed to 400°C, is also shown. It can be seen that the angular dependence is weak for the DBBA molecule and the polymer chain, since they are not flat and thus their σ^*/π^* states are not entirely parallel/perpendicular to the Au(111) substrate. In turn, when the graphene nanoribbon is formed, upon normal incidence the XAS structure is governed by the transitions to σ^* states and the electron transitions into the π^* states are suppressed at this angle. For the grazing incidence angle the situation is opposite. As can be seen from the schematics, this is fully consistent with formula 4.18. Such pronounced angular dependence is a clear signature of the flattening which occurs upon annealing at 400°C, corresponding to the formation of flat graphene nanoribbons.

[7] Of source, if we consider the quasimolecule, we should omit the translation symmetry.

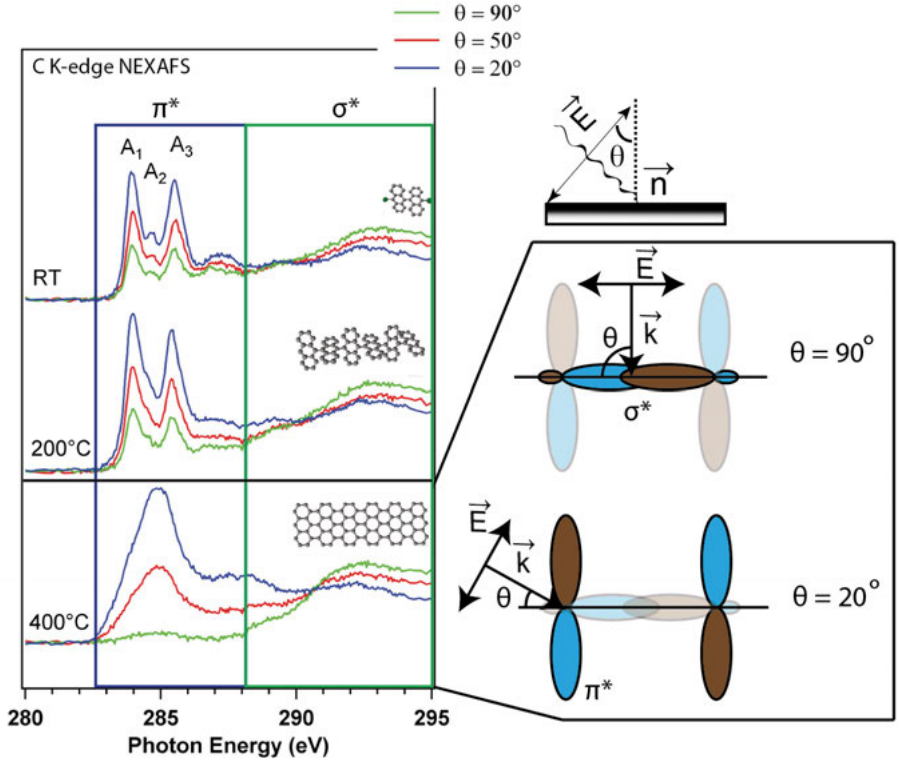

Figure 4.10. Angle dependent C-K edge NEXAFS spectra of DBBA/Au(111) at different substrate temperatures, characteristic for intact and not flat DBBA (RT), tilted polymer chain (200°C) and flat graphene nanoribbon (400°C) as illustrated by the ball-and-stick models. The inset in the top right corner shows the relation between the sample orientation and the angle between the sample normal and polarization vector of the incident radiation (θ). For the case of flat graphene nanoribbons on Au(111) two additional insets are inserted to the right. They demonstrate the relative orientation of the σ* states and the polarization vector at normal incidence ($\theta = 90°$) and the relative orientation of the π* states and the polarization vector at grazing incidence ($\theta = 20°$).

Acquisition of X-ray absorption spectra

The measurements of a NEXAFS spectrum can be performed in a number of ways including (i) transmission measurements, as well as (ii) fluorescence-, (iii) total-, partial- and Auger electron yield measurements [145]. The obvious drawback of the transmission geometry is that it naturally requires very thin foils to be used as samples and cannot be performed on a bulk single crystal as was used in our experiments. In turn, the possibilities for the fluorescence yield method are limited for low-Z elements, such as B, C, N, O, which are studied in the present work, due to the low probability of the fluorescent final state de-excitation.

The most favorable path is to measure secondary electrons leaving the sample, since for the low-Z elements the cross-section for the electronic Auger decay is more that two orders of magnitude higher than for the fluorescence decay. As was demonstrated in the pioneering works by A. P. Lukirskii and co-workers from Leningrad State University, USSR [149, 150], owing to the fact that the photon penetration depth is much larger than the electron escape depth, the electron yield signal is directly proportional to the absorption coefficient μ.

In the case of the Auger electron yield measurements, only Auger electrons with a fixed energy, corresponding to a particular de-excitation channel, are measured using an electron analyzer. On the other hand, if one is measuring the total current of *all* photoelectrons escaping the sample (including inelastically scattered and Auger electrons), this mode is called Total Electron Yield (TEY). It can be practically realized by reading out the drain current to the sample. This is a rather simple way to perform XAS experiments and, therefore, widely used. Nevertheless, the lack of surface sensitivity represents a significant drawback of the TEY mode if one is going to investigate submonolayers of adsorbates on a bulky substrate. Indeed, in this case the signal is dominated by multiple scattered electrons with an escape depth of 10-20 nm (see Figure 4.3). The higher surface sensitivity, comparable with the surface sensitivity of XPS, can be achieved by excision of secondary electrons from the measured signal. Such technique is referred as Partial Electron Yield (PEY) and can be implemented in an experimental set-up as an electron detector (often an MCP) placed near the sample having a couple of conducting (*e.g.* gold) grids in front of it. The outer grid is kept grounded, while the inner grid is kept at a certain retarding potential and can be used for cutting off the slowest electrons. Thus for a non-zero retarding potential, only electrons with energies above the retarding threshold contribute to the PEY signal. Since high surface sensitivity was required for the measurements in the current thesis , all of the presented NEXAFS spectra were measured in the PEY mode.

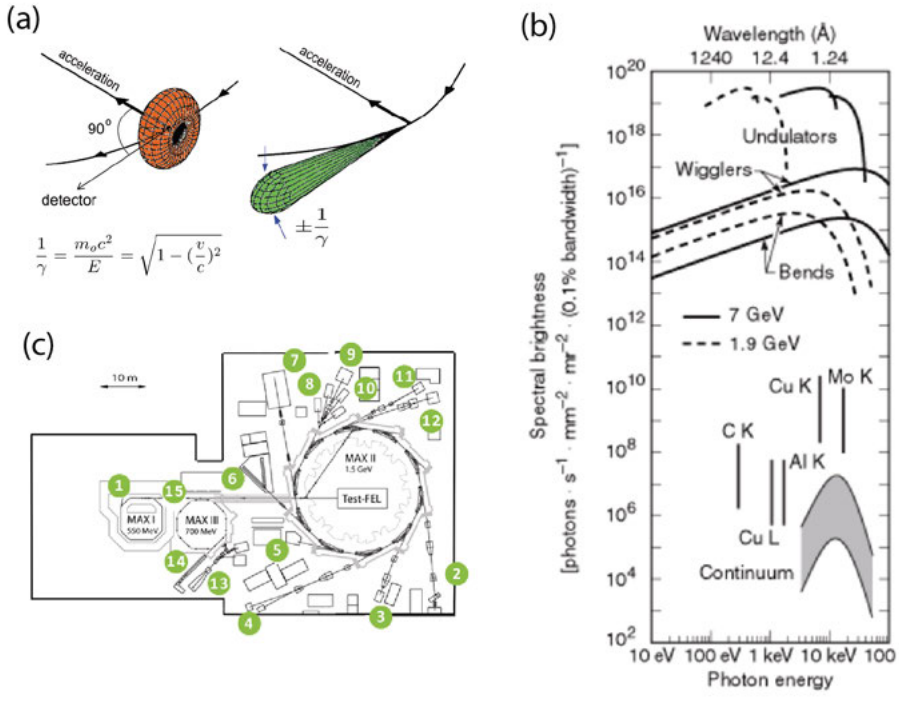

Figure 4.11. Synchrotron radiation: (a) Projector effect for the relativistic (right) charged particle; (b) Spectral brightness for several synchrotron radiation sources and conventional X-ray sources; (c) Schematics of the MAX-lab (old site) synchrotron radiation facility. *Images (a),(b) and (c) are copied from* [151, 153, 154], *respectively*.

4.3 Synchrotron radiation facilities

More than 100 years has passed from the day when W. C. Röntgen discovered the X-rays. Since that time, X-ray sources have evolved from the X-ray tubes (which are still widely used nowadays as compact laboratory sources) to the huge specialized facilities - synchrotrons, capable of producing high-intense X-rays in a wide spectral range. First noticed in the 1940s as a parasitic energy-loss phenomenon in electron storage rings [151, 152], synchrotron radiation (SR) has developed into a valuable tool in many disciplines. In particular, XPS and XAS experiments, presented in this thesis have been carried out at the MAX IV laboratory in Lund, Sweden. During the last years the MAX IV laboratory comprised both the old MAX-lab and the new MAX IV project. The experimental data presented in this work were taken at MAX-lab. Nevertheless, by the time when the present thesis was finished, MAX-lab was already decommissioned and the story of the new MAX IV synchrotron, which is going to take a leading role in that field, has begun.

According to classical electrodynamics, electrons accelerated in space should radiate. A French physicist Alfred Liénard of the Ecole des Mines in Paris described the concept of the circular motion of charged particles, and gave the rate of energy loss by an electron traveling in a circular path, thus giving birth to the first basic theory of what is now known as synchrotron radiation [152]. In Figure 4.11 (a) the radiation pattern of an accelerated electron (or any other charged particle) is depicted for the case of non-relativistic (left) and relativistic (right) velocities. In the relativistic case, as measured in the laboratory frame of reference, the Lorentz transformation causes a drastic change in the spatial distribution of an emitted radiation from donut-like to a narrow cone with a divergence of $\frac{1}{\gamma}$ in the direction of electron motion ($\frac{1}{\gamma} = \sqrt{1 - \upsilon^2/c^2}$ - Lorentz factor). The emitted synchrotron radiation covers a wide spectral range and has a high degree of linear polarization in the plane of the electron orbit, while out of orbit elliptically polarized light is emitted. In addition, the brilliance of the synchrotron radiation is far superior to that of more conventional X-ray sources (see Figure 4.11 (b)). Starting from the late 1960s a continuous advancement of synchrotrons occurred and the brightness and degree of coherence of the light produced have kept increasing. Third generations synchrotrons[8] are exceptionally much brighter than the first facilities of this kind. Nevertheless, the development is still ongoing and a generation of "diffraction limited" synchrotrons is preparing to take the lead. In particular, the new MAX IV facility is going to start operating in the outskirts of Lund. Its design is based on innovative technology and scientific breakthroughs developed at MAX-lab over the last few decades. The MAX IV facility will be the most brilliant synchrotron light source in the world where scientists will be able to explore different materials and substances with better resolution and on shorter time and length scales than previously possible.

Let us quickly describe the general operation principle of the synchrotron radiation facility. Electrons are produced in an electron gun and accelerated in a linear accelerator - so-called Linac or a booster synchrotron. The storage ring in a simplest form consists of straight sections joined by bending magnets. Additionally a number of quadrupole magnets is used to control the electron orbit and focus the electron beam. Upon traveling through the bending magnet, the electrons emit synchrotron radiation, which is directed down beamlines to experimental stations where particular wavelengths may be selected by a monochromator. When emitting SR the electrons lose some of their energy, which is compensated in radio-frequency cavities, situated in straight sections of the storage ring. The earliest synchrotron radiation facilities exclusively used bending magnets to produce the radiation. More recent facilities have incorporated insertion devices such as undulators and wigglers. Figure 4.11 (c) shows the schematics of the MAX-lab synchrotron radiation facility, which included three storage rings MAX I (550 MeV), MAX II (1.5 GeV) and MAX

[8]MAX II and MAX III storage rings were among them.

III (700 MeV) [9]. The experiments described in the thesis have been performed at the D1011 bending magnet beamline at MAX II and the I3 and I4 undulator beamlines at MAX III and thus the short description of the beamlines is given below.

4.3.1 Beamlines at MAX-lab

D1011 beamline

Beamline D1011 was a MAX II bending magnet beamline, designed for probing the core-levels of light elements (C, N, O, Si, *etc.*) and covering photon energies between 40 - 1500 eV with high resolution. The bending magnet of the beamline D1011 at MAX II was also equipped with a set of quadrupole magnets, which made it possible to control the degree and direction of light polarization. The beamline was equipped with two experimental endstations: front (EXP1) and back station (EXP2). The front station allowed to perform measurements with the main spectroscopy techniques: XPS and NEXAFS in both PEY and TEY modes. It was equipped with a Scienta SES-200 HSA and a PEY detector. Moreover, the preparation chamber had a set-up for Low Energy Electron Diffraction (LEED) measurements, an Ar^+ gun and a mass-spectrometer. The back station offered opportunities for X-ray Circular Magnetic Dichroism measurements.

The EXP 1 chamber was mounted directly after the slit of the monochromator (S1), while EXP 2 was mounted further downstream and received radiation passing *via* a re-focusing mirror system. By changing the slit size of S1 we could change the photon energy resolution and, at the same time, the photon flux on the sample. In our photoemission experiments the total energy resolution of the beamline and HSA was maintained at about 0.1 eV.

I3 and I4 beamlines

Although the D1011 beamline was capable of some ARPES measurements, the parameters of the MAX II storage ring were not suitable for the SR research at the ultraviolet energy range. The MAX III storage ring was specially designed for this purpose. It was the home of two ARPES-dedicated beamlines, I3 and I4. Both I3 and I4 were undulator beamlines for the low energy region of 5 - 50 eV and 15 - 200 eV, respectively. The technical details of the beamlines can be found in Ref. [154]. The undulators of both beamlines provided high photon flux at low energies. The overall design and instrumentation of the experimental endstations were different on these two beamlines. Nevertheless, both stations were equipped with the set of instruments for preliminary sample characterization and ARPES measurements.

The analysis chambers of endstations at I3 and I4 were equipped with manipulators, which allowed precise alignment of the sample in **k**-space, and

[9] All three are out of operation from December 2015.

HSAs for high-resolution ARPES measurements (Scienta R4000 combined with a Mott Detector at I3 and SPECS Phoibos 100 at I4). Both stations comprised preparation chambers for sample treatment, and a load-lock systems for introducing samples. Each preparation chamber was equipped with an ion gun for cleaning samples and a LEED for surface analysis. For ARPES measurements the Scienta R4000 and SPECS Phoibos 100 HSAs were operated at the maximum acceptance angle of $\pm 15^\circ$ and $\pm 10.5^\circ$, respectively, with an angular resolutions of 0.4° in both cases.

4.4 Scanning tunneling microscopy (STM)

As was shown in the previous sections, spectroscopic techniques allow to obtain a lot of information about the electronic structure of the material and chemical state of the atoms in it. On the other hand, such data always carry the averaged information and its interpretation frequently requires physically justified models. Especially this is the case for the investigation of the bottom-up processes of the growth of supramolecular structures, which occur through various intermediate stages - each with its characteristic atomic configuration. Therefore the combination of spectroscopy methods with some sort of microscopy technique, providing information about the sample with atomic-level precision, is highly desirable. Usually, and this work is not an exception, this role is assigned to the Scanning Tunneling Microscopy, which has become a "must" routine for studying on-surface processes.

STM was developed at IBM Zurich in the early 1980s by G. Binnig and H. Rohrer [155]. Rapidly it has become an important standard technique in surface science which brought the Nobel Prize to its inventors already in 1986. STM relies on the basic principle of a quantum-mechanical tunneling junction, characterized by the exponential dependence of the tunneling probability on the width of potential barrier. The basic operation principle of STM is sketched in Figure 4.12. An atomically sharp probe (tip), usually made of W or a Pt-Ir alloy, is attached to a scanning unit - a piezo tube scanner, whose dimensions can be controlled by the external applied voltages. The scanning unit can be positioned with respect to the sample with an extremely high accuracy of about 1 pm. Using a piezo drive, the tip and the sample are brought to within a few Å from each other. The electron wave functions of the *biased* tip and the sample start to overlap at such small distances, thus causing an electrical current (tunneling current, I_T) to flow. The STM images are acquired by raster-scanning the STM tip laterally over the conducting sample while measuring the tunnel current. Applying the simplest quantum-mechanical model of the tunneling through a one-dimensional barrier, one can derive that the probability density of the wavefunction tunneling and hence I_T depends exponentially on the tip-sample separation, d, with [156]:

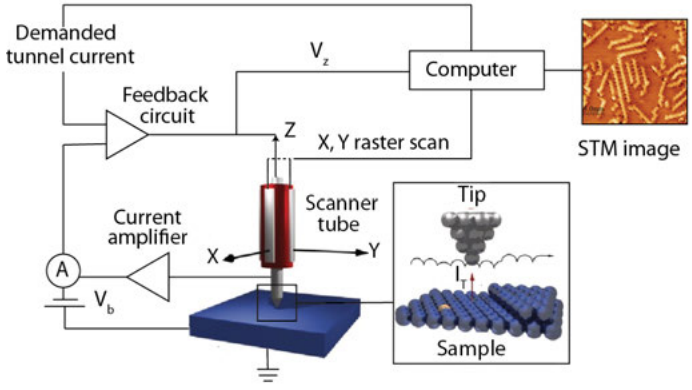

Figure 4.12. Schematic drawing of an STM setup, showing a feedback system used to control the tip-sample separation during operation. When a bias voltage is applied to the sample, there is a tunnel current between the sample and the tip located at a distance of about 1 nm from each other. If the current is kept fixed, a topographic image of the surface may be obtained.

$$I_T \propto \exp^{-ad\sqrt{\Phi}} \tag{4.19}$$

Where a is a constant and Φ is the tunnel barrier height between the tip and the sample. Due to this exponential relation, the value of I_T is extremely sensitive to the tip-sample separation: the tunneling current typically increases by an order of magnitude for a 1 Å decrease in the tip-sample separation. Therefore, by maintaining $I_T = I_0$ (I_0 is the certain preset value), one can control the position of the tip over the surface with subatomic precision. The tunneling current is amplified by the current amplifier generating a voltage, which is then compared with the reference value. The feedback loop adjusts the tip-substrate distance using the difference value (V_z) in order to keep the current fixed. As the tip scans over the xy plane, a two dimensional array of equilibrium z positions, representing a contour plot of the equal tunneling current surface, is obtained and stored. This type of STM operation is the one most commonly used and is called constant current mode. All of the STM images presented in the thesis were obtained in the *constant current mode*, which allows to image soft materials such as organic molecules without destruction. For the so-called *constant height mode*, on the contrary, the tip-sample distance is held constant while the tunneling current is detected at each point. Since the feedback loop is off, the risk of crashing the tip into the surface is very high.

Figure 4.13 shows schematic energy diagrams for the tunneling process in the STM setup. As can be seen, the electron transfer is facilitated by the bias voltage (V_b), applied between the tip and the sample (in our case the sample was grounded). When $V_b = 0$, the Fermi levels E_{Ftip} and $E_{Fsample}$ are aligned, and there is no net current. If the tip is biased negatively ($V_b < 0$), E_{Ftip} will

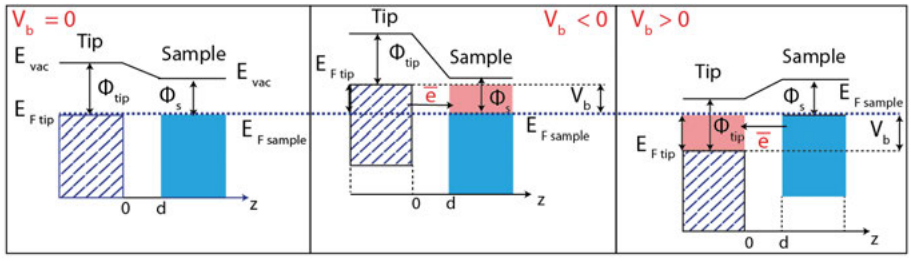

Figure 4.13. Schematic energy diagrams, showing a metal-vacuum-metal tunneling junction at different bias voltages, applied to the tip (V_b). If $V_b < 0$, electrons flow from the occupied states of the tip to the unoccupied states of the sample. If the $V_b > 0$, the electron flow is directed from the sample to the tip.

move with respect to $E_{Fsample}$ by eV_b, thus allowing electrons occupying energy levels between between E_{Ftip} and $E_{Ftip} - eV_b$ to tunnel across the gap into the empty states of the sample between $E_{Fsample}$ and $E_{Fsample} + eV_b$. For the case where the tip is biased positively ($V_b > 0$) the situation is opposite. Therefore, in reality, the tunnel current includes a complicated convolution of the electronic structure of the tip and the sample. The complete theoretical description of STM is out of the scope of the work and can be found in the literature [156]. Below the main approaches, which are useful for the calculation of the tunneling current, will be cited.

4.4.1 Theoretical aspects of STM

The most extensively used theoretical method for the understanding of the metal-vacuum-metal tunneling junction is the time-dependent perturbation approach developed by Bardeen (1960) [157], which turned to be sufficiently simple for treating many realistic cases, and has been successfully used for describing a wide variety of effects [156]. By Fermi's Golden Rule the tunneling current is given by the Fermi distribution function, $f(E)$, the bias voltage, V_b, and the tunneling matrix element, M, between the tip states and the states of the surface, characterized by the density of states, ρ_t and ρ_s, respectively. Considering the case when $V_b > 0$ (positive voltage applied to the tip) we get:

$$I_T = \frac{4\pi e}{\hbar} \int_{-\infty}^{\infty} [f(E_F - eV_b + \varepsilon) - f(E_F + \varepsilon)] \times \rho_s(E_F - eV_b + \varepsilon)\rho_t(E_F + \varepsilon)\,|M|^2\, d\varepsilon \quad (4.20)$$

The matrix element can be expressed as a integral over the surface, S, lying in the region between the tip and the sample:

$$M_{s,t} = \frac{\hbar}{2m} \int_S (\psi_s * \nabla \psi_t - \psi_t \nabla \psi_s *) dS \tag{4.21}$$

It is, therefore, determined by the overlap of the surface wave functions, ψ_s and ψ_t, of the two electrodes. If the Fermi distribution function is approximated by a step function in Equation 4.20, the tunneling current is:

$$I_T = \frac{4\pi e}{\hbar} \int_0^{eV_b} \rho_s(E_F - eV_b + \varepsilon) \rho_t(E_F + \varepsilon) \, |M|^2 \, d\varepsilon \tag{4.22}$$

Obviously, in order to be able to calculate the tunneling current, the wave functions of both tip and sample, through which tunneling occurs, have to be known. In general this is not possible and therefore further simplifications are needed. One of the simplest approaches was suggested by J. Tersoff and D. R. Hamann [158] who modeled the tip function as an s - wave and showed that the STM images reflect the topography and local density of states (LDOS) at the Fermi energy at the center of the curvature of the tip r_0:

$$I_T \propto eV_b \rho_s(r_0, E_F) \tag{4.23}$$

This result is quite representative since it demonstrates that STM is indeed a *local* probe and that the STM spatial resolution significantly depends on the tip shape. If the tip is sharp and the tunneling current flows through the one atom, situated at the tip apex, atomic resolution can be achieved in the STM picture. But the real situation is often more complicated than what is assumed in the s-wave tip model, since other orbitals can contribute to the tip wave function.

A useful expression for the tunneling current can be obtained by summarizing Equation 4.19 and Equation 4.22 assuming that the LDOS of the tip and the sample are approximately constant within the energy interval, determined by V_b:

$$I_T \propto \rho_t \cdot \rho_s \cdot \exp^{-ad\sqrt{\Phi}}, \tag{4.24}$$

where ρ_t and ρ_s are the electron LDOS in the vicinity of the Fermi level.

Image interpretation

The complicated nature of the tunnel current means that it is not always (or, maybe I should say "always not") acceptable to understand STM images as direct representations of the surface topography. In reality the STM image depends on many factors like bias voltage, tip configuration, tunneling current, sample electronic structure *etc.*, therefore one should be really careful when interpreting STM images. To some extent, STM images are rather the convolution of the geometric and electronic structure of the surface plus the electronic structure and configuration of the tip. Figure 4.14 shows an example of different images of the same sample (DBBA/Cu(110) after 250°C

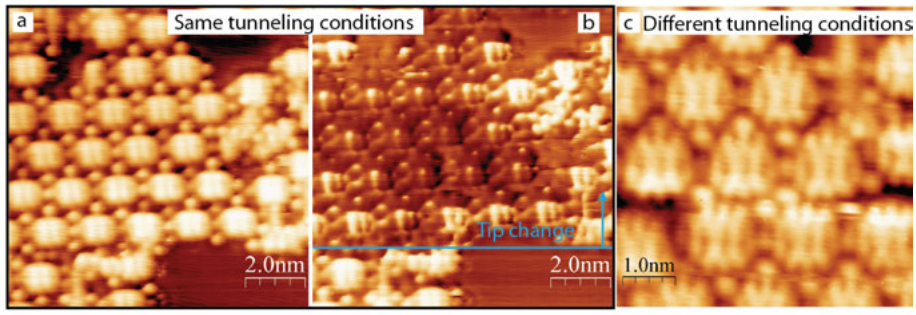

Figure 4.14. Examples of different modes of imaging of the same sample with STM. The presented system is DBBA/Cu(110) after a 250°C anneal as discussed in Paper III. Images (a) and (b) demonstrate a tip effect. They were obtained using the same tunneling conditions (V_b/I_T), nevertheless at the bottom part of image (b) the tip change occurred (indicated by the cyan line and arrow) which leads to the completely different STM picture. Image (c) is taken from the same system as (a) and (b), but now at a different V_b/I_T. The variations of the LDOS within each individual "square" unit can clearly be seen.

anneal, see Paper III for description). The images in Figure 4.14 (a) and (b) are taken from the same area with the same tunneling conditions. Nevertheless a tip change occurred at the bottom part of picture (b) which results in a completely different image mode. Such a tip change may happen if molecules or any other adsorbates attach to the tip apex. Figure 4.14 (c) shows the STM image taken under different tunneling conditions, which leads to the appearance of the new details in comparison with Figure 4.14 (b). Nonetheless, on the large-scale, that is on the tens to hundreds nanometer range, STM provides reliable information on the topography of the sample.

4.4.2 Experimental setup

The STM images presented in the thesis have been obtained mainly using the MAX IV laboratory STM system (VT STM XA, Omicron Nanotechnology GmbH) and cross-checked in a separate analogous STM system (group of Dr. A. A. Cafolla, DCU, Dublin, Ireland). Both stations consist of a fast entry load lock and two UHV chambers: one for sample preparation and another one which contains the STM. Without going into the technical details of the experimental stations, some important features of the STM machine have to be discussed. The main components of the Omicron VT STM XA are labelled in Figure 4.15. The STM is effectively isolated from vibrations by the spring suspension and the Omicron eddy current magnetic vibration damping system. The sample stage can be cooled down to liquid nitrogen temperatures and heated up to 300°C, which allows to investigate the temperature evolution

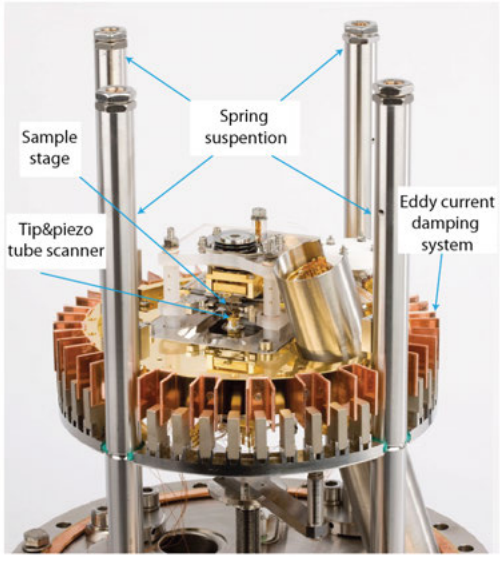

Figure 4.15. The design of the VT STM from Omicron GmbH. *Copied from* [159]

of the systems under study without taking it out from the STM. Measuring the STM images at low temperatures significantly improves their quality by reducing the thermal motion taking place on the surface. This is especially the case if one is focused on the investigation of molecular adsorbates on single-crystal surfaces.

4.4.3 Scanning tunneling spectroscopy

One important extension of the STM method is the scanning tunneling spectroscopy. As was mentioned in Chapter 3, STS has been successfully implemented for the investigation of the electronic structure of atomically precise GNRs [20, 21, 26, 43, 45]. Since this technique is not used in the present thesis, it will be described very briefly. More detailed information can be found *e.g.* in Ref. [156].

The usual goal of STS experiments is to probe the local DOS distribution of the sample surface. Indeed, from Equation 4.22 it follows, that if the tip DOS is constant, then the dynamic tunneling conductance is proportional to the sample DOS:

$$\frac{dI_T}{dV_b} \propto \rho_s(E_F - eV_b). \tag{4.25}$$

Of course, this simple situation requires a special procedure to treat the tip. On the other hand, a reproducible sample surface is easier to prepare than a reproducible tip. If the behavior of the DOS as a function of energy is known

for a test sample, the STS can provide information on the tip DOS, which can then be used to obtain the DOS for the unknown sample.

In its simplest case, the STS spectrum can be recorded by placing an STM tip over a particular place at the sample. With the feedback off (the height of the tip is fixed), I_T is then measured while varying V_b, thus the I-V curve can be recorded. Taking Equation 4.25 into account, the slope of the I-V curve at each bias voltage ($\frac{dI_T}{dV_b}(V_b)$) contains information about the local DOS of the sample at $E_F - eV_b$. It should be noted, that one of the main problems in doing STS with an STM is that the tunneling probability typically exhibits a dependence on V_b. The character of this dependence is usually unknown. Therefore, the measured spectroscopic data need a normalization. One possible way is to measure the relative dynamic conductance ($g(V_b)$) instead of the absolute one:

$$g(V) = \frac{dI_T}{dV_b}\left(\frac{dI_T}{dV_b}\right)^{-1}_{V_b=0} \tag{4.26}$$

Thus, STS can provide spectroscopic information with atomic spatial resolution, which makes this method extremely useful for the investigation of nanosystems.

4.5 Density functional theory

The calculation of the physical properties of a system, such as a molecule or solid material requires the solution of the multi-electron Schrödinger equation, which cannot be done without approximations. Even within the one-electron Hartree-Fock model, eigenvalue equations are obtained for each of the one-dimensional wave functions and this set of equations have to be solved self-consistently. The major problem which limits the applicability of *ab initio* methods is that for the N particle system, the energy has to be minimized in the 3N space (without taking spin in the account). This makes calculations for any system even of moderate size an unbearably complicated task.

An alternative to the Hartree-Fock methods is the so-called Density Functional Theory (DFT) method. In 1964 Hohenberg and Kohn [160] proved that the electron density $n(\mathbf{r})$ uniquely specifies the total energy of an electron gas, even in the presence of an external potential. Therefore it is enough to know the ground state density to determine all observable quantities of the stationary quantum system. Thus, the wave-function description of the many-body problem in *ab initio* methods was reduced to the three-dimensional electron-density description in the DFT method.

The DFT-based methods have proved to be extreamly effective for the calculation of polyatomic quantum systems and are widely used nowadays. Walter Kohn received the Nobel Prize in Chemistry in 1998 “for his development of the density functional theory” [161].

Paper III includes results of DFT calculations for the DBBA molecule on Cu(110) surface by Dr. A. Lyalin in Global Research Center for Environment and Energy based on Nanomaterials Science (GREEN), National Institute for Materials Science (NIMS), Tsukuba, Japan.

4.6 Materials

4.6.1 Single crystal metal surfaces

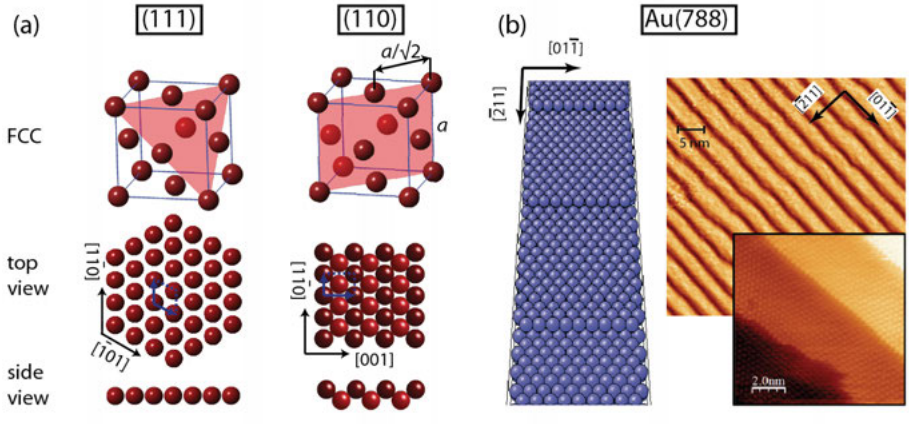

Figure 4.16. (a) The (111) and (110) planes for an FCC crystal and the corresponding surfaces (top and side view), where *a* is the lattice parameter. (b) Left: atomic structure of Au(788) surface, which is vicinal of Au(111). Right: STM images of clean Au(788) surface.

All single crystal metal substrates used in the present work, namely Au(111), Au(788), Ag(111), Cu(111) and Cu(110), were purchased from Surface Preparation Laboratory, Netherlands [162]. The crystal structure of Au, Ag and Cu is face-centered cubic (FCC). Figure 4.16 (a) shows an FCC crystal with (111) and (110) planes highlighted. It is clear, that the coordinations of the atoms in the (111) and (110) planes are different. The close-packed (111) surface is characterized by a 6-fold atomic arrangement, where each atom in the surface

Table 4.1. *Main crystallographic parameters for the surfaces used in this thesis.*

Parameter (Å)	Au(111)	Ag(111)	Cu(111)	Cu(110)
Lattice parameter (*a*)	4.08	4.09	3.61	3.61
Nearest neighbor distance	2.88	2.89	2.56	2.56
Interplane separation	2.35	2.36	2.09	2.56

plane has six neighbors, while for the (110) surface with a rectangular unit cell each atom has only two in-plane neighbors. As can be seen from the side view, the Cu(110) surface consists of close-packed atomic rows running along the $[1\bar{1}0]$ direction and the atoms of the underlying second layer are also, to some extent, exposed to the surface.

The relevant lattice parameters for each surface are given in Table 4.1. It should be noted, that while the clean Cu(111) surface has a 1×1 reconstruction (bulk-terminated), the clean Au(111) surface undergoes a $22 \times \sqrt{3}$ reconstruction, known as the "herringbone" [163].

The Au(788) surface, a vicinal to Au(111), consists of (111) terraces, 16 atom-rows wide (38 Å) and with monoatomic height (2.35 Å) (Figure 4.16 (b)). As on the Au(111) surface, the (111) terraces of Au(788) display the same $22 \times \sqrt{3}$ reconstruction. Therefore the Au(788) surface is nanoscopically patterned in two dimensions [164]: in the $\left[\bar{2}11\right]$ direction (*i.e.* perpendicular to the step edges), the step-terrace arrangement provides a structure of approximately 38 Å periodicity, whereas in the $\left[01\bar{1}\right]$ direction (*i.e.* parallel to the step edges) the herringbone reconstruction creates an anisotropic in-plane behaviour with a periodicity of about 72 Å. The Au(788) surface is relatively stable [164], and consequently has been used as a convenient template to grow regular arrays of GNRs [43, 44].

4.6.2 Molecules

Two kinds of molecules which are used in the experiments, DBBA (10,10'-dibromo-9,9'-bianthracene, $C_{28}H_{16}Br_2$) and BA (9,9'-bianthracene, $C_{28}H_{18}$), are schematically imaged in Figure 4.17. Both DBBA and BA have the lateral dimensions of 0.8×0.8 nm^2. The powders of DBBA and BA molecules (both 99% purity) were purchased from Angene Chemical company [165] and Langchem Inc. [166], respectively. Before being used in the experements the quality of the materials was double-checked using all avaliable techniques (XPS, NEXAFS, STM).

4.6.3 Sample preparation

In this section the common sample preparation procedure, used in our experiments, will be described. For more detailed information, regarding the experimental conditions in each particular case, please refer to the "Experimental section" within the corresponding article.

All the samples were prepared *in situ* under UHV conditions, ensuring the lack of impurities, which can affect on-surface processes. Like in any other surface science experiment, the on-surface transformations were studied on atomically clean single crystal surfaces. All crystals, preliminary degased by annealing in UHV up to $\approx 500^{\circ}$C, were further subjected to several cycles of

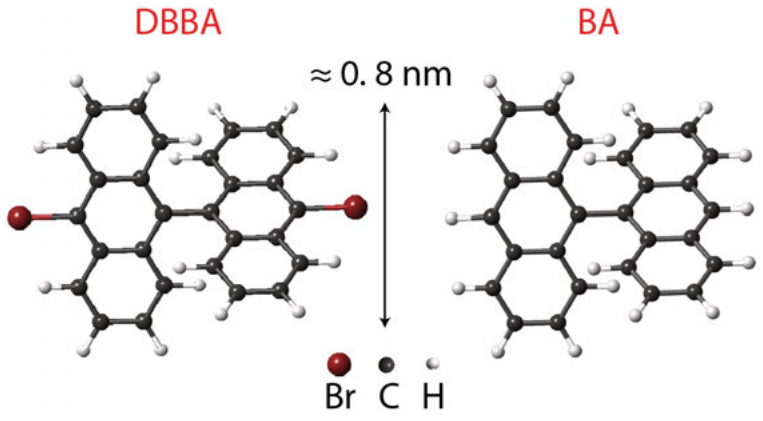

Figure 4.17. Ball-and-stick models of the two kinds of molecules used in the present thesis: DBBA ($C_{28}H_{16}Br_2$) and BA ($C_{28}H_{18}$).

bombardment with high energy (1 kV) Ar^+ ions for 20 - 40 min (to remove oxygen contamination and other remnants) and subsequent annealing at 500 - 600 °C to induce surface flattening. The temperature upon annealing was usually monitored both by a K-type thermocouple (ThC) and a Cyclops pyrometer (Land Instruments International). After the cleaning procedures the crystals were checked for structural perfectness and elemental cleanliness by Low-Energy Electron Diffraction (LEED) [167] and XPS.

In order to deposit organic molecules we sublimated them in UHV from a home-made Knudsen-cell type evaporator with a tantalum crucible (Figure 4.18). The tungsten filament is wound around the crucible in order to be able to heat the contents. The possibility to measure the temperature is provided by spot-welding of a K-type ThC contact to the wall of the crucible in a way that any contact between the ThC and the filament is avoided. Before deposition, the molecules were always outgassed for several hours at temperatures around 100°C and at a pressure of 1×10^{-7} mbar. The sublimation temperature of the molecules was about 170°C and thus low enough to prevent decomposition of the molecules in the crucible, which was double-checked experimentally. The pressure inside the vacuum chamber upon deposition of molecules was about 1×10^{-9} mbar (the base pressure was always around 1×10^{-10} mbar). The amount of deposited material was monitored by LEED and XPS, or directly with STM.

The STM system and the photoemission endstations provided the possibility to cool down the sample with liquid nitrogen. The design of the manipulator in the STM chamber and the XPS station at D1011 provided heating of the sample with a filament, located at the back side of the sample. For annealing to high temperatures (above 400°C) a high voltage was applied between the sample and the filament thus resulting in e-beam heating. Nevertheless,

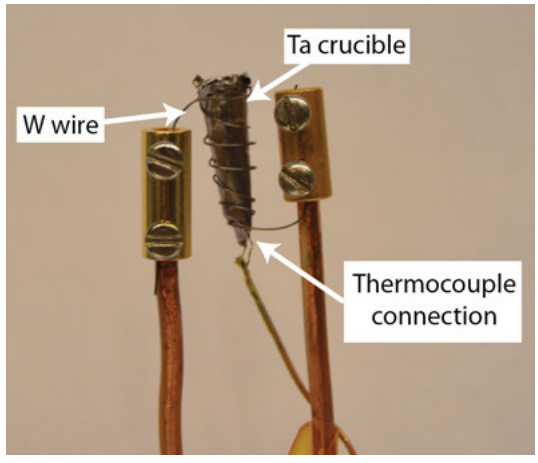

Figure 4.18. The design of the home-made molecular source.

one should be really careful when using direct e-beam heating for annealing such fusible metals. During experiments at I4 heating was achieved by passing current through the tungsten wires by which the sample was mounted on the special sample holder.

5. Summary of Results

An overview of the results included in the thesis is given in the following sections. Each part does not pretend to be comprehensive and just briefly summarizes the main outcome of the articles.

5.1 Effect of substrate activity on growth dynamics and structure of graphene nanoribbons

Using DBBA molecules as a precursor, in **Paper I** we have performed a comparative study of the 7-AGNRs growth on (111) gold and copper single crystal surfaces. We have shown, that GNRs can be grown on a Cu(111) substrate, but that the dynamics of the bottom-up process and the structure of the resulting ribbons are significantly affected by the interaction with the substrate.

As can be directly seen from the Br 3d XPS spectra (Figure 5.1 (a)), on more reactive Cu(111) a complete dehalogenation of DBBA molecules takes place already at RT, while on inert Au(111) the DBBA molecules completely lose Br only at 200°C. Based on the comprehensive spectroscopic study, including the investigation of the evolution of the angle-dependent C K-edge NEXAFS spectra and the C 1s XPS line we were able to monitor the process of graphene nanoribbon formation. As an example, Figure 5.1 (b) shows the intensity evolution of the individual components (C1, C2, C3), obtained from the results of a line-fitting analysis for the C 1s XPS line, as a function of sample annealing temperature. The line fitting was based on the structural models, suggested on the basis of NEXAFS and STM data. The colors of the spectral components correspond to the colors of the carbon atoms in the insets, illustrating different steps of GNRs formation on Au(111) and Cu(111).

It is clearly seen that the growth dynamics of the GNRs on Au(111) and Cu(111) differs significantly. On Au(111) the C1 ($C[C_2H]$) and C2 ($C[C_3]$) components evolve gradually up to 200°C, where debromination of DBBA molecules and formation of polymer chains occurs (the component C3 ($C[C_2Br]$) disappears), while just above this point the active process of cyclodehydrogenation starts and continues up to 300°C. Further annealing does not change the C 1s line profile significantly. Therefore, we assume that on Au(111) short GNRs can probably be found at 300°C, while annealing to 400°C leads to the formation of long flat 7-AGNRs.

On the contrary, on Cu(111) the precursors molecules lose bromine readily upon adsorption at RT (C3 component thus correspond to $C[C_2]$ sites). However, based on the intensity ratio of the C1 and C2 components it is plausible

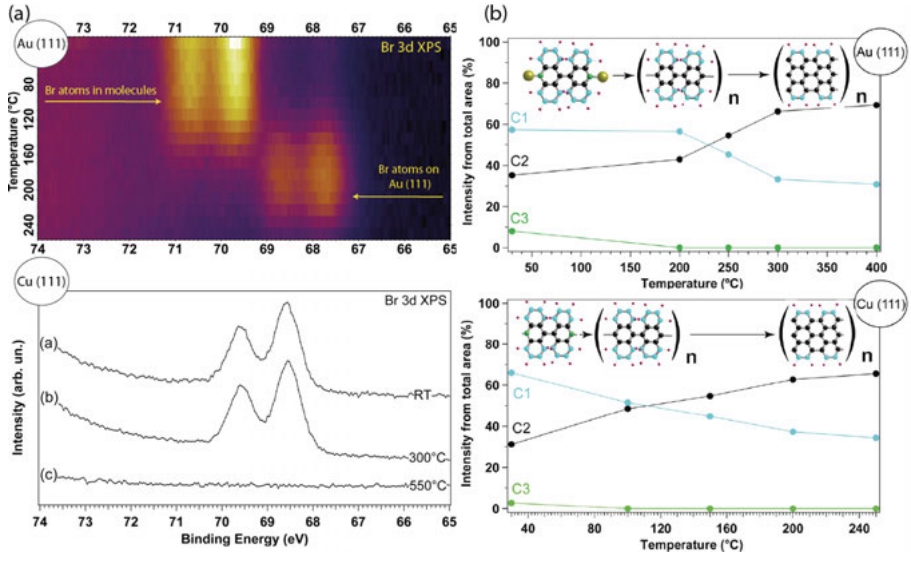

Figure 5.1. (a) Evolution of the Br 3d XPS spectrum of DBBA/Au(111) and DBBA/Cu(111) as a function of increasing sample temperature. (b) Intensity evolution of the individual components of the C 1s XPS signal (C1, C2, C3) measured as a function of annealing temperature upon GNR formation on Au(111) and Cu(111) substrates. See text for explanation.

to suggest that polymerization of debrominated molecular units do not occur at RT and that the dangling bonds formed after debromination are likely to interact with the copper substrate, resulting in the metastable organometallic structure. In turn, annealing to 100°C, is enough to brake the C-Cu bonds and overcome the diffusion barrier, which triggers the polymerization reaction between the molecular building blocks, resulting in the formation of polyanthracene chains. Moreover, unlike the situation on Au(111), on Cu(111) cyclodehydrogenation already occurs above 100°C and GNRs appear at 200 - 250°C.

Figure 5.2 (a) illustrates the STM images of the GNRs on Au(111) and Cu(111), formed after annealing to 400°C and 250°C, respectively. It can be seen, that on Cu(111) parallel rows, comprising 3 or 4 separate GNRs, can be observed. Their orientation is governed by a strong ribbon-substrate interaction, because the rows are oriented along six high-symmetry directions on Cu(111) with an angular separation of 30°, as can be nicely seen from the Fourier transform of the corresponding image (Figure 5.2 (a), inset). This is not the case on Au(111), where the orientation of the nanoribbons is random due to a weaker ribbon-substrate interaction. Moreover, as follows from Figure 5.2 (b), the stronger interaction with Cu(111) results in a significantly

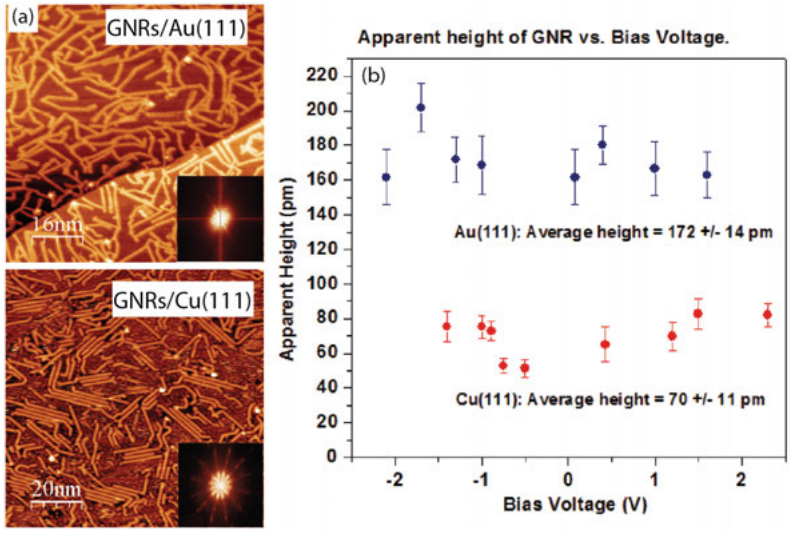

Figure 5.2. (a) STM images of GNRs/Au(111) obtained after 400°C anneal and GNRs/Cu(111) grown at 250°C. Insets show the Fourier transforms of the corresponding images. (b) Apparent height of the GNRs on Au(111) and Cu(111) obtained from STM images recorded at different V_b. Each data point is an average value for one STM image.

reduced apparent height of 70 $\pm$ 11 pm for the GNRs/Cu(111) in comparison with 172 $\pm$ 14 pm measured for the GNRs on Au(111).

It is worth mentioning that unlike GNRs on Au(111), on Cu(111) nanoribbons are formed in the presence of Br, which remains on the surface up to 500°C. Furthermore is not possible to remove Br from the surface by annealing without affecting the ribbons since GNRs/Cu(111) start to decompose at this temperature.

5.2 Graphene nanoribbons on Cu(111)

From **Paper I** we understood that the interaction with the active Cu(111) substrate plays a key role in the formation of GNRs/Cu(111). This observation led to the fact that different models have been proposed to explain the growth mechanism of the GNRs, resulting in contradictory suggestions about the structure of the resulting GNRs [168]. To address this question, in **Paper II** the growth mechanism of GNRs on Cu(111) was further investigated using STM.

Figure 5.3 illustrates the STM images, representing the successive stages leading to the formation of AGNRs on Cu(111). The long "chain-like" structures with the periodic bright protrusions on either side of the central axis of

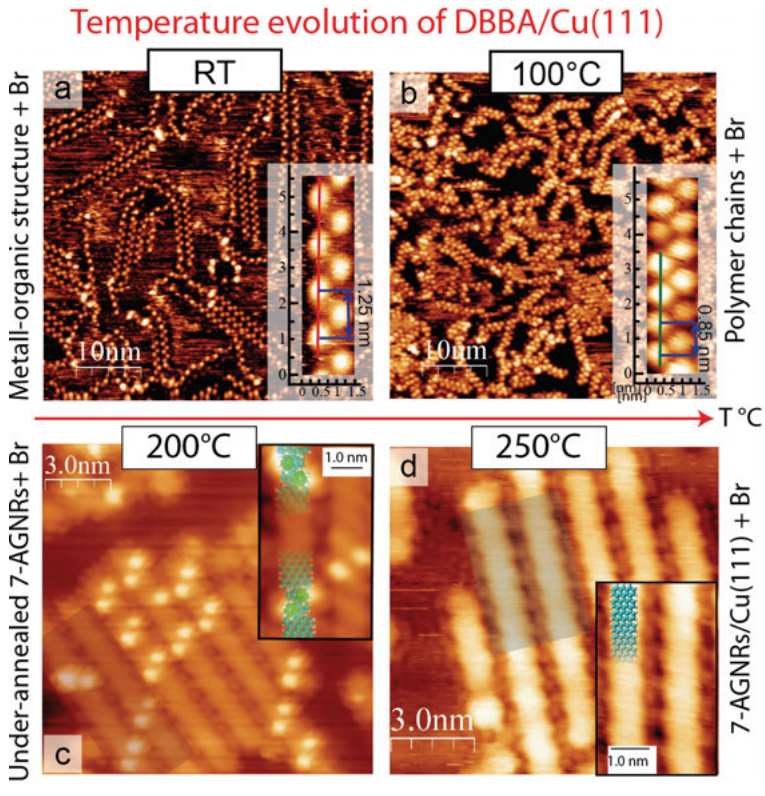

Figure 5.3. The series of STM images (a) - (b) - (c) - (d) shows successive stages leading to the formation of AGNRs on Cu(111). Insets: (a), (b) - High resolution images of a surface-confined DBBA chain at RT and the polymer chain at 100°C; (c), (d) - The enlarged images of two undeveloped and two completely flattened GNRs (highlighted with the transparent rectangle in the main image), respectively, with the superimposed ball-and-stick models. In the inset in (c) the aromatic rings pointing upwards are colored bright green.

the chain can be clearly seen at RT (Figure 5.3 a). However, the chain-like structures observed upon annealing at 100°C are different (Figure 5.3 b). As can be seen from the insets in Figure 5.3 (a,b), the periodicity along the DBBA chain at RT (1.25 nm) is significantly larger than that of the chains formed at 100°C (0.85 nm). The measured value of 0.85 nm for the period of the chains formed upon annealing at 100°C is in perfect agreement with the previously reported value measured for polymer chains on Au(111) [42] and is fully consistent with the structural model proposed in **Paper I** for 100°C anneal (*i.e.*, individual debrominated DBBA molecules linked by the covalent C-C bonds along the chain axis). Taking into account the results of the spectroscopic studies performed in **Paper I**, which indicate the possibility of the formation of a metastable surface-stabilized system at RT, it is proposed that Figure 5.3 (b) il-

lustrates organometallic surface-stabilized chains, consisting of debrominated DBBA molecules bonded at each end to the Cu substrate or to Cu adatoms. The period of the metalloorganic chain is 4 Å longer than that of the covalent one, which is consistent with C-Cu-C linkage between debrominated molecular units.

According to **Paper I**, upon further heating to 200°C the dehydrogenation inside the polyanthracene chains begins at temperatures of around 150°C, and by 250°C flat GNRs are formed. Figure 5.3 (c) corresponds to the intermediate stage of the GNR formation on Cu(111) after annealing at 200°C, where the dehydrogenation reaction is incomplete. Apparently, such "undeveloped" GNRs contain pairs of bright protrusions analogous to those observed in the polyanthracene chains at 100°C. As the annealing temperature was not high enough, the cyclodehydrogenation process inside the polyanthracene chain was not completed, leaving some of the anthracene units tilted with respect to the axis of the flat GNRs. This is schematically shown in the inset of Figure 5.3 (c). It is possible to obtain oppositely tilted pairs of anthracene units incorporated into the same GNR, or, sometimes, even individual (not paired) protrusions at places where dehydrogenation was completed only on one side of the precursor molecule.

Further annealing of the sample at 250°C leads to the disappearance of the bright protrusions and results in the formation of flat GNRs (Figure 5.3 d). The circular protrusions, which can be seen around GNRs are associated with Br adatoms which, as follows from spectroscopic data, are stably present on the Cu(111) surface up to 500°C. In principle, one can distinguish Br adatoms at the STM images after a 100°C anneal in the vicinity of polymer chains or even, rarely, at RT, where the Br atoms are too mobile to be clearly imaged. The formation of flat GNRs, most likely leads to the trapping of the Br adatoms by the potential landscape of the Cu(111) surface, modified by the presence of strongly bonded ribbons. On the basis of the analysis of the STM images, we have also compared the length distributions for GNRs/Au(111) and GNRs/Cu(111). Both distributions turn out to exhibit a Γ - like character centered at 17 nm for Au(111) and 12 nm for Cu(111) and having slightly bigger spread of sizes for GNRs/Au(111).

It should be noted that the growth mechanism revealed for GNRs/Cu(111), unlike the two-step process for GNRs on Au(111), includes an additional organometallic phase, preceding the formation of polymer chains. Nevertheless, this mechanism most likely results in the formation of 7-AGNRs/Cu(111), although the nature of the edge modulation observed for certain tunneling conditions in the STM images (see Figure 5.3 d) is still not entirely clear.

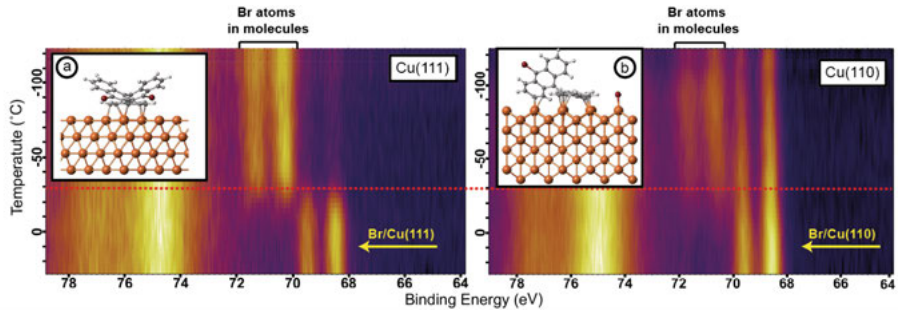

Figure 5.4. Intensity maps, showing the evolution of the Br 3d XPS spectrum of DBBA/Cu(111) and DBBA/Cu(110) as a function of increasing sample temperature. The insets show the calculated adsorption geometry of the DBBA molecule on the Cu(111) and Cu(110) surfaces below -30°C.

5.3 From graphene nanoribbon on Cu(111) to nanographene on Cu(110)

In **Paper III** we have focused on the comparison between on-surface processes taking place for DBBA on isotropic Cu(111) and on anisotropic Cu(110). While for the densely-packed Cu(111) surface, the reaction scheme investigated in **Paper I** and **Paper II** can be effectively implemented for the fabrication of atomically precise GNRs, on Cu(110) the bottom-up process carried out at the same conditions turns out to be significantly modified.

The striking difference in the on-surface reaction pathways manifests itself already at the initial stage of the process, *i.e.* in the debromination (Figure 5.4). The Br 3d XPS intensity maps reveal a significant increase in the substrate reactivity for the less densely-packed Cu(110) surface as compared to Cu(111): at -120°C the DBBA remains intact on Cu(111) and half-debrominated on Cu(110). Moreover, below -30°C the character of the debromination process on Cu(110) turns out to be significantly modified due to the "tilted" absorption geometry of the DBBA molecule. While one of the anthracene units in the DBBA forms bonds with low-coordinated Cu atoms in $[1\bar{1}0]$ atomic rows, another one points upwards, hence increasing the distance between its Br atom and the surface (see the insets, which show the corresponding absorption geometry calculated using DFT). Above -30°C DBBA occurs to be debrominated on both surfaces, nevertheless, on Cu(110) the strong interaction with the anisotropic surface hinders the formation of organometallic chains at RT. Instead of this, each individual debrominated molecule binds to the $[1\bar{1}0]$ rows with its dangling bonds and do not interact with the neighboring molecular units.

The evolution of the system has been tracked using NEXAFS, STM and XPS combined with DFT calculations. In particular, unlike the densely-packed Cu(111) surface, the Cu(110) is more active and anisotropic which in turn in-

fluences the adsorption energies, diffusion barriers and lateral interactions for molecular precursors. Unlike synthesis on Cu(111) where the Ullmann reaction between the debrominated DBBA fragments results in the formation of the polymer precursors for GNRs after 100°C anneal, on the Cu(110) surface the beginning of cyclodehydrogenation and high anisotropy of the potential relief blocks the covalent coupling of the molecular units and thus no polyanthracene chains are formed. As a result, instead of growth of GNRs, stepwise annealing of DBBA on Cu(110) to 250°C leads to the formation of nanographenes ($C_{28}H_8$ flat derivatives of DBBA) oriented with their armchair edge parallel to the $[1\bar{1}0]$ direction (see inset in Figure 5.5, right column). Each NG unit is strongly bonded to the underlying $[1\bar{1}0]$ copper rows causing a significant electron transfer from the substrate. Moreover, NG on Cu(110) can self-assemble into the highly ordered arrays, which can be interesting for the nanotechnological applications *e.g.* nanotemplating.

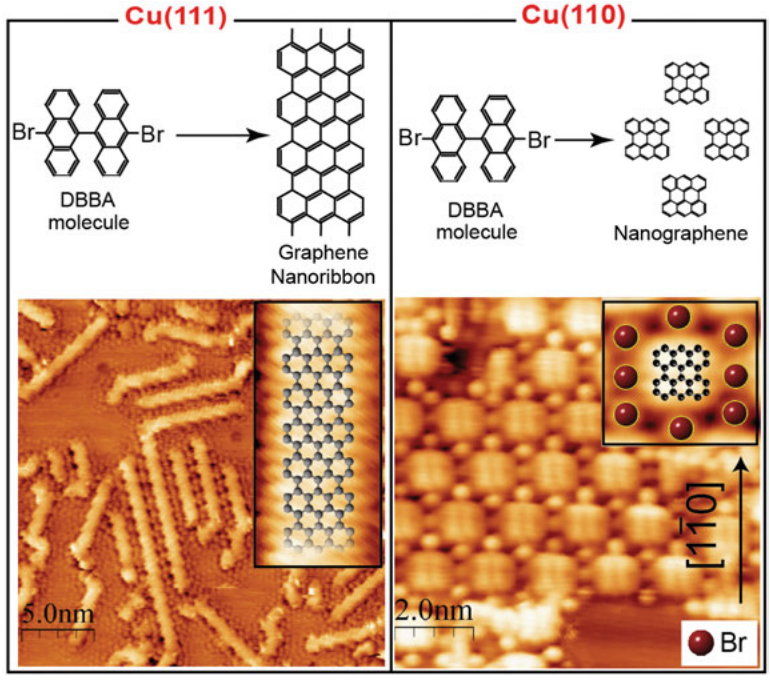

Figure 5.5. The outcome of the same preparation procedure performed for DBBA molecules on Cu(111) and Cu(110). While on Cu(111) GNRs are formed, on Cu(110) the quasi-0D nanographenes appear as a result of the on-surface reactions.

5.4 Insight into the role of the organometallic intermediates in the formation of GNRs on Ag(111)

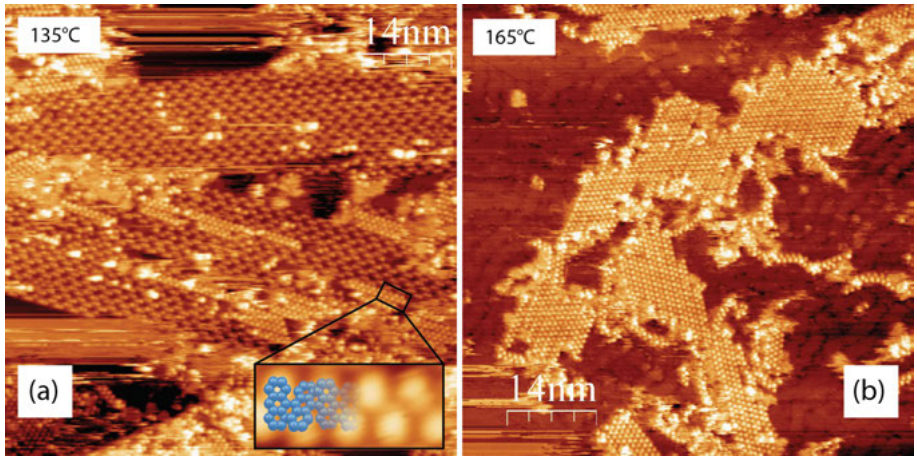

Figure 5.6. (a,b) STM images illustrating transformation of organometallic chains on Ag(111) into the polymer ones upon annealing. The inset in (a) is an enlarged region of the area indicated by the black rectangle containing one polymer chain, whose ball and stick model is superimposed on top.

In **Paper IV** we demonstrate that, unlike for the inert Au(111) substrate, but similar to the more active Cu(111) substrate, GNR's growth on the Ag(111) surface involves the formation of organometallic intermediates based on carbon-metal-carbon bonds. The GNR growth process was monitored by XPS and STM. Our STM studies show that the temperatures for the formation of organometallic chains depend on the substrate reactivity, being close to 120°C on Ag(111), while on Cu(111) the organometallic chains were previously observed at the room temperature. Being both composed of the debrominated DBBA molecular units interlinked through the metal atoms, the organometallic chains on Ag(111) appear to have different structure from the organometallic chains on Cu(111). Such an effect is associated with the difference in lattice constants of the Ag(111) and Cu(111) surfaces, which affects the orientation and adsorption configuration of the debrominated molecular units within the organometallic chains.

In order to determine the temperature threshold for the organometallic-to-covalent conversion and to demonstrate the very possibility of this transformation, the sample with organometallic chains was subsequently annealed with temperature intervals of 15 °C and characterized by STM at each annealing step. The first clear signs of covalent bonding between the DBBA units are visible already at 135 °C (Figure 5.6, a). Individual organometallic intermediates start to convert into visibly different dense chains characterized by the

periodic bright protrusions on either side of the central axis of the chain (inset in Figure 5.6, a). The new chains are characterised by a periodicity of 0.85 nm, which is fully consistent with the structural model of a polymer chain. Annealing at higher temperatures was demonstrated to promote further C-C coupling reaction. Being rarely visible at 135 °C, polymer chains appeared as frequently as organometallic chains at 150 °C, while annealing at 165 °C converted all organometallic bonds into covalent ones (Figure 5.6, b). It was shown that by further heating at 350 °C the polymer chains can be irreversibly converted into GNRs.

5.5 Charge injection in copper-intercalated graphene nanoribbons on Au(788)

The previous papers were mainly focused on the effect of the substrate on the growth mechanism and kinetics of on-surface transformations. In **Paper V** we suggest an elegant way to design GNR-metal interfaces *via* deposition of metal atoms on spatially aligned 7-AGNRs grown on the Au(788) surface, which allows to use ARPES technique to investigate changes in the electronic structure of GNRs induced by interaction with various metals. We report on the effect of Cu intercalation on the electronic structure of 7-AGNRs. We take advantage of combining ARPES, XPS, NEXAFS and STM in order to follow the intercalation process, and to investigate the structural and electronic properties of the 7-AGNRs/Cu/Au(788) system and its temperature evolution.

Due to the confinement of GNRs on the narrow (111) terraces of the Au(788) surface, the resulting ribbons are packed parallel to each other parallel to the step edges ($[01\bar{1}]$ direction), as was confirmed by the STM data (Figure 5.7 (a)). At the next stage one monolayer of copper has been deposited in UHV at RT on the 7-AGNRs/Au(788) system. As can be seen from Figure 5.7 (b) the GNRs are clearly visible after mild annealing at 80°C, which facilitates the intercalation. Importantly, most of the 7-AGNRs still preserve their orientation along the $[01\bar{1}]$ direction of gold, although the degree of alignment is reduced by the formation of an intercalated copper layer along the gold step edges, which causes lateral displacement of the nanoribbons. Since the long-range ribbon alignment in the Cu-intercalated system persisted, ARPES intensity maps have been measured for both 7-AGNRs/Au(788) and 7-AGNRs/Cu/Au(788), as shown in Figure 5.7 (c,d). ARPES reveals that the top of the first parabolic 7-AGNR band (shown by red arrow) is shifted by ΔE ~ 0.5 eV: from E_B = 0.9 eV to 1.4 eV. Such a pronounced downshift of the GNR-related bands indicates a significant electron injection into the ribbons from the underlying Cu layer.

The system was further investigated by XPS and NEXAFS. As was demonstrated by combining ARPES and NEXAFS data the effect of copper intercalation is restricted to n-doping only, without considerable modification of the

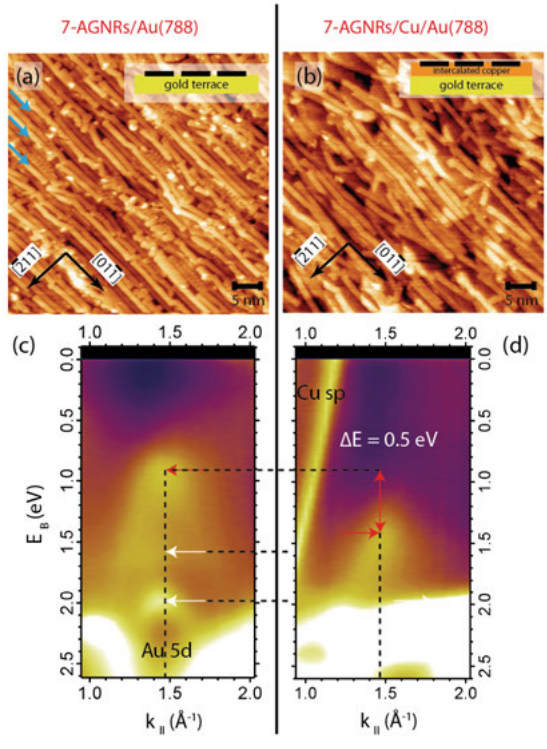

Figure 5.7. (a) STM image of aligned 7-AGNRs on Au(788). Cyan arrows point to three gold step edges. (b) STM image of copper-intercalated GNRs after 10 min anneal at 80°C. (c,d) ARPES momentum scans measured along $k_{\parallel}$ for 7-AGNRs/Au(788) and 7-AGNRs/Cu/Au(788), respectively.

band structure of the GNRs. From the XPS results it was shown that post-annealing of the 7-AGNRs/Cu/Au(788) system at 200°C activates the diffusion of copper into the gold and the formation of a Cu-rich surface gold layer. Alloying of the intercalated copper leads to a recovery of the initial position of GNR-related bands with respect to E_F, thus proving tunability of the induced n-doping.

5.6 Doping of 7-AGNRs induced by lithium deposition: metallization of GNRs

As follows from **Paper V** interaction of GNR with metal can cause significant electron injection in GNRs. In this respect it was quite interesting to see how interaction with an active alkali metal could influence the properties of GNRs. Therefore **Paper VI** is focused on the effect of interaction with lithium on the electronic structure of 7-AGNR prepared on the Au(788) surface.

The Li is a much more effective electron dopant than Cu and, as was confirmed by ARPES measurements, *via* lithium doping 7-AGNRs can be effectively transformed from a semiconductor into a metal due to the partial filling of the conduction band. The bandgap of 2.1 eV for Li-doped 7-AGNRs was directly measured from the ARPES data, and is 0.3 eV smaller than the bandgap measured by STS method from the intact 7-AGNRs/Au(788). More interestingly, as was estimated from the curvature of the electron bands, after doping the effective mass of the conduction band carriers is significantly increased.

The system was additionally investigated by XPS, NEXAFS and Raman spectroscopy. The latter allowed to observe a renormalization of the GNR's phonon spectrum upon doping. While the origins of the observed effects are not clear yet, our results demonstrate that 1D GNRs react to electron doping quite differently from 2D graphene.

6. Outlook

Without doubt researchers in different areas, including surface science, chemistry and nanotechnology still have a plenty of work to do before the potential of GNRs and other nanostructured materials will be at least partially realized in real devices. Nevertheless, each scientific work on this subject is a small but nonetheless important investment in our common knowledge about those complicated but fascinating objects.

The results presented in this thesis contribute to the understanding of the controllable preparation of GNRs from molecular precursors. It is shown that both substrate composition and structure have a critical impact on the on-surface bottom-up synthesis process. In addition we proposed an original conception for investigation of GNR-metal interfaces and demonstrated that contact with metal may significantly affect the properties of GNR. Our research can be logically extended to the exploration of the possibilities for further modification of the electronic properties of GNRs *via* chemical functionalization with atoms or functional groups. Altogether, this can have a good practical outcome for those who design GNR-based electronics.

While our work was focused on AGNRs, ZGNRs, thanks to their unique edge states, represent no less or perhaps even more interest for certain electronic applications, especially spintronics. The recent successful bottom-up synthesis of atomically precise ZGNRs opens extensive opportunities and challenges for the analysis of their physical properties (for example, their band structure, magnetism and charge/spin transport).

It should be noted that most of the experiments so far are limited by the use of a metallic substrate. Further processing is thus required to transfer the synthesized structures onto device-ready semiconductor surfaces which enable back-gating and minimize leak currents as well as GNR-substrate interaction effects. Recent experiments performed by local probe techniques indicate that the synthesis of covalently bonded nanostructures on bulk insulator surfaces, transition metal oxides, and also passivated semiconductor may be feasible. It opens the door for investigation of bottom-up synthesized GNRs and other nanostructured materials on device-ready substrates.

7. Populärvetenskaplig sammanfattning

Gränsen mellan mikroteknologi och nanoteknologi brukar ofta sättas till etthundra nanometer (10^{-7} m), vilket motsvarar ungefär en tusendel av tjockleken hos ett hårstrå. Halvledarindustrin passerade denna gräns ungefär vid millenieskiftet i sin strävan att göra allt mindre komponenter. På mindre än 50 år har denna industri genomgått en oerhörd förändring: från diskreta transistorer som var centimeterstora till "mikrochips" med milliontals transistorer där storleken för de enskilda transistorerna är betydligt mindre än en mikrometer. När förra millenniet gick mot sitt slut började man tillverka vad man istället skulle kunna kalla "nanochips". Den exponentiella minskningen av storleken hos elektronikkomponenterna beskrevs år 1965 av ingenjören och affärsmannen Gordon E. Moore. Enligt Moore's lag tar det mellan ett och två år att fördubbla antalet komponenter som man kan få in på en viss yta. Sedan 1965 har utvecklingen faktiskt följt Moore's lag. ända sedan 1970-talet har man diskuterat om och när naturliga barriärer skulle bryta denna utveckling, men vetenskapsmännen och ingenjörerna har hela tiden funnit nya tekniska lösningar.

Idag ser man nya vägar att fortsätta tillverkning av allt mindre komponenter genom att använda nya nanostrukturerade material med väldefinierade egenskaper. För att kunna kontrollera nanomaterialens egenskaper måste man kunna kontrollera den kemiska strukturen och man talar om designade material. Det har visat sig att man kan bygga sådana strukturer med atomär precision. Man utnyttjar molekylära byggstenar som kan byggas ihop så att varje atom i molekylen kommer på en förutbestämd plats. Man kan på detta sätt styra materialens egenskaper. Man kan beskriva detta som ett molekylärt LEGO-byggande. Nya strukturer byggs upp från de molekylära byggstenarna *via* successiva kemiska reaktioner på atomärt rena ytor, det vill säga ytor som är fria från föroreningar ända ner på atomnivån. Detta sätt att tillverka specifika nanostrukturer kan öppna nya vägar att skapa kvantdatorer, molekylära maskiner och andra komponenter. Det öppnar nya vägar för tekniska framsteg i den framväxande nano-eran.

Det är en mycket stor utmaning att kunna kontrollera kemiska reaktioner på ytor med atomär precision. Först och främst krävs Ultra-Hög Vakuum (UHV) i experimentkammaren för att undvika att främmande atomer och molekyler förorenar ytorna. Detta kräver avancerade pumpar och vakuumkammare tillverkade av speciella typer av material. Dessutom behöver man utnyttja ett antal experimentella tekniker för att studera vad som händer på ytorna.

Fotoelektronspektoskopi (XPS) och Röntgenabsorptionsspektroskopi (XAS) är två kraftfulla metoder som bygger på att man bestrålar provet med

Röntgenstrålning. Teknikerna bygger på att Röntgenstrålningen, när den absorberas av en atom i materialet, kan lyfta upp en elektron från en av atomens besatta nivåer till en högre obesatt nivå. I XAS lyfts elektronen från en inre nivå till en specifik nivå och när detta äger rum ser man att röntgenstrålningen absorberas i högre utsträckning vid denna Röntgenenergi. I XPS får elektronen däremot en så hög energi att den kan lämna provet. Genom att mäta dess energi i en elektronspektrometer kan man dra slutsatser om atomernas energinivåer i materialet. Genom dessa tekniker kan man få information om materialets sammansättning och i vilken kemisk omgivning de olika atomerna befinner sig.

En annan metod i forskarens verktygslåda är sveptunnelmikroskopin (STM). Tekniken bygger på ett fenomen där elektroner kan hoppa över från ett material till ett annat ("tunnla") om gapet mellan dessa är tillräckligt litet. Sannolikheten för att elektronen skall tunnla avtar mycket snabbt med avståndet mellan materialen. I STM-tekniken utnyttjar man denna effekt för att undersöka ett materials ytstruktur på en atomär skala. Man för en spets alldeles över ett prov och mäter hur stark tunnelströmmen är. Spetsen kan göras så fin att den slutar med en enda atom. Med denna teknik kan man således skapa en bild av materialet med atomär upplösning.

Med hjälp av dessa tekniker kan forskarna studera såväl strukturen som det kemiska tillståndet hos de olika systemen under byggandet av de nanostrukturerade materialen.

Denna avhandling är inriktad mot en ny klass av nanostrukturer - nanotrådar (eller nanoband) av grafén, här kallade GNR (Graphene Nano Ribbons). Grafén är ett material bestående av enbart kolatomer och som bara är ett atomlager tjockt. Grafén har mycket intressanta egenskaper, inte minst elektroniska. GNR är smala band av grafén, kanske bara tio kolatomer breda. Genom att på detta sätt kontrollerat begränsa utsträckningen hos grafénstrukturerna kan man styra de elektroniska egenskaperna. Detta kan var en möjlig väg att skapa nya högpresterande elektronikkomponenter. Dessa strukturer måste tillverkas genom kontrollerad syntes på ytor. Betydelsen av ytans (substratets) egenskaper för denna syntes och för nanostrukturernas egenskaper kan inte överskattas. Målet med detta arbete har därför varit att med hjälp av Röntgenbaserade spektroskopier och STM undersöka substratets inverkan på syntesen och de elektroniska egenskaperna hos de studerade nanostrukturerade materialen.

8. Acknowledgements

To some extent the presented thesis summarizes four years of my life. It was sometimes difficult, but always interesting time during which I met so many new people, colleagues and friends, who, without doubt, contributed to this work in many different ways. In this brief chapter I would like to thank all of you.

First of all I would like to express my deep gratitude to Prof. Nils Mårtensson, Prof. Olof (Charlie) Karis and Dr. Alexei Preobrajenski, my research supervisors. Nils and Charlie, thank you for being supportive and helping out with various problem despite your tight schedule. Nils, thank you for enthusiastic encouragement and constructive suggestions, which I am very grateful for.

Alexei, thank you for your patient guidance during the planning and development of this research work. Thank you for teaching me of all aspects of how to set-up and perform experiments. Your continuous support, motivation, and immense knowledge helped me in all the time of my PhD both at work and in life.

I would like to extend my thanks to all personnel of MAX IV, especially to my labmates - Dr. Nikolay Vinogradov and Dr. Alexander Generalov, for the stimulating discussions, for the sleepless nights we were working together during beamtimes, and for all the fun we have had in the last four years. Nikolay, thank you for your guidance during my first experiments and your assistance with adaptation to the realities of life in Sweden. I wish to thank Dr. Karsten Handrup, Dr. Noelle Walsh, Dr. Jacek Osiecki, Dr. Justin Wells, Dr. Balasubramanian Thiagarajan (Balu), Dr. Johan Adell, Dr. Mats Leandersson, Dr. Karina Thånell (Schulte) and Dr. Alex Zakharov for helping me. Many thanks also goes to Dr. Rainer Pärna, Dr. Katerina Medjanik, Dr. Natallia Torapava, Dr. Johan Unge - for their constant support and a good company!

In the beginning of my PhD project I performed STM measurements at the Division of Synchrotron Light Radiation in Lund University. I am very grateful to Prof. Edvin Lundgren, Prof. Anders Mikkelsen, Dr. Jan Knudsen, Dr. Elin Grånäs, Dr. Natalia Martin and Alif Arman for their help.

I was also tightly involved in collaboration with researchers from Dublin - Prof. Tony Cafolla, Dr. Thomas Carpy and Dr. John P Cunniffe (Dublin City University), and Prof. Cormac McGuinness (Trinity College Dublin). Tony, Tom, John, thank you for hosting me in Dublin and teaching me the subtleties of the STM technique. Tony and Cormac, I really grateful to both of you for advice and assistance. It was really nice to be the member of your team!

My sincere thanks also goes to Prof. Alexander Vinogradov from Saint-Petersburg State University, whose guidance helped me in all the time of my studies in Sweden. I appreciate help which I got from the students of SPbSU - Gleb Svirskiy and Elena Zagrebina, during beamtimes at D1011.

Since my position was located in Lund, I was not an often visitor in Uppsala. Nevertheless, during the last year of my studies I was given an opportunity to join UBjL and was introduced to the HELIOS lab. I would therefore like to thank Prof. Svante Svensson, Dr. Ruslan Ovsyannikov, Dr. Torsten Leitner, Prof. Håkan Rensmo, Prof. Anders Sandell, Dr. Johan Söderström, Dr. Joachim Terschlüsen, Dr. Robert Stefanuik, Dr. Valeria Lanzilotto, Dr. Ute Cappel, Dr. Yasmine Sassa, and others. I hope our future work will be rewarding in any sense.

Of course I cannot ignore all collaborators and co-authors - thank you for working with me on papers, projects and so on. I would also like to thank the administrative and technical staff at MAX IV and Uppsala University.

For enabling me to complete my education I would like to acknowledge funding by the citizens of Sweden and European Union through the Swedish Research Council, the Swedish Energy Agency (STEM), and the European Research Council (ERC).

Last but not the least, I would like to thank my family. Thank you for supporting me spiritually throughout writing this thesis and my life in general.

References

[1] M. D Hill, N.P. Jouppi, and G.S. Sohi. *Readings in Computer Architecture*. Academic Press, 2000.

[2] B. Trauzetteel et al. Spin qubits in graphene quantum dots. *Nature Phys.*, 3:192–196, 2007.

[3] G. Brumfiel. Quantum leaps. *Nature*, 491:322–324, 2012.

[4] R. Barends et al. Superconducting quantum circuits at the surface code threshold for fault tolerance. *Nature*, 508:500–503, 2014.

[5] A. Brenneis et al. Ultrafast electronic readout of diamond nitrogen-vacancy centres coupled to graphene. *Nature Nanotech.*, 10:135–139, 2015.

[6] C. Joachim, J. Gimzewski, and A. Aviram. Electronics using hybrid-molecular and mono-molecular devices. *Nature*, 408:541–548, 2000.

[7] A. Nitzan and M. A. Ratner. Electron transport in molecular wire junctions. *Science*, 300:1384–1389, 2003.

[8] J. Fiurášek et al. Intramolecular hamiltonian logic gates. *Physica E*, 24:161–172, 2004.

[9] I. Diez-Perez et al. Gate-controlled electron transport in coronenes as a bottom-up approach towards graphene transistors. *Nat.Commun.*, 1:31, 2010.

[10] F. Schwarz et al. High-conductive organometallic molecular wires with delocalized electron systems strongly coupled to metal electrodes. *Nano Lett.*, 14:5932–5940, 2014.

[11] J. V. Barth et al. Supramolecular architectures and nanostructures at metal surfaces. *Appl. Phys. A*, 76:645–652, 2003.

[12] N. Lin et al. Surface-assisted coordination chemistry and self-assembly. *Dalton Trans.*, pages 2794–2800, 2006.

[13] S. De Feyter et al. Molecular and supramolecular networks on surfaces: from two-dimensional crystal engineering to reactivity. *Angew. Chem. Int. Ed.*, 48:7298–7332, 2009.

[14] D. Liu et al. Using azobenzene-embedded self-assembled monolayers to photochemically control cell adhesion reversibly. *Angew. Chem. Int. Ed.*, 48:4406–4408, 2009.

[15] R. Klajn. Immobilized azobenzenes for the construction of photoresponsive materials. *Pure Appl. Chem.*, 82:2247–2279, 2010.

[16] F. Klappenberger. Two-dimensional functional molecular nanoarchitectures - complementary investigations with scanning tunneling microscopy and X-ray spectroscopy. *Progr. Surf. Sci.*, 89:1–55, 2014.

[17] M. El Garah et al. Covalently bonded networks through surface-confined polymerization. *Surf. Sci.*, 613:6–14, 2013.

[18] K. S. Novoselov. A roadmap for graphene. *Nature*, 490:192–200, 2012.

[19] F. Schwierz. Graphene transistors. *Nat Nanotechnol.*, 5:487–496, 2010.

[20] J. Cai et al. Graphene nanoribbon heterojunctions. *Nature Nanotech.*, 9:896–900, 2014.

[21] Chen Y.-H. et al. Molecular bandgap engineering of bottom-up synthesized graphene nanoribbon heterojunctions. *Nat. Nanotechnol.*, 10:156–160, 2015.
[22] Z. Chen et al. Graphene nano-ribbon electronics. *Physica E*, 40:228–232, 2007.
[23] M. Han et al. Energy band-gap engineering of graphene nanoribbons. *Phys. Rev. Lett.*, 98:206805, 2007.
[24] M. Koch et al. Voltage-dependent conductance of a single graphene nanoribbon. *Nature Nanotechnol.*, 7:713–717, 2012.
[25] J. Van der Lit et al. Suppression of electron-vibron coupling in graphene nanoribbons contacted via a single atom. *Nature Commun.*, 4:2023, 2013.
[26] Y.-C. Chen et al. Tuning the band gap of graphene nanoribbons synthesized from molecular precursors. *ACS Nano*, 7:6123–6128, 2013.
[27] C. Bronner et al. Aligning the band gap of graphene nanoribbons by monomer doping. *Angew. Chem. Int. Ed.*, 52:4422–4425, 2013.
[28] P. B. Bennett et al. Bottom-up graphene nanoribbon field-effect transistors. *Appl. Phys. Lett.*, 103:253114, 2013.
[29] K. Wakabayashi et al. Electronic and magnetic properties of nanographite ribbons. *Phys. Rev. B*, 59:8271–8282, 1999.
[30] Y.-W. Son, M. Cohen, and S. G. Louie. Half-metallic graphene nanoribbons. *Nature*, 444:347–349, 2006.
[31] M. Ezawa. Peculiar width dependence of the electronic properties of carbon nanoribbons. *Phys. Rev. B*, 73:045432, 2006.
[32] V. Barone, O. Hod, and G. E. Scuseria. Electronic structure and stability of semiconducting graphene nanoribbons. *Nano Lett.*, 6:2748–2754, 2006.
[33] L. Yang et al. Quasiparticle energies and band gaps in graphene nanoribbons. *Phys. Rev. Lett.*, 99:186801, 2007.
[34] P. Shemella et al. Energy gaps in zero-dimensional graphene nanoribbons. *Appl. Phys. Lett.*, 91:042101, 2007.
[35] J. Bai and Huang. Yu. Fabrication and electrical properties of graphene nanoribbons. *Mater. Sci. Eng. R*, 70:341–353, 2010.
[36] L T. Nguyen et al. Electronic band structures of graphene nanoribbons with self-passivating edge reconstructions. *J. Phys.: Condens. Matter*, 23:295503, 2011.
[37] P. Wagner et al. Band gap engineering via edge-functionalization of graphene nanoribbons. *J. Phys. Chem. C*, 117:26790–26796, 2013.
[38] O. V. Yazyev. A guide to the design of electronic properties of graphene nanoribbons. *Acc. Chem. Res.*, 46:2319–2328, 2013.
[39] Y. Li et al. Electronic and magnetic properties of zigzag graphene nanoribbons on the (111) surface of Cu, Ag, and Au. *Phys. Pev. Lett.*, 110:216804, 2013.
[40] F. Cervantes-Sodi et al. Edge-functionalized and substitutionally doped graphene nanoribbons: Electronic and spin properties. *Phys. Rev. B*, 77:165427, 2008.
[41] H. Terrones et al. The role of defects and doping in 2D graphene sheets and 1d nanoribbons. *Rep. Prog. Phys.*, 75:062501, 2012.
[42] J. Cai et al. Atomically precise bottom-up fabrication of graphene nanoribbons. *Nature*, 466:470–473, 2010.

[43] P. Ruffieux et al. Electronic structure of atomically precise graphene nanoribbons. *ASC Nano*, 6:6930–6935, 2012.
[44] S. Linden et al. Electronic structure of spatially aligned graphene nanoribbons on Au(788). *Phys. Rev. Lett.*, 108:216801, 2012.
[45] H. Huang et al. Spatially resolved electronic structures of atomically precise armchair graphene nanoribbons. *Sci. Rep.*, 2, 2012.
[46] L. Talirz et al. Termini of bottom-up fabricated graphene nanoribbons. *J. Am. Chem. Soc.*, 135:2060–2063, 2013.
[47] C. Bronner et al. Electronic structure changes during the surface-assisted formation of a graphene nanoribbon. *J. Chem. Phys.*, 140:024701, 2014.
[48] S. Peljhan and A. Kokalj. DFT study of gas-phase adsorption of betzotriazole on Cu(111), Cu(100) and Cu(110), and low coordinated defects thereon. *Phys. Chem. Chem. Phys.*, 13:20408–20417, 2011.
[49] M Bieri et al. Two-dimensional polymer formation on surfaces: Insight into the roles of precursor mobility and reactivity. *J. Am. Chem. Soc.*, 132:16669–166676, 2010.
[50] M. Kolmer et al. Polymerization of polyanthrylene on a titanium dioxide (011)-(2×1) surface. *Angew. Chem. Int. Ed.*, 52:10300–10303, 2013.
[51] R. Gutzler et al. Ullmann-type coupling of brominated tetrathientoanthracene on copper ans silver. *Nanoscale*, 6:2660–2668, 2014.
[52] L. Massimi et al. Surface-assisted reactions toward formation of graphene nanoribbons on Au(110) surface. *J. Phys. Chem. C*, 119:2427–2437, 2014.
[53] Z.-X. Hu, H. Lan, and W. Ji. Role of the dispersion force in modeling the interfacial properties of molecule-metal interfaces: adsorption of thiophene on copper surfaces. *Sci. Rep.*, 4:5036, 2014.
[54] J. A. Lipton-Duffin et al. Synthesis of polyphenylene molecular wires by surface-confined polymerization. *Small*, 5:592–297, 2009.
[55] J. Eichhorn et al. On-surface Ullmann coupling: the influence of kinetic reaction parameters on the morphology and quality of covalent networks. *ACS Nano*, 8:7880–7889, 2014.
[56] Q. Fan et al. Surface-assisted formation, assembly, and dynamics of planar organometallic macrocycles and zigzag shaped polymer chains with C-Cu-C bonds. *ACS Nano*, 8:709–718, 2014.
[57] Q. Fan et al. Covalent, organometallic and halogen-bonded nanomeshes from tetrabromo-terphenyl by surafase-assisted synthesis on Cu(111). *J. Phys. Chem. C*, 118:13018–13025, 2014.
[58] M. Di Giovannantonio et al. Insight into organometallic intermidiate and its evolution to covalent binding in surface-confined Ullmann polymerization. *ACS Nano*, 7:8190–8198, 2013.
[59] E. A. Lewis et al. Atomic-scale insight into the formation, mobility and reaction of Ullmann coupling intermediates. *Chem. Commun.*, 50:1006–1008, 2014.
[60] S. A. Krasnikov et al. Formation of extended covalently bonded Ni porphyrin networks on the Au(111) surface. *Nano. Res.*, 4:376–384, 2011.
[61] A. Basagni et al. Molecules-oligomers-nanowires-graphene nanoribbons: A bottom-up stepwise on-surface covalent synthesis preserving long-range order. *J. Am. Chem. Soc.*, 137:1802–1808, 2015.

[62] D. Heim et al. Self-assembly of flexible one-dimensional coordination polymers on metal surfaces. *J. Am. Chem. Soc.*, 132:6783–6790, 2010.
[63] J. Park et al. Interchain interactions mediated by Br adsorbates in arrays of metal-organic hybrid chains on Ag(111). *J. Phys. Chem. C*, 115:14834–14838, 2011.
[64] A. Saywell et al. Manipulating the conformation of single organometallic chains on Au(111). *J. Phys. Chem. C*, 118:1719–1728, 2014.
[65] M. Treier et al. Surface-assisted cyclodehydrogenation provides a synthetic route towards easily processable and chemically tailored nanographenes. *Nature Chem*, 3:61–67, 2010.
[66] A. L. Pinardi et al. Tailored formation of N-doped nanoarchitectures by diffusion-controlled on-surface (cyclo)-dehydrogenation of heteroaromatics. *ACS Nano*, 7:3676–3684, 2013.
[67] S. Haq et al. Versatile bottom-up construction of diverse macromolecules on surface observed by scanning tunneling microscopy. *ACS Nano*, 8:8856–8870, 2014.
[68] D. Zhong et al. Linear alkane polymerization on gold surface. *Science*, 334:213–216, 2011.
[69] L. Talirz et al. On-surface synthesis of atomically precise graphene nanoribbons. *Adv. Mater.*, 2016.
[70] G. Vasseur et al. Quasi one-dimensional band dispersion and surface metallization in long-range ordered polymeric wires. *Nature Commun.*, 7:10235, 2016.
[71] S. Wang et al. Resolving band-structure evolution and defect-induced states of single conjugated oligomers by scanning tunneling microscopy and tight-binding calculations. *Phys. Rev. Lett*, 106:206803, 2011.
[72] G. Giovannetti et al. Doping graphene with metal contacts. *Phys. Rev. Lett*, 101:026803, 2008.
[73] B. Huard et al. Evidence of the role of contacts on the observed electron-hole asymmetry in graphene. *Phys. Rev. B*, 78:121402, 2008.
[74] A. Varykhalov et al. Effect of noble-metal contacts on doping and band gap of graphene. *Phys. Rev. B*, 82:121101, 2010.
[75] F. Xia et al. The origins and limits of metal-graphene junction resistance. *Nat. Nanotechnol.*, 6:179–184, 2011.
[76] C. Archambault et al. States modulation in graphene nanoribbons through metal contacts. *ACS Nano*, 7:5414–5420, 2013.
[77] D. Mencarelli et al. Analysis of the metal work function dependence of charge transfer in contacted graphene nanoribbons. *Nanomater. Nanotechnol.*, 2:12:2012, 2012.
[78] D. Haberer et al. Anisotropic eliashberg function and electron-phonon coupling in doped graphene. *Phys. Rev. B*, 88:081401, 2013.
[79] B. M. Ludbrook et al. Evidence for superconductivity in li-decorated monolayer graphene. *Proceedings of the National Academy of Sciences*, 112:11795–11799, 2015.
[80] B. Genorio and A. Znidarsic. Functionalization of graphene nanoribbons. *J. Phys. D: Appl. Phys.*, 47:094012, 2014.

[81] G. D. Nguyen et al. Bottom-up synthesis of N = 13 sulfur-doped graphene nanoribbons. *J. Phys. Chem. C*, 120:2684–2687, 2016.
[82] Q. Zhang, X. amd Zeng and C. Wang. On-surface single molecule synthesis chemistry: a promising bottom-up approach towards functional surfaces. *Nanoscale*, 5:8269–8287, 2013.
[83] A. Shchyrba et al. Covalent assembly of two-dimensional molecular "sponge" on Cu(111) surface: confined electronic surface states in open and closed pores. *Chem. Commun.*, 50:7628–7631, 2014.
[84] N. Koch. *Supramolecular Materials for Opto-Electronics*. The Royal Society of Chemistry, 1st edition, 2015.
[85] A. Gourdon. On-surface covalent coupling in ultrahigh vacuum. *Angew. Chem. Int. Ed.*, 47:1950–6953, 2008.
[86] Y.-Q. Zhang et al. Homo-coupling of terminal alkynes an a noble metal surface. *Nat. Commun.*, 3:1286, 2012.
[87] J. Björk et al. Untraveling the mechanism of the covalent coupling between terminal alkynes on a noble metal. *J. Phys. Chem. C*, 118:3181–3187, 2014.
[88] Q. Sun et al. Dehydrogenative homocoupling of terminal alkenes on copper surfaces: a route to dienes. *Angew. Chem. Int. Ed.*, 54:1–5, 2015.
[89] F. Ullmann and J. Bielecki. Über synthesen in der biphenylreihe. *Ber. Dtsch. Chem. Ges.*, 34:2174–2185, 1901.
[90] M. Xi and B. E. Bent. Mechanics of Ullmann coupling reaction in adsorbed monolayers. *J. Am. Chem. Soc.*, 115:7426–7433, 1993.
[91] J. Eichhorn et al. On-surface Ullmann polymerization via intermidiate organometallic networks on Ag(111). *Chem. Commun.*, 50:7680–7682, 2014.
[92] L. Grill et al. Nano-architectures by covalent assembly of molecular building blocks. *Nature Nanotech.*, 2:687–691, 2007.
[93] G. Franc and A. Gourdon. Covalent networks through on-surface chemistry in ultra-high vacuum: state-of-the-art and recent developments. *Phys. Chem. Chem. Phys.*, 13:14283–14292, 2011.
[94] L. Lefferentz et al. Controlling on-surface polymerization by hierarchical and substrate-directed growth. *Nature Chem.*, 4:215–220, 2012.
[95] M. M. Blake et al. Identifying reactive intermediates in the Ullmann coupling reaction by scanning tunneling microscopy and spectroscopy. *J. Phys. Chem. A*, 113:13167–13172, 2009.
[96] M. Kittelmann et al. Sequential and site-specific on-surface synthesis on a bulk insulator. *ACS Nano*, 7:5614–5620, 2013.
[97] J. Björk et al. Mechanisms of halogen-based covalent self-assembly on metal surfaces. *J. Am. Chem. Soc.*, 135:5768–5775, 2013.
[98] P. Henderson et al. Synthesis of functionalized triphenylenes and dibenzopyrenes. precursor molecules for polymeric discotic liquid crystals. *Liq. Cryst.*, 18:191, 1995.
[99] Weiss. K et al. Template-mediated synthesis of polyciclic aromatic hydrocarbons: cyclodehydrogenation and planarization of hexaphenylbenzene derivative on copper surface. *Angew. Chem. Int. Ed.*, 38:3748–3752, 1999.
[100] K. T. Rim et al. Formatting aromatic hemispheres on transition-metal surfaces. *Angew. Chem. Int. Ed.*, 46:7891–7895, 2007.

[101] G. Otero et al. Fullerenes from aromatic precursors by surface-catalysed cyclodehydrogenation. *Nature*, 454:865–869, 2008.
[102] M. In't Veld et al. Unique intermolecular reaction of simple porphyrins at a metal surface gives covalent nanostructures. *Chem. Commun.*, pages 1536–1538, 2008.
[103] H.-Y. Gao et al. Glaser coupling at metal surfaces. *Angew. Chem. Int. Ed.*, 52:4024–4028, 2013.
[104] V. K. Kanuru et al. Sonogashira coupling on an extended gold surface in vacuo: reaction of phenylacetylene with iodobenzene on Au(111). *J. Am. Chem. Soc.*, 132:8081–8086, 2010.
[105] S. Weigelt et al. Covalent interlinking of an aldehyde and an amine on Au(111) surface in ultrahigh vacuum. *Angew. Chem. Int. Ed.*, 46:9227–9230, 2007.
[106] S. Weigelt et al. Surface synthesis of 2D branched polymer nanostructures. *Angew. Chem. Int. Ed.*, 47:4406–4410, 2008.
[107] M. Treier et al. Molecular imaging of polyimide formation. *Phys. Chem. Chem. Phys.*, 11:1209–1214, 2009.
[108] N. A. A. Zwaneveld et al. Organized formation of 2D extended covalent organic frameworks at surfaces. *J. Am. Chem. Soc.*, 130:6678–6679, 2008.
[109] F. Bebensee et al. A surface coordination network based on copper adatom trimers. *Angew. Chem. Int. Ed.*, 53:12955–12959, 2014.
[110] M. Matena et al. Transforming surface coordination polymers into covalent surface polymers: linked polycondensed aromatics through oligomerization of N-heterocyclic carbene intermediates. *Angew. Chem. Int. Ed.*, 47:2414–2417, 2008.
[111] M Mortimer and P Taylor. *Chemical kinetics and mechanism*. Royal Society of Chemistry, 1st edition, 2002.
[112] *Graphene Brillouin Zone and Electronic Energy Dispersion*. Wolfram demonstrations project. http://demonstrations.wolfram.com/. Accessed Mar. 1, 2015.
[113] C. M. Goringe, D. R. Bowler, and E. Hernández. Tight-binding modelling of materials. *Rep. Prog. Phys.*, 60:1447–1512, 1997.
[114] P. R. Wallace. The band theory of graphite. *Phys. Rev.*, 71:622, 1947.
[115] W. A. Harrison. *Electronic Structure and the Properties of Solids*. Dover Publications, 2nd edition, 1989.
[116] K. Wakabayashi et al. Electronic states of graphene nanoribbons and analytical solutions. *Sci. Technol. Adv. Mater.*, 11:054504, 2010.
[117] K. Nakada et al. Edge state in graphene ribbons: nanometer size effect and edge shape dependence. *Phys. Rev. B*, 54:17954–17961, 1996.
[118] Y.-W. Son, M. Cohen, and S. G. Louie. Energy gaps in graphene nanoribbons. *Phys. Rev. Lett.*, 97:216803, 2006.
[119] F. Aryasetiawan and O. Gunnarsson. The gw method. *Rep. Prog. Phys.*, 61:237–312, 1998.
[120] C. Tao et al. Spatially resolving edge states of chiral graphene nanoribbons. *Nature Phys.*, 7:616–620, 2011.
[121] M. Poljak et al. Influence of substrate type and quality on carrier mobility in graphene nanoribbons. *J. Appl. Phys.*, 114:053701, 2013.

[122] Y. Chen et al. Thermoelectric properties of graphene nanoribbons, junctions and superlattices. *J. Phys.: Condens. Matter*, 22:372202, 2010.
[123] L. Talirz et al. On-surface synthesis of atomically precise graphene nanoribbons. *Adv. Mater.*, 2016.
[124] D. Usachov et al. Nitrogen-doped graphene: efficient growth, structure and electronic properties. *Nano Lett.*, 11:5401–5407, 2011.
[125] J. Gebhardt et al. Growth and electronic structure of boron-doped graphene. *Phys. Rev. B*, 87:155437, 2013.
[126] H. Hertz. Über einen Einfluss des ultravioletten Lichtes auf die electrische Entlandung. *Annalen der Physik*, 267:983–1000, 1887.
[127] A. Einstein. Über einen die Erzeugung und Verwandlung des Lichtes betreffenden heuristischen Gesichtspunkt. *Annalen der Physik*, 17:132–148, 1905.
[128] S. Hüfner. *Photoelectron Spectroscopy*. Springer-Verlag, 2nd edition, 1996.
[129] J.J. Yeh. *Atomic Calculation of Photoionization Cross-Sections and Asymmetry Parameters*. Gordon and Breach Science Publishers, 1993.
[130] P. Hofmann. *Surface Physics. An Introduction*. ebook, Philip Hofmann, 2013. www.philiphofmann.net.
[131] C. N. Berglund and W. E. Spicer. Photoemission studies of copper and silver: Theory. *Phys. Rev.*, 136:A1030 – A1044, 1964.
[132] *Electron Inelastic Mean Free Path of Elements and Compounds. Practical Electron Microscopy and Database - An Online Book*. http://www.globalsino.com/EM/. Accessed Feb. 10, 2015.
[133] K. Siegbahn, C. Nordling, A. Fahlman, R. Nordberg, K. Hamrin, J. Hedman, T. Johansson, T. Bergmark, S. E. Karlsson, I. Lindgren, and B. Lindberg. *ESCA: Atomic, Molecular and Solid State Structure Studied by Means of Electron Spectroscopy*. Almqist & Wixell, 1967.
[134] T. A. Koopman. Über die zuordnung von wellenfunktionen und eigenwerten zu den einzelnen elektronen eines atoms. *Physica*, 1:104–113, 1933.
[135] W. Bardyszewski and L. Hedin. A new approach to the theory of photoemission from solids. *Physica Scripta*, 32:439–450, 1985.
[136] S. Tougaard. Energy loss in XPS: Fundamental processes and applications for quantification, non-destructive depth profiling and 3D imaging. *J. Electr. Spectr. Rel. Phen*, 178:128–153, 2010.
[137] N. Måtensson and A. Nilsson. On the origin of core-level binding energy shifts. *J. Electron Spectrosc. Relat. Phenom.*, 75:209–223, 1995.
[138] J. N. Andersen et al. Surface core-level shifts of some 4d-metal single-crystal surfaces: Experiments and ab initio calculations. *Phys. Rev. B*, 50:17525, 1994.
[139] J. Andersen and C. O. Almbladh. Many-electron singularity in X-ray photoemission and X-ray line spectra from metals. *Journal of Physics: Cond. Matter*, 13:11267, 2001.
[140] S. Doniach and M. Ŝunjić. Many-electron singularity in X-ray photoemission and X-ray line spectra from metals. *J. Phys. C*, 3:285, 1970.
[141] D. A. Shirley. High-resolution X-ray photoemission spectrum of the valence bands of gold. *Phys. Rev. B*, 5:4709, 1972.
[142] S. Tougaard et al. Test of algorithm for background correction in XPS under variation of XPS peak energy. *Surf. Interf. Anal.*, 13:225–227, 1988.

[143] Division of Synchrotron Radiation Research at Lund University webpage. www.sljus.lu.se.
[144] J. E. Ortega et al. One-dimensional versus two-dimensional electronic states in vicinal surfaces. *New J. Phys.*, 7:101, 2005.
[145] J. Stöhr. *NEXAFS spectroscopy*. Springer-Verlag, 2nd edition, 2003.
[146] J. G. Chen. NEXAFS investigations of transition metal oxides, nitrides, carbides, sulfides and other interstitial compounds. *Surf. Sci. Rep.*, 30:1–152, 1997.
[147] B. K. Agarwal. *X-Ray Spectroscopy: An Introduction*. Springer-Verlag, 2nd edition, 1991.
[148] A. S. Vinogradov et al. Low-lying unoccupied electronic states in 3d transition-metal fluorides probed by NEXAFS at the F 1s threshold. *Phys. Rev. B*, 71:045127, 2005.
[149] A.P. Lukirskii et al. *Sov. Phys. Solid State*, 6:32, 1964.
[150] A.P. Lukirskii et al. *Sov. Phys. Solid State*, 8:1422, 1966.
[151] A. Thompson, D. Attwood, E. Gullikson, M. Howells, K.-J. Kim, J. Kirz, J. Kortrigth, I. Lindau, Y. Liu, P. Pianetta, A. Robinson, J. Scofield, J. Underwood, and G. Williams. *X-ray Data Booklet*. Lawrence Berkley National Laboratory, University of California, 3rd edition, 2009.
[152] P. J. Duke. *Synchrotron Radiation. Production and Properties*. Oxford University Press, 1st edition, 2000.
[153] *Photon Science. DESY generates pulses of brilliant light*. http://photon-science.desy.de/research/studentsteaching/primers/synchrotron radiation/index eng.html. Accessed Feb. 18, 2015.
[154] MAX IV official webpage. www.maxlab.lu.se.
[155] G. Binnig et al. Surface studies by Scanning Tunneling Microscopy. *Phys. Rev. Lett.*, 49:57–61, 1982.
[156] Chen C. J. *Introduction to Scanning Tunneling Microscopy*. Oxford University Press, 1st edition, 1993.
[157] J. Bardeen. Tunnelling from a many-particle point of view. *Phys. Rev. Lett.*, 6:57–59, 1961.
[158] J. Tersoff and D. R. Hamann. Theory and application for the Scanning Tunneling Microscope. *Phys. Rev. Lett.*, 50:1998–2001, 1983.
[159] Omicron NanoTechnology GmbH. www.omicron.de/en/products/variable-temperature-spm/instrument-concept. Accessed Feb. 18, 2015.
[160] H. Hohenberg and W. Kohn. Inhomogeneous electron gas. *Phys. Rev.*, 136:B864, 1964.
[161] Official Web Site of the Nober Prize. http://www.nobelprize.org/nobel prizes/chemistry/laureates/1998/. Accessed Feb. 19, 2015.
[162] Surface Preparation Laboratory. http://www.spl.eu/. Accessed Mar. 4, 2015.
[163] J.V. Barth et al. Scanning tunneling microscopy observations on the reconstructured Au(111) surface: atomic structure, long-range superstructure, rotational domains, and surface defects. *Phys. Rev. B*, 42:9307–9318, 1990.
[164] S. Rousset et al. Self-ordering of au (111) vicinal surfaces and application to nanostructure organized growth. *J. Phys.: Condens. Matter*, 15:S3363, 2003.

[165] Angene Chemical company. http://www.angenechemical.com/. Accessed Mar. 4, 2015.
[166] Langchem inc. http://www.langchem.com/. Accessed Mar. 4, 2015.
[167] M. A. Van Hove, W. H. Weinberg, and Chan C. M. *Low-Energy Electron Diffraction: experiment, theory and surface structure determination*. Springer-Verlag, 1st edition, 1986.
[168] P. Han et al. Bottom-up graphene-nanoribbon fabrication reveals chiral edges and enantioselectivity. *ACS Nano*, 8:9181–9187, 2014.
[169] VG Scienta. www.vgscienta.com.
[170] R. Nyholm et al. The modified SX-700 monochromator with a spherical focusing mirror: a configuration for -1 diffraction order. *Nucl. Instr. and Meth. A*, 246:267–271, 1986.
[171] D. F. Perepichka and F. Rosei. Extending polymer conjugation into the second dimension. *Science*, 323:216–217, 2009.
[172] R. Chau et al. Integrated nanoelectronics for the future. *Nat. Mater.*, 6:810–812, 2007.
[173] R. Yang et al. Isolated nanographene crystals for nano-floating gate in charge trapping memory. *Sci. Rep.*, 3:2126, 2013.
[174] M. Schulz. The end of the road for silicon? *Nature*, 399:729–730, 1999.
[175] T Ito and S. Okazaki. Pushing the limits of litography. *Nature*, 406:1027–1031, 2000.

Acta Universitatis Upsaliensis

Digital Comprehensive Summaries of Uppsala Dissertations from the Faculty of Science and Technology 1385

Editor: The Dean of the Faculty of Science and Technology

A doctoral dissertation from the Faculty of Science and Technology, Uppsala University, is usually a summary of a number of papers. A few copies of the complete dissertation are kept at major Swedish research libraries, while the summary alone is distributed internationally through the series Digital Comprehensive Summaries of Uppsala Dissertations from the Faculty of Science and Technology. (Prior to January, 2005, the series was published under the title "Comprehensive Summaries of Uppsala Dissertations from the Faculty of Science and Technology".)

Distribution: publications.uu.se
urn:nbn:se:uu:diva-295884

ACTA
UNIVERSITATIS
UPSALIENSIS
UPPSALA
2016